UC Berkeley
UC Berkeley Electronic Theses and Dissertations

Title
Transient Absorption Spectroscopy with Isolated Attosecond Pulses

Permalink
https://escholarship.org/uc/item/3hh4m9zt

Author
Bell, Marie Justine

Publication Date
2013

Peer reviewed|Thesis/dissertation

eScholarship.org Powered by the California Digital Library
University of California

Transient Absorption Spectroscopy with Isolated Attosecond Pulses

By

Marie Justine Bell

A dissertation submitted in partial satisfaction of the

requirements for the degree of

Doctor of Philosophy

in

Chemistry

in the

Graduate Division

of the

University of California, Berkeley

Committee in charge:

Professor Stephen R. Leone, Co-Chair
Professor Daniel M. Neumark, Co-Chair
Professor Graham Fleming
Professor Roger Falcone

Spring 2013

Transient Absorption Spectroscopy with Isolated Attosecond Pulses

Copyright 2013
by
Marie Justine Bell

Abstract

Transient Absorption Spectroscopy with Isolated Attosecond Pulses

by

Marie Justine Bell

Doctor of Philosophy in Chemistry

University of California, Berkeley

Professor Stephen R. Leone, Co-Chair
Professor Daniel M. Neumark, Co-Chair

Ultrashort pulses with durations less than one femtosecond advance understanding of chemistry and physics by facilitating time-resolved measurements on the timescale of electronic motion. A very pragmatic type of experiment incorporating isolated attosecond (10^{-18} s) pulses is transient absorption measurements that utilize the broad bandwidth of attosecond pulses. In these measurements the dispersed spectrum of the isolated attosecond pulse is recorded after the attosecond pulse and a time-delayed optical pulse pass through an experimental target of interest. This thesis focuses on the development of an attosecond transient absorption spectrometer with the ultimate goal of using the spectrometer to measure atomic and molecular dynamics. Two experimental studies are presented: one focusing on the behavior of helium atoms bathed in a strong near-infrared optical field, and one focusing on measurement of the lifetimes of autoionizing states in xenon.

Measurement of the absorption spectrum of atomic helium bathed in a near-infrared (780 nm) field exhibits new features when the attosecond pulse and the optical pulse are overlapped in the gas target. The features near the $1s2p$ transition at 21.21 eV are identified as intermediates in two-photon transitions to reach nearby s and d helium excited states that are inaccessible via one photon transitions from the $1s^2$ ground state of He. Initial measurements identified three intermediate states, and further experiments investigated the behavior of the states as the near-infrared field intensity is increased.

Attosecond time-resolved measurement of ultrashort lifetimes of autoionizing states is also investigated. The $5s5p^6 6p$ and $5s5p^6 7p$ autoionizing states of xenon are visible in the extreme-ultraviolet absorption spectrum of Xe as Fano resonances. The Fano resonances are suppressed by a time-delayed near-infrared pulse and recover with a time-constant that is related to the lifetime of the state. The studies here identified key parameters for time-resolved measurements of the autoionization lifetime, including spectral resolution of the attosecond transient absorption spectrometer.

To Nick, for everything.

Contents

List of figures

List of tables

Acknowledgments

I am very fortunate to have encountered a diverse group of great scientists during my tenure at UC Berkeley. I am especially indebted to former project leaders Thomas Pfeifer and Hiroki Mashiko who were fountains of ideas, advice, and encouragement. Many thanks are due to senior graduate students working on the attoseond project, Mark Abel and Phil Nagel, for teaching me the necessary fundamentals of lasers, non-linear optics, and spectroscopy and how to navigate the murky waters of grad school. The work presented here builds off the efforts started by all former (and some current) group members. I want to thank Adrian Pfeiffer, for his help with computational studies. His efforts helped us understand and refine our experiments.

I am very glad to have shared time, lab and office space with current atto-team members Annelise Beck, Erika Warrick, and Gitti Berhnardt. I am eager to see what great science comes out of experiments in the newly-revamped atto-lab. We worked hard and had some great silly times together! Annelise, I enjoyed sharing the atto project with you for four years. I feel lucky to have had such a great labmate not only for doing lab work, but also for seeing metal bands, playing board games, and geeking out over Star Trek.

Adam Bradford, Kathleen Fowler, and Michelle Haskins were always able to make the paperwork and bureaucracy run as smoothly as possible. Any issue I brought to their attention seemed to magically clear up.

I want to recognize the contribution of our theoretical collaborators: Professors Kenneth J. Schafer and Mette B. Gaarde, and their group members Shaohao Chen, and Mengxi Wu. They offered valuable insight into our experiments and were very professional collaborators.

I deeply appreciate the time and effort that committee members, Professors Graham Fleming and Roger Falcone, are spending to serve on my thesis and qualifying exam committee. Lastly, many thanks are due to Professors Stephen Leone and Daniel Neumark for offering good experimental and scientific advice, teaching me the value of good, rigorous science and letting me work on an amazing experimental setup.

Chapter 1

Introduction to attosecond spectroscopy

1.1 Introduction

Time-resolved spectroscopy, the utilization of short bursts of light to measure chemical dynamics, is a powerful tool for understanding the fundamentals of chemical processes. This technique of using short pulses of light to analyze the behavior of a sample after excitation has a rich scientific history. For example, the femtosecond dynamics of molecules and atoms have been studied for well over two decades. The Nobel prize winning work of Zewail has been noted for advancing the understanding of quantum chemistry by elucidating transition states in chemical reactions [1]. A key component of these measurements is the ability to collect information on the natural timescale of chemical processes.

Recently, developments in laser technology have introduced the capability to produce pulses of radiation that are shorter than 1 fs in duration [2]. Application of sub-femtosecond pulses to chemical dynamics permits real-time measurements of energetics and populations of electronic states as a function of time because electronic dynamics take place on a few-femtosecond to sub-femtosecond timescale. Measurements of fundamental chemical and physical processes, including valence and inner-valence ionization, strong field ionization, and lifetimes of highly excited states [3], have yielded interesting results; for example, electronic coherences [4] or sub-femtosecond delays in ionization [5]. This work focuses on the powerful opportunities that exist for measuring of lifetimes and energetics of highly excited states in addition to monitoring optical modification of optical properties of materials with unprecedented time resolution.

1.2 Attosecond science

Vibrational periods of molecules are typically on the femtosecond and picosecond timescale, consequently time-resolved spectroscopy with femtosecond pulses has provided valuable insight

into the motions of nuclei over the course of chemical reactions. Dynamics occurring on the attosecond and few-femtosecond timescale are typically motions of electrons [6–10]. Time-resolved measurements on the attosecond timescale can probe short-lived states (with lifetimes that range from sub-femtosecond to tens of femtoseconds) that decay via autoionization or Auger decay [8, 11]. Attosecond measurements may also probe fundamental processes, for example measuring the length of time an electron needs to escape from an atom or surface in photoionization or field ionization [5, 9, 12]. A rich topic in femtosecond spectroscopy is coherent phenomena like vibrational wave packets. The analogous scenario on the attosecond timescale is coherent superpositions of electronic states [4, 10]. Over the past decade efforts have been directed toward incorporating more complicated molecular or solid state targets and toward testing common assumptions of ionization and absorption.

Auger relaxation and, more generally, autoionization relaxation processes are driven by configuration interaction and occur on sub-femtosecond to picosecond timescales. Atomic autoionization processes are driven by electron-electron interactions, but molecular autoionization may be mediated by vibronic or rotational couplings in addition to electron-electron interactions. Real-time measurements of autoionization and Auger decay elucidate electronic reorganization after ionization, by determining how quickly electrons rearrange following a sudden ionization. Influential measurements of ultrashort lifetimes with attosecond time resolution include measurement of Auger decay in core-excited atomic krypton [8, 11]. Auger emission mirrors the lifetime of the core-excited state, so the lifetime was determined by measuring the emission time of Auger electrons with photoelectron streaking. Subsequent efforts utilizing photoelectron streaking and transient absorption spectroscopy include measuring the lifetimes of autoionizing states of helium [13] and argon [3], respectively. Attosecond experiments on molecular species have the power to examine dynamics where lifetimes determined from frequency domain measurements of spectral linewidths may be limited by complex lineshapes with overlapping features and contributions from multiple vibrational states [14]. Additionally, attosecond experiments with molecular targets may probe the competition between electronic and nuclear coupling in relaxation pathways (for example, relaxation of superexcited states of molecules). Uniquely molecular relaxation mechanisms may also be studied in core-excited molecular and loosely bound dimer targets (for example Ne_2 or XeF_2). For example, the core-excited states may relax via interatomic Coulombic decay, where the core-hole lifetime decreases (relative to the isolated atom core-hole lifetime) because the double ionization potential is reduced when the holes are localized on two separate nuclei [15–18]. Measurement of core-hole lifetimes in molecules that decay via interatomic Coulombic decay can provide valuable parameters for understanding energy transfer and electronic correlation in molecules.

Photoionization is a fundamental component of spectroscopy and several experiments (performed in the research groups of Anne L'Huillier and Ferenc Krausz) have focused on measuring relative time delays between emission times of electrons from different atomic subshells. For example, a sub-femtosecond delay in electron emission has been measured for electrons emitted from the $2p$ orbital of gas phase neon relative to the $2s$ orbital [5]. Experimental and theoretical [19–21] work focusing on short delays in photoemission can

provide measurements of the Wigner time delay: the delay in arrival time of the attosecond pulse induced by the presence of the atom [22, 23]. The delays measured in these experiments answer fundamental questions: When exactly an electron escapes from atom? And when processes, in this case ionization events, can be considered to occur simultaneously? Another interesting feature of measuring sub-femtosecond photoionization delays is the impact of the optical laser field, typically used in attosecond pump-probe experiments, on the measured time delays. The interpretation of time delays in neon photoionization and subsequent work utilizing attosecond pulse trains to measure relative time delays between ionization of electrons from $3p$ and $3s$ orbitals of atomic argon [24], is informed by theoretical calculations that incorporate the effect of the near-infrared (NIR) streaking field on the electrons' trajectories [19–21]. The Wigner time is produced by the incident attosecond pulse scattering off the atom; therefore, measurements of sub-femtosecond Wigner time delays provide a valuable bench mark for scattering theories. Measurements of this kind are also practically important as the Wigner time can be thought of as the propagation time of the scattered pulse and, as such, is a measure of energy transfer time [25]. Experiments on solid state targets have measured the delay between emission from Fermi-level and $4f$ core orbitals of a tungsten crystal, and theoretical work has identified the contribution to the delay resulting from the time necessary for electrons to escape from the surface [26–28].

Several experiments (performed in the research groups of Ursula Keller and Ferenc Krausz) have investigated atomic and molecular dynamics driven by a strong laser field ($\sim 10^{12} - 10^{14}$ W/cm^2). A NIR laser has an optical period of 2.6 fs, therefore dynamics driven by the instantaneous oscillations of the laser field occur on the few-femtosecond to sub-femtosecond timescale. In 2007, an influential experiment measuring the yield of doubly ionized neon cation produced from field ionization of singly ionized neon cation revealed a step like character in Ne^{2+} yield [8, 29]. The results experimentally verified that the field ionization rate depends on the instantaneous field strength. Additional work has focused on determining whether field ionization adiabatically follows the laser field or if electrons are ionized after some time delay. Angular streaking measurements (that utilize an elliptically polarized streaking field instead of the typical linearly polarized streaking field) of strong field ionization of helium atoms measured an almost instantaneous ionization and placed an upper limit of 12 as on the tunneling time [9, 12]. Similar to measurements of Wigner time delays, measurement of tunneling time delays requires consideration of subtle effects including field induced Stark shifts and multielectron dynamics. Changes to the tunneling offset angles (the angular offset caused by escaping electrons interacting with the cation Coulomb potential) as a function of field intensity in gas phase argon are attributed to induced dipole and Stark shift effects [30]. These experiments suggest further avenues to study multielectron dynamics in more complex systems, including larger more polarizable molecules and targets where multiple field ionization events may take place.

Femtosecond and picosecond time-resolved measurements of strong field ionization of gas phase xenon [31] and krypton [32, 33] measured quantum state distributions and hole orbital alignment effects. Subsequent transient absorption measurements and theoretical studies of strong field ionization of gas phase krypton with isolated attosecond pulses have

revealed not only alignment effects, but also superpositions of atomic states [4, 34, 35]. The electronic coherence can only be directly measured with attosecond time-resolved techniques. Kinematically complete measurements of hole localization in core-ionized molecular nitrogen inferred, but not directly probed, electronic coherence [36]. Examining the coherence generated during strong field double ionization may provide insight into competition between sequential and non-sequential double ionization [37]. Turning toward more complex molecular targets, measurements of coherent electronic superpositions may allow vibronic dephasing effects or additional losses of coherence to be studied. Direct measurements of electronic coherences and dephasing may elucidate interactions of electronic correlations and nuclear dynamics. A technical challenge of generating coherent superpositions via field ionization, is the requirement that the NIR ionization pulse be short enough to create electronic states in phase. Practically, few-femtosecond and even single-optical-cycle pulses are necessary [38].

Attosecond science is an emerging field focused on measuring fundamental parameters of light-matter, electron-electron, and electron-nuclear interactions with sub-femtosecond time resolution. A significant portion of experiments with attosecond time resolution in the past decade have focused on proof of principle measurements on atomic species, but current efforts are shifting toward investigations of molecular dynamics with attosecond time resolution.

1.3 Attosecond pulse generation

Production of pulses with durations in the sub-femtosecond regime requires radiation in the extreme ultraviolet range of the electromagnetic energy spectrum, because the pulse duration cannot be smaller than the optical period of the radiation [39]. For example 300 nm radiation has an optical period of 1 fs, so to make pulses shorter than 1 fs radiation of a higher frequency must be used. Additionally, considering the time-energy Fourier transform pair, a sub-femtosecond pulse necessarily needs a broad spectral bandwidth–a transform-limited pulse 1 fs in duration requires a 1.8 eV spectral bandwidth [40]. Traditional laser gain media do not allow the production of broadband radiation in the desired energy range. High harmonic generation from optical pulses is currently the only source for generating radiation with the appropriate characteristics for isolated attosecond pulses. Future developments in free-electron laser sources, which currently are limited to few-femtosecond durations at the shortest, may expand the possibility of high photon flux attosecond light sources.

1.3.1 High harmonic generation

In the process of high harmonic generation, a strong laser field is converted to a high harmonic in a non-linear medium, most commonly a noble gas in a cell, jet, or capillary (molecular gas phase targets and solid-state targets may also be used, but are less common). High harmonic generation can be explained in terms of a semi-classical model proposed by Corkum [41]. The laser field at the focus of the laser is comparable to the Coulomb potential that binds electrons to the atoms. At an extremum of the oscillating laser field, the potential

that binds an electron to the atom is suppressed, allowing an electron to tunnel-ionize. The nascent electron is now a charged particle in an oscillating electric field, and, as such, it is accelerated away from the parent cation. As the laser field reverses, the electron is accelerated back toward the parent cation, and when the field is zero, the electron may recombine. As the electron was accelerated in the laser field, its kinetic energy increased; therefore recombination requires that energy be emitted, possibly in the form of a photon. The energy of the radiation emitted will correspond to the kinetic energy the electron gained as it was accelerated by the laser field and the ionization potential of the parent atom:

$$\hbar\omega = I_p + 3.17U_p \tag{1.1}$$

where I_p is the ionization potential of the parent atom and U_p is the pondermotive energy of an electron in a electromagnetic field defined as:

$$U_p = \frac{e^2 E_0^2}{4m_e\omega_0^2} \tag{1.2}$$

where e is the elementary unit of charge, E_0 is the electric field strength in V/m, m_e is the mass of an electron and ω_0 is the angular frequency of the laser field.

The recombination may happen at every zero crossing of the electric field, yielding a train of attosecond pulses separated in time by the half-period of the driving laser field and with a spectrum corresponding to a series of peaks whose energy is an odd harmonic of the driving laser frequency. A full quantum mechanical model of high harmonic generation has been developed [42].

Attosecond pulse trains have permitted measurements of ultrafast molecular dissociation [43, 44], precision measurements of aligned molecules [45], and condensed phase targets [46] on femto- and picosecond timescales, but for resolving dynamics on the sub- and few-femtosecond timescale, in real time, single isolated attosecond pulses are advantageous.

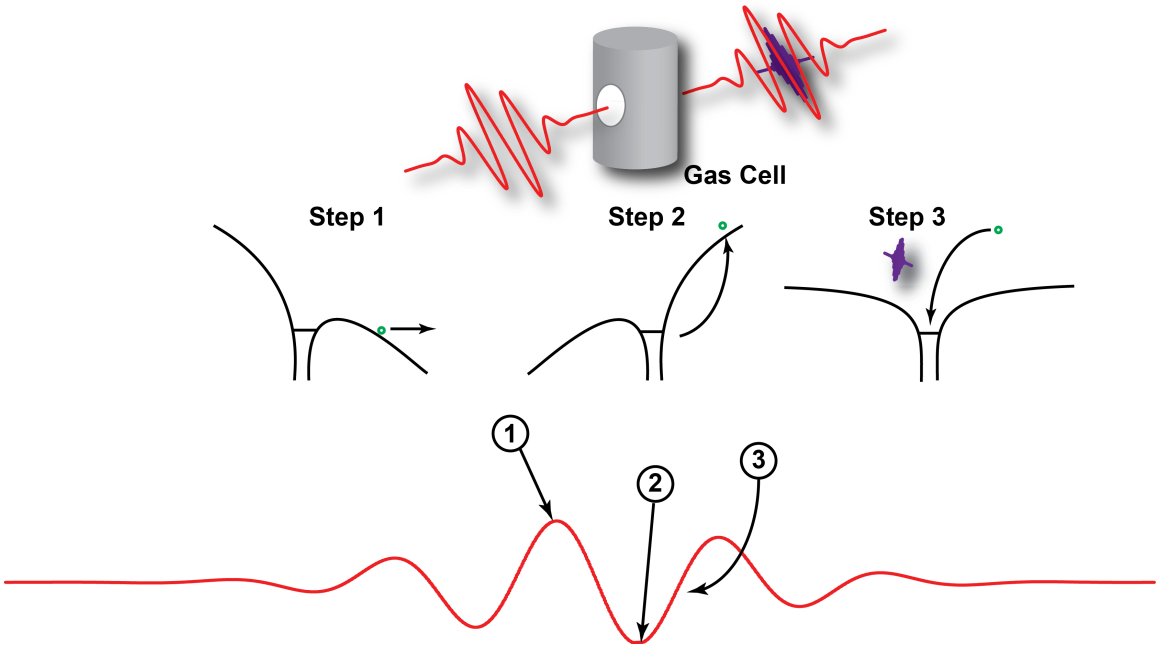

Figure 1.1: The semi-classical mechanism for high harmonic generation (HHG). A strong few-cycle laser field suppresses the coulomb binding potential of an atom, allowing an electron (shown in green) to tunnel-ionize in step 1. This electron is accelerated in the field in step 2. Finally, in step 3, the electron can recombine with the parent cation releasing a burst of photons.

1.3.2 Isolated attosecond pulses

Intensity gating

Isolated attosecond pluses were first demonstrated in 2001 [2]. This advancement was achieved by selecting a single attosecond pulse with the highest photon energy from a train of attosecond pulses produced by high harmonic generation. Intensity gating utilizes the scaling of high harmonic photon energy with the driving laser intensity: The single attosecond pulse is selected by utilizing a high pass filter such that only one attosecond pulse in the pulse train has sufficiently high photon energy to pass through the metallic high pass filter. This technique requires very short pulses, so that the difference in laser intensity between each successive half-cycle is large. Practically, the pulse duration of the driving laser should be 5 fs or less for NIR pulses; single optical cycle driving laser pulses are the state-of-the-art implementation of this method [38]. High harmonic generation is controlled by the driving laser field so precision control of the laser electric field (in contrast to the laser intensity envelope) is necessary to generate isolated attosecond pulses by this method. Stabilization of the electric field waveform and control of the pulse duration are prerequisites for isolated attosecond pulse production via intensity gating. Finally, this method is limited to using the so-called cut-off region of HHG. Typical experimental photon energies may be over 70 eV or

over 100 eV if zirconium or silicon filters, respectively, are used.

Polarization gating

Controlling the polarization of the driving field was proposed in 1994 [47–49] to limit or gate harmonic generation to one half-cycle. Polarization gating exploits the suppression of harmonic generation by a circularly polarized field, by creating two circularly polarized pulses that are only overlapped for one optical half-cycle. The polarization of the total field at pulse overlap is linear, so harmonic recombination is allowed. Effectively, the pulse is partially circularly polarized. The so-called gate width (τ_g) where harmonic production is allowed can be estimated from:

$$\tau_g = \epsilon \frac{\xi_{th}}{\ln(2)} \frac{t_p^2}{T_d} \tag{1.3}$$

where ϵ is the ellipticity of the laser pulses ($\epsilon = 1$ for circularly polarized light), ξ_{th} is the threshold ellipticity for suppression of harmonic recombination, t_p is the input pulse duration, and T_d is the delay introduced between the two counter-rotating pulses. This condition was experimentally achieved in 2003 [50] by using birefringent quartz plates. The plates are designed to produce two counter-rotating circularly polarized pulses that are time delayed so that the pulses overlap for only one optical half-cycle [50]. This technique is advantageous because it opens up broader ranges of spectrum for use with attosecond pulse generation for use in experiments, for example, around 20 or 40 eV.

Double optical gating

Double optical gating (DOG) [51–53], is an evolution of polarization gating, utilizing the same techniques, but it further relaxes the generating conditions by overlapping the second harmonic of the driving field with the driving field itself. Adding the second harmonic breaks the symmetry of the electric field and as a result recombination resulting in emission of light only occurs once per optical cycle. The addition of a β-barium borate (BBO; $\beta-BaB_2O_4$) for second harmonic generation to the high harmonic generation scheme produces significant gains in efficiency because the high harmonic production needs to be gated to only one optical cycle, instead of one optical half-cycle. Thus, the delay between the two counter-rotating pulses may be shorter and, therefore, for a given input pulse DOG will result in less preionization of the high harmonic generating gas on the leading edge of the pulse before harmonic generation is permitted, compared to polarization gating alone. Another key advantage of DOG is the ability to generate a supercontinuum spectrum of the attosecond pulse, see for example Figure 1.2. This allows certain spectral energy ranges for experiments to be selected by means of filters [54].

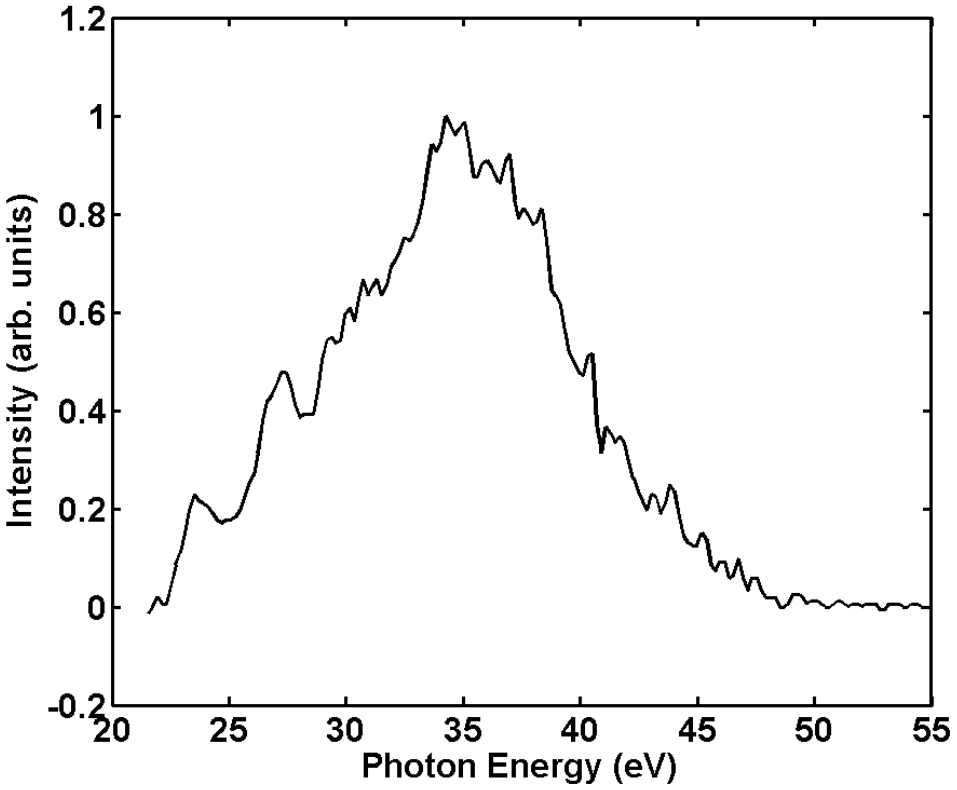

Figure 1.2: Extreme ultraviolet spectrum recorded using double optical gating (DOG). The spectrum of high harmonic generation utilizing DOG to create isolated attosecond pulses. The supercontinuum XUV spectrum is generated by focusing the optical DOG field into a gas cell filled with 2 Torr argon gas. An Aluminum filter (200 nm thick) reflects the residual optical light.

Future attosecond light sources

Free-electron laser based sources are a possible source for high photon flux attosecond pulses, but current free-electron lasers can only produce few-femtosecond pulses with durations shorter than 10 fs. New pulse production methods including spatial selection [55] and slicing techniques [56–58] are currently being developed to produce sub-femtosecond pulse durations. Challenges like timing jitter (currently $30 - 100$ fs RMS) are an experimental limitation.

1.3.3 Photoelectron streaking

To measure the duration of attosecond pulses photoelectron streaking [59] is typically used; autocorrelation methods typically used with femtosecond optical pulses require non-linear crystals, which do not exist in the XUV photon energy range [39]. In this technique the

attosecond pulse is superimposed with a near-infrared pulse (typically at an intensity of approximately 10^{12} W/cm^2) with a variable time delay in the interaction region of a time-of-flight spectrometer. The attosecond pulse ionizes typically a noble gas target, creating what is assumed to be an electron wave packet replica of the attosecond pulse. If the photoelectrons detected are indeed a wave packet replica of the attosecond pulse, ionization must be instantaneous and ionization must be unaffected by the presence of a strong laser field.

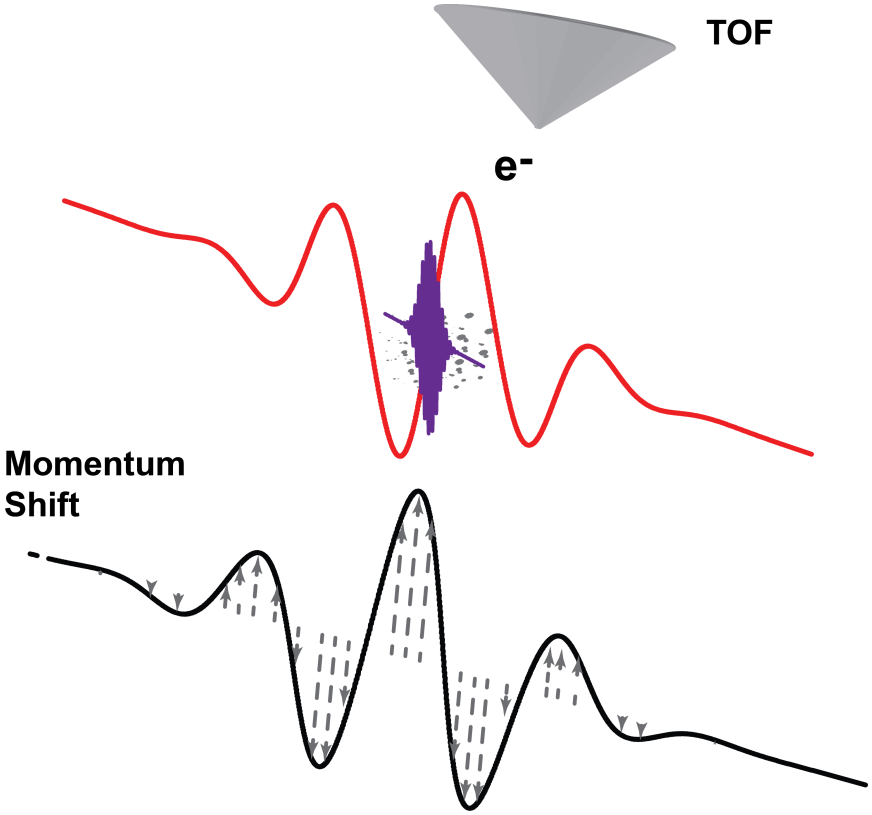

Figure 1.3: The mechanism of photoelectron streaking. An isolated attosecond pulse (in purple) is overlapped with a NIR optical field (in red). The nascent photoelectrons feel a shift in momentum from the oscillating NIR field. The shift in momentum (p) is measured by the photoelectron time-of-flight as a shift in kinetic energy ($\frac{p^2}{2m_e}$) where m_e is the mass of an electron.

The photoelectrons that are produced experience a time-dependent shift in momentum from the time-varying electric field of the optical pulse, as diagrammed in Figure 1.3. The shift in momentum (Δp) for electrons ionized at time t_i is given by:

$$\Delta p(t_i) = -e \int_{t_i}^{\infty} E_l(t) \mathrm{dt} \tag{1.4}$$

where e is the charge of an electron, and $E_l(t)$ is the time-dependent electric field [59]. A

measured spectrogram is shown in Figure 1.4. The pulse duration is retrieved from the spectrogram via frequency resolved optical gating for compete reconstruction of attosecond bursts (FROGCRAB) [60–62] with an iterative algorithm like the principle components generalized projection algorithm (PCGPA) [63]. A key assumption in this methodology is that the central momentum of the electron wave packet that is liberated from the ionized target can describe the election wave packet. Practically, this means that the momentum spread of the wave packet is small compared to the central momentum of the wave packet. Measurements of high kinetic energy electrons (for example Auger electrons from gas phase krypton released with a kinetic energy of 40 eV and an energy spread of a few eV) fulfill the condition, but this is not necessarily the case for lower kinetic energy electrons.

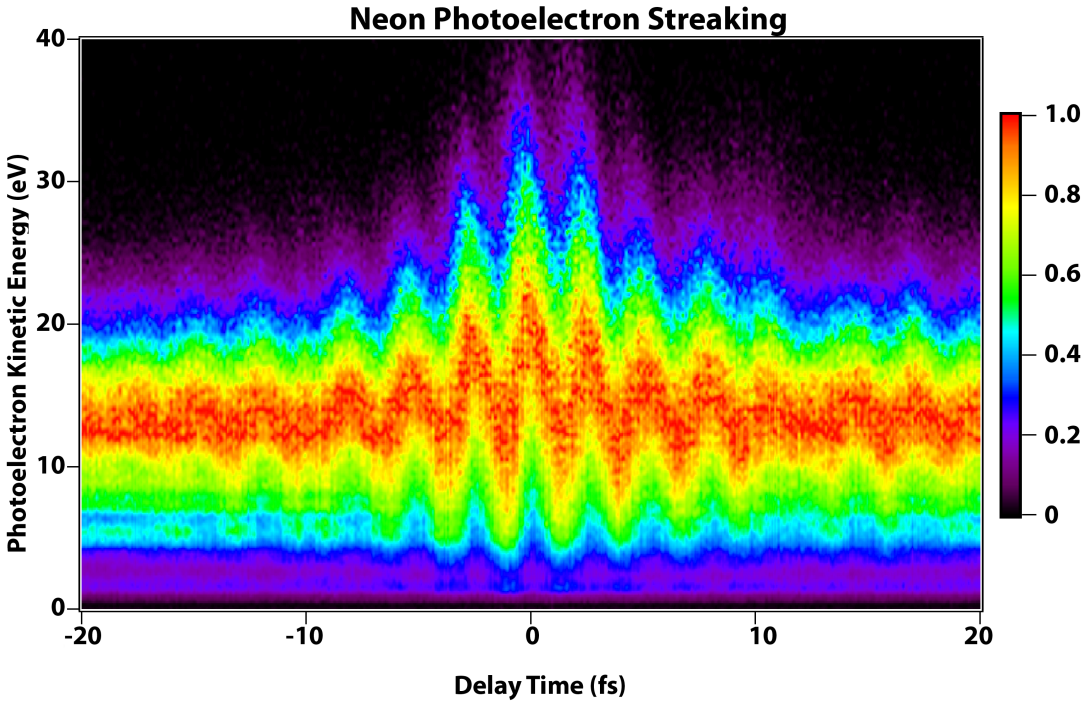

Figure 1.4: Streaking spectrogram recorded with neon gas ($Ip = 21.56$ eV) as the photoionization target. Photoelectrons ionized by the attosecond pulse (in the absence of the NIR field) have kinetic energies centered around 15 eV; as the NIR pulse begins to overlap the attosecond pulse, the measured kinetic energies of the photoelectrons shifts.

Recent developments (2010) of new methods for determination of the attosecond pulse duration include the phase retrieval by omega oscillation filtering (PROOF) [64] method, which attempts to determine attosecond pulse duration without needing the so-called central momentum approximation. The method again uses a spectrogram generated in the same manner as FROGCRAB, but the analysis is different. The spectrogram is Fourier filtered at the dressing laser frequency to produce a spectrogram of the "one omega component". The spectral phase of the attosecond pulse is then extracted from either the phase or the intensity

of the one omega component depending on conditions.

Efforts focusing on elucidating any effect a strong field may have on the ionization events measured in photoelectron streaking are a current area of research [19].

1.4 Attosecond spectroscopy

1.4.1 Photoelectron and photoion measurements

Photoelectron streaking has been used to measure the emission time of electrons following excitation by extreme-ultraviolet attosecond pulses. For example, time-resolved measurements of Auger decay were made in 2003 by Drescher et al. [11] The experimental procedure is very similar to the procedure for measuring attosecond pulse durations. However, unlike the photoelectrons liberated in FROGCRAB streaking measurements of attosecond pulse durations, the ionization event is not instantaneous; the electron wave packet is released over several optical cycles. This means parts of the electron wave packet (emitted at separate times) may acquire the same shift in momentum. There are multiple ways electrons may end up in the same final state. As a result, the measured photoelectron spectrogram will have a structure indicative of interference; namely, sidebands separated in energy by one NIR photon from the main photoelectron line. Drescher et al. used isolated attosecond pules (with central energy of 93 eV) to ionize core electrons from the $3d$ subshell of gas phase krypton. The highly excited Kr^+ may emit a subsequent Auger electron after a time delay. From the resulting data the lifetime of the $3d_{5/2}$ core hole states was determined to be 7.9 fs, agreeing with a value obtained from experimentally measured linewidths [65]. Similar measurements of autoionizing states in atomic helium have also been performed [13]. Additional information on ultrafast decay can be achieved by incorporating more sophisticated measurement techniques; for example, velocity map imaging [13], which provides the opportunity for measuring angular distributions of emitted electrons in addition to electron kinetic energies. The tunneling time is obtained for excited electrons produced after Ne gas was irradiated by a 250 as duration 91 eV attosecond pulse [29]. The attosecond pulse could simultaneously remove a core electron from the neon atom and excite an electron to an unfilled orbital. A 5.5 fs 750 nm NIR laser pulse, overlapped with the attosecond pulse with a variable time delay, tunnel ionized the excited electrons. The tunneling rate is determined from the amount of Ne^{2+} cations measured as a function of delay between the attosecond and NIR laser pulses. Notably, the yield of the Ne^{2+} cations increased in steps corresponding to the sub-femtosecond oscillations of the NIR field.

1.4.2 Transient absorption spectroscopy

Absorption spectroscopy is a convenient application of isolated attosecond pulses, because the broad bandwidth of attosecond pulses can be utilized to monitor several excitations at one time. In this technique, an attosecond pulse is superimposed on a sample (most simply a gas cell) with a NIR probe pulse with a variable time delay. Recording the dispersed spectra

of attosecond pulses after interaction with a target allows multiple bound states of atoms or molecules to be monitored simultaneously. The appearance of new spectral features (transient absorptions) or disappearance of field-free spectral features (bleaches) in the transmitted spectra as a function of pump-probe delay indicate which transitions take place.

Transient absorption spectroscopy has a rich history for interrogating chemical dynamics beginning with flash photolysis measurements [66]. Recent developments allow experiments to be performed on the timescale of nuclear [1, 67] and even electronic [4, 8, 68] motion. Ultrafast absorption experiments have yielded insight into fundamental chemical and biological processes that depend on light-matter interaction; for example reactions of retinal isomerization [69] and energy transfer during photosynthesis [70]. Femtosecond transient absorption spectroscopy with ultraviolet, visible, and NIR pulses is well established [71], but only relatively recently have femtosecond [72] and sub-femtosecond [3, 4, 73, 74] transient absorption measurements in the XUV range of the spectrum become possible.

An advantage of the technique is that the spectral resolution is not limited by the time bandwidth product. The time resolution of transient absorption pump-probe measurements results from the delay between the pump and probe pulses, and their cross correlation. The spectral resolution is determined from a completely separate event in the spectrometer. The spectrometer resolution is dependent on the geometry, grating, and sensitivity of the recording device. Because the time resolution and the spectral resolution are not correlated the spectra may be acquired with arbitrary resolution [75, 76].

The initial attosecond transient absorption measurements used a strong 7×10^{14} W/cm^2 750 nm NIR pulse with a duration of less than 4 fs to ionize valence $4p$ electrons of atomic krypton, and probe the ionization process using attosecond pulses with an approximately 150 as duration centered at 80 eV to excite electrons from the $3d$ subshell of Kr^+ to the vacant $4p$ holes produced during field ionization. The measurements revealed that strong field ionization yielded Kr^+ with vacancies in the $4p_{1/2}$ and $4p_{3/2}$ orbitals produced in a coherent superposition. Additional work has focused on measuring ultrafast decay pathways in gas phase atomic argon [3]. These experiments suggest a diverse spectrum of future experiments incorporating broadband excitation, much like the excitation of vibrational wave packets utilized in some femtosecond spectroscopy techniques. Attosecond transient absorption spectroscopy has recently been extended to solid state targets [73].

1.4.3 Interpretation of spectra

To interpret transient absorption measurements it is useful to consider the atomic response to an electromagnetic field. The incident field induces a dipole oscillation in the absorption target, similar to the Drude model of an electrons driven by an electromagnetic field [71, 75–77]. The dipole will ring and radiate at a particular frequency corresponding to the atomic or molecular transitions excited. The radiated field is the so-called induced polarization field. The incident driving field and the radiated field are detected together. The out of phase

component of the radiated field corresponds to absorption, as shown:

$$s(\omega) = \frac{4\pi\omega}{cn(\omega)} Im[\frac{\int_{-\infty}^{+\infty} E(t)^* P(t)\ \mathrm{dt}}{\int_{-\infty}^{+\infty} |E(t)|^2\ \mathrm{dt}}] \tag{1.5}$$

Where $s(\omega)$ is the absorption signal at frequency ω, c is the speed of light in vacuum, $n(\omega)$ is the index of refraction, $P(t)$ is the time-dependent polarization, and $E(t)$ is the incident electric field [77]. The polarization and the electric field can be written as:

$$E(t) = 2E_0(t)cos(\omega t) = E_0(t)[Exp(i\omega t) + Exp(-i\omega t)] \tag{1.6}$$

$$P(t) = 2P_0(t)cos(\omega t + \phi) = P_0(t)[Exp(i\omega t + i\phi) + Exp(-i\omega t - i\phi)] \tag{1.7}$$

The ϕ phase term is included in $P(t)$, because the polarization may have any phase with respect to the incident electric field. $E_0(t)$ and $P_0(t)$ are the time-dependent field and polarization envelopes. Equation 1.7 can be rewritten as:

$$P(t) = [P_0(t)cos(\phi)]cos(\omega t) + [P_0(t)sin(\phi)]sin(\omega t) \tag{1.8}$$

When $E(t)^*$ is multiplied by $P(t)$ only the $sin(\omega t)$ terms will be imaginary, and so only the $sin(\omega t)$ terms will survive in $s(\omega)$. In transient absorption spectroscopy the induced polarization will sample not only dynamics at the instant the polarization is excited, but also dynamics occurring at all times after until the polarization has decayed. This can lead to the counterintuitive result that the polarization induced by an attosecond pulse may be altered by a subsequent NIR pulse, which can change the radiated field and as a result the transmission of the attosecond pulse [76]. Linear absorption corresponds to the first-order (in electric field) polarization, while techniques like Raman spectroscopy and four-wave mixing correspond to third-order (in electric field) polarization [71, 77].

1.4.4 Dressed absorption: He in a strong field

Attosecond pump-probe measurements typically utilize a strong optical laser pulse in addition to the attosecond pulse. The strong optical pulse can then induce certain structure in the experimental target, for example, resulting in electromagnetic induced transparency and Autler-Townes splitting. The ability of a strong 780 nm laser pulse to couple the $1s2p$ and $1s3p$ states of helium to the nearby s and d excited states is studied in detail in Chapters 3 and 4.

1.4.5 Probing short-lived electronic states: Xe autoionization

Autoionizing electrons are electrons emitted in a decay pathway induced by configuration interaction of excited states that are higher in energy than the ionization potential. These

states have short lifetimes–on the order of picoseconds to less than a femtosecond. Chapter 5 will focus on two autoionization resonances (the $5s5p^6 6p$ and the $5s5p^6 7p$) visible as a Fano resonance in the absorption spectrum of gas phase xenon. The measurements elucidate several experimental requirements and allow direct measurement of the lifetimes of the states. The ultimate goal of these experiments is to understand lifetime recovery in a relatively simple atomic system, and to apply the experimental and analytical insight to measurements of more complicated molecular targets.

Chapter 2

Experimental principles and details

2.1 Experimental overview

Few-cycle laser pulses (with a central wavelength of 780 nm) are used to make isolated attosecond pulses via high harmonic generation with double optical gating. The attosecond pulses are used for time-resolved photoelectron spectroscopy and transient absorption spectroscopy with attosecond time resolution.

2.2 Attosecond spectroscopy instrument

2.2.1 Laser system

The layout on the optical table is shown in Figure 2.1. Few-femtosecond laser pulses are generated with the output of a commercial titanium:sapphire chirped-pulse amplifier system (FemtoPower HE by Femtolasers Inc.) which has a pulse duration of $20 - 25$ fs, and a pulse energy of 2 mJ at a 1 kHz repetition rate. The laser system has the capability to produce waveform controlled pulses, where the offset between the oscillations of the carrier frequency and the pulse envelope is locked.

Laser oscillator

The laser oscillator (Rainbow by Femtolasers Inc.) is a confocal cavity, with a titanium:sapphire crystal as the lasing medium. The crystal is pumped by a 532 nm, 3.0 W continuous wave laser (Verdi V6 by Coherent Inc.). Typical continuous wave power of the oscillator is 420 mW, and mode locked power is 180 mW. While mode locked, the oscillator operates at 78.58 MHz with a nominal pulse duration of less than 10 fs. The oscillator incorporates dispersive mirrors (both intra- and extra-cavity) to optimize the pulse compression. The bandwidth of the laser pulse extends from 650 nm to 1100 nm. The pulses are directed into a periodically-poled lithium niobate (PPLN) crystal for difference frequency generation of light at approximately 1040 nm. The overlapping portion of the fundamental spectrum and

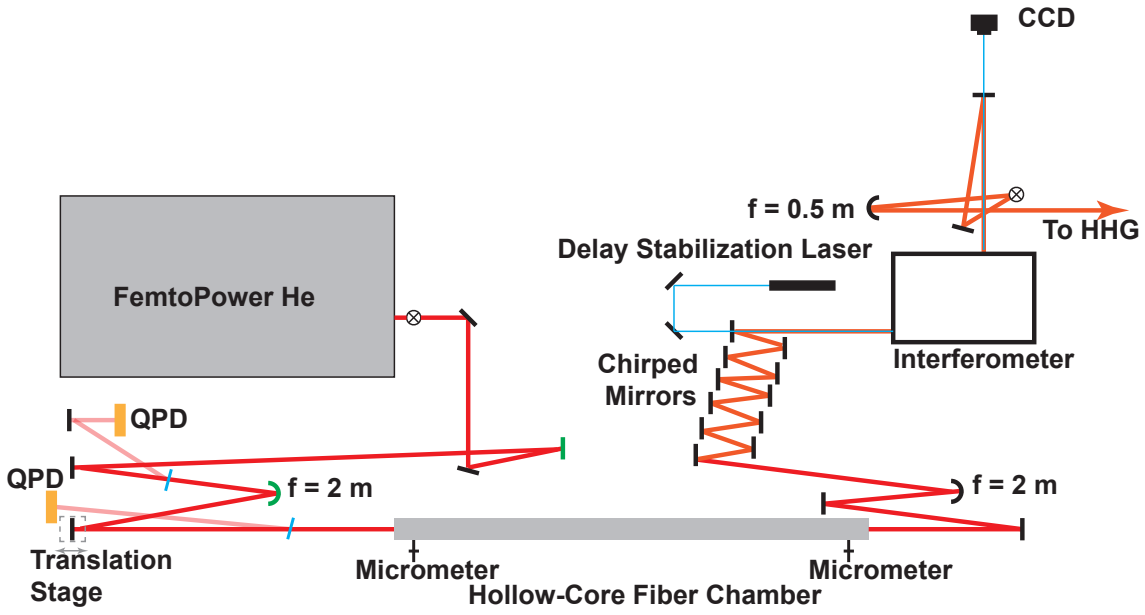

Figure 2.1: The output of the commercial chirp-pulse amplifier (25 fs, 2 mJ per pulse, 1 kHz) is directed into a 300 μm inner diameter 1 m long hollow fiber waveguide(filled with 2 bar neon gas) for spectral broadening. The resulting pulse travels to a chirped mirror compressor, which compensates the significant positive dispersion imparted into the pulse. The pulse then is sent to the interferometer, which controls delay between the attosecond pulse and optical pulse, and finally focused by an $f = 50$ cm spherical mirror into the HHG cell.

the difference frequency light are transmitted through a dichroic mirror to a fast photodiode, while the remaining light is sent to the multipass amplifier.

Fast loop

The transmitted light is used for the first stage of carrier-envelope phase control, the fast loop. The Fourier transform of the signal from the fast photodiode has peaks corresponding to the repetition rate (f_{rep}) of the oscillator as well as peaks from the beating between the difference frequency light and the fundamental spectrum of the oscillator. The beating is at the carrier-offset frequency (f_{ceo}), because the fundamental spectrum of the laser is a frequency comb with peaks separated by f_{rep} and offset from zero by f_{ceo} and the difference frequency spectrum has no offset frequency [39, 78]. The signal from the fast photodiode is sent through a band-pass filter that transmits frequencies close to f_{ceo}. The filtered signal at f_{ceo} and a signal at f_{rep} (measured with a separate photodiode) are sent to homemade phase locking electronics (from JILA) to stabilize f_{ceo} relative to f_{rep}.

The locking electronics have been described in detail previously [78–80]. A phase detector compares f_{ceo} to f_{rep} and the phase difference is sent to a proportional-integral-derivative

control loop to produce an error signal. A fast summing device combines the error signal with the error signal from the second stage of carrier-envelope phase control. The total error signal is sent to an acoustic optical modulator that modulates the pump laser power to lock f_{ceo} relative to f_{rep}. The modulations in pump laser power change the ratio of the index of refraction for the carrier wave to the index of refraction for the envelope and allow f_{ceo} to be stabilized relative to f_{rep}.

Multipass amplifier

The oscillator pulse train is sent through a stretcher before entering the titanium:sapphire multipass-amplifier cavity, pumped by a neodymium-doped yttrium lithium fluoride solid state laser (527 nm; 200 ns; $17 - 19$ W). The multipass cavity has total of ten passes. The gain after four passes is $\sim 10,000$. After the fourth pass a single pulse from the oscillator pulse train is selected by a Pockels cell that is triggered (at a 1 KHz repetition rate) to only pass a pulse with a consistent carrier-envelope phase. The selected pulse is sent though an acousto-optic programmable dispersive filter (Dazzler by FastLite), which allows a user-specified spectral phase to be added to the laser pulses for optimum pulse compression [81]. The selected pulse is further amplified by the subsequent six passes in the amplifier cavity. The final power after the ten passes is ~ 2.5 W. After the amplifier, the pulse is compressed with a grating compressor. The resulting output has a pulse energy of 2 mJ at 1 KHz and a pulse duration of $20 - 25$ fs.

Slow loop

A portion of the laser pulse is picked off by a fused silica plate and directed to an f to $2f$ interferometer for the second stage of carrier-envelope phase control (the slow loop). In the f to $2f$ a continuum spectrum is generated by focusing the pulse into a sapphire plate, and the white light is frequency doubled by a β-barium borate (BBO) crystal. Both the fundamental spectrum and the second harmonic are sent into a spectrometer. Fringes in the spectrum are visible in the high frequency portion of the spectrum that correspond to the carrier-envelope phase. The fundamental white light spectrum has a spectral phase of $\phi_{WL}(\omega) + \phi_{CEP}$ and the second harmonic has a spectral phase of $\phi_{SH}(\omega) + 2\phi_{CEP}$ (where ϕ_{WL} and $\phi_{SH}(\omega)$ are the spectral phases, excluding carrier-envelope phases, of the white light and second harmonic, respectively). The combined spectral intensity will have a term that is proportional to the cosine of ϕ_{CEP} [39, 78]. The spectral fringes are recorded by a charged coupled device (CCD) camera at a rate of ~ 30 Hz coupled to a PC for control by a Labview proportional-integral-derivative control loop. The feedback signal from the second stage of carrier-envelope phase control is combined with the signal from the first stage by a fast summing device and sent to the acoustic optical modulator.

Few-cycle pulse generation

Few-cycle pulses are generated from the $20-25$ fs output of the laser amplifier. The laser pulses are focused by an $f = 2$ m focusing mirror into a 1 m long, 300 μm inner diameter hollow-core fiber filled with 2 bar neon gas to produce a supercontinuum via self-phase modulation [68, 82]. The focusing optics are chosen so that the focal spot of the near-infrared (NIR) laser (twice the beam waist) at the entrance of the fiber is approximately 64% of the inner diameter of the fiber, to ensure best transmission [83]. The intense laser pulses cause a time-varying index of refraction in the neon gas, resulting in a non-constant instantaneous phase that introduces new frequencies into the laser spectrum [84]. The stainless steel fiber enclosure is designed so that the entrance and exit windows (1 mm thick fused silica windows coated on both faces with a broad-band anti-reflective coating) are approximately 40 cm from the entrance and exit of the fiber; at this distance the beam diameter is large enough to prevent high order phase effects occurring in the windows. The pulse spectrum recorded directly after the laser and after the hollow fiber is shown in Figure 2.2(a-b).

Daily optimization of the fiber is performed by adjusting the micrometers at either end of the fiber enclosure so that the output of the fiber has a Bessel mode when observed on a card as shown in Figure 2.2(c), and so that the fiber transmission is approximately 60%. Less frequent optimization of the fiber involves moving the mirror on a translation stage (see Figure 2.1), which will translate the focal position at the entrance of the fiber. The second order phase terms applied by the Dazzler in the laser amplifier may also be adjusted to optimize the output of the fiber.

The transmission of the fiber is highly sensitive to the beam pointing, so the beam path from the femtosecond laser is actively stabilized using a stabilization apparatus from MRC systems (Germany) with two quadrant photodiodes and two actuated mirrors to monitor and correct beam pointing fluctuations. Monitoring and stabilizing the position at two points on the beam path allows a constant beam path to be maintained throughout the day.

Following the fiber, the beam is recollimated with an $f = 2$ m focusing mirror and directed to a set of chirped mirrors in order to compress the pulse before entering the compact interferometer. The chirped mirrors introduce negative dispersion to the pulse, to not only compensate the positive dispersion from the spectral broadening in the hollow fiber, but also to compensate any positive dispersion added by the optics and optical path length before harmonic generation in the vacuum [85].

Pump and probe pulse separation

The interferometer (pictured in Figure 2.3) utilizes annular hole mirrors to spatially separate the beam into two parts for pump-probe measurements [54]. The inner portion of the beam is the HHG driving pulse and has a pulse duration of 7 fs, while the outer ring is used as the optical pulse in the attosecond pump-probe measurements and has a pulse duration of 12 fs when optimally compressed. The difference in pulse duration is a consequence of spectral broadening by a hollow-core fiber, which is less efficient and less consistent near the edges of the beam [86]. Spatial separation of the inner and outer portions

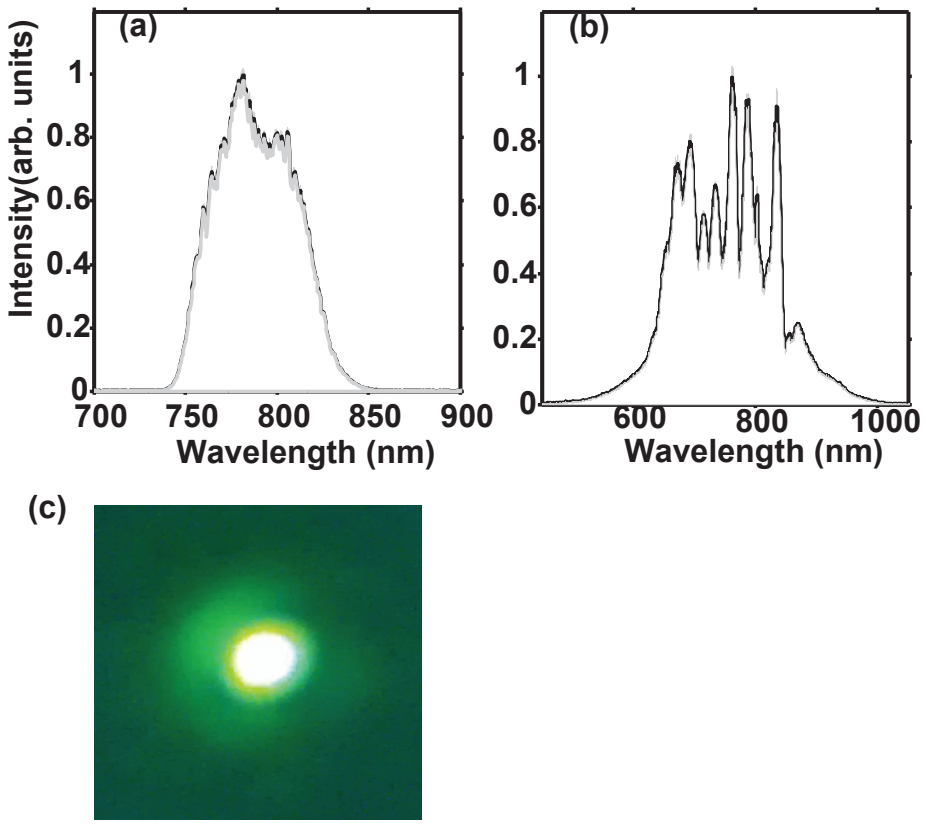

Figure 2.2: Spectra of laser before and after hollow core fiber. (a) Spectrum recorded after laser amplifier system. The black trace is the average of five spectra each integrated for 100 ms, the gray area is the ± one standard deviation. (b) Spectrum recorded after hollow core fiber. The black trace is the average of five spectra each integrated for 100 ms, the gray area is ± one standard deviation. (c) Photograph of beam spot after transmission through hollow fiber. The beam is attenuated with an OD = 3 metallic neutral density filter, and a laser goggle (filter style 070 by Sperion) is placed in front of the camera.

of the beam results in one spatially chirped pulse that is difficult to compress. The pulse durations measured with SPIDER [87] are plotted in Figures 2.4-5.

At the exit of the interferometer the harmonic driving pulse and the optical pulse are not compressed. The harmonic driving pulse will be compressed after transmission through the 1 mm thick fused silica window that is the entrance to the vacuum. The optical pulse will be compressed after transmission though the window and an additional annular piece of fused silica mounted in the vacuum after the HHG cell. This ensures that the optical pulse has a long pulse duration (and low intensity) when it passes through the HHG cell, so that it will not interfere with harmonic generation. Due to the difference in group-delay dispersion at the HHG cell, the optical pulse arrives at the cell $\sim 1-2$ ps before the harmonic driving

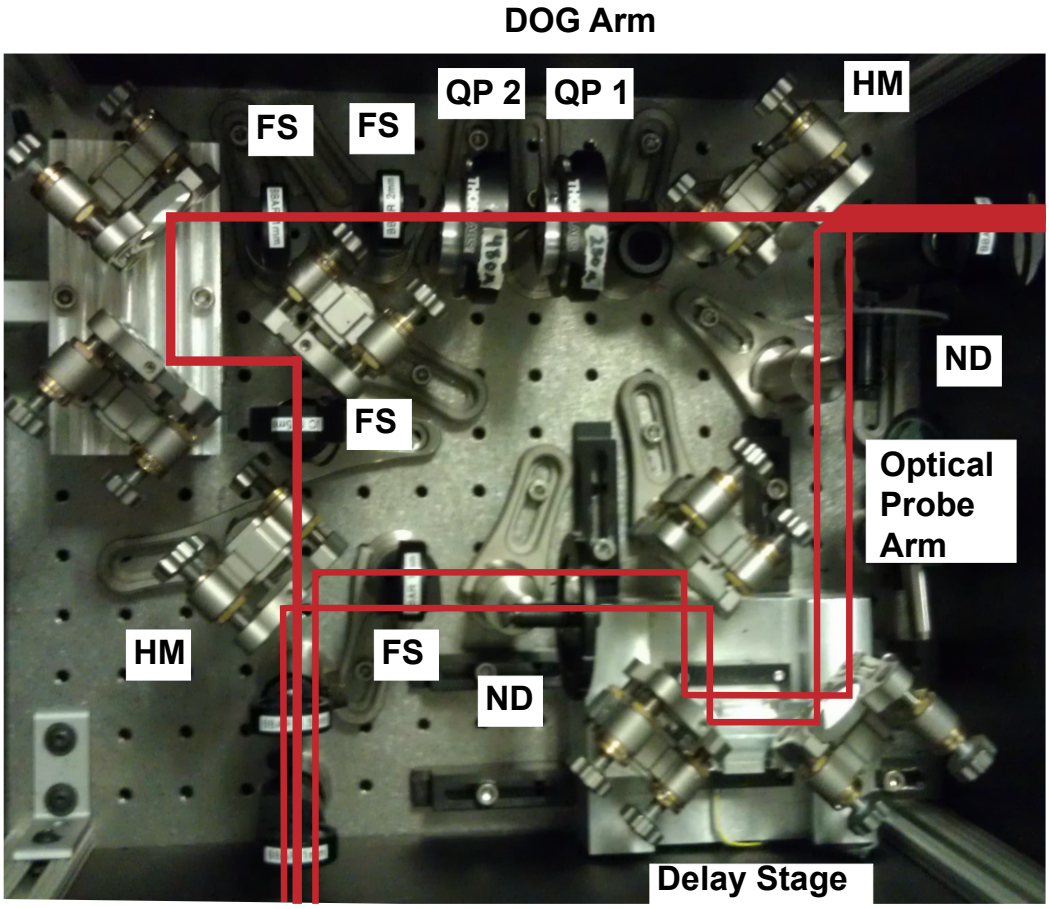

Figure 2.3: Interferometer. Hole mirrors (HM) separate and recombine the pump and probe arms. The quartz plates (QP1 and QP2) are used for double optical gating. The fused silica (FS) is inserted for best pulse compression. Metallic neutral density filters (ND) control the intensity of the optical arm. The NIR beam enters at the upper right hand side of the photograph and exits at the bottom left side. The long term drift of the interferometer is actively stabilized with a homebuilt feedback loop to ~ 50 as rms jitter over 24 hours.

pulse. Transmission through a final piece of fused silica applies sufficient positive dispersion to the optical pulse so that it is compressed and overlapped in time with the attosecond high harmonics [54].

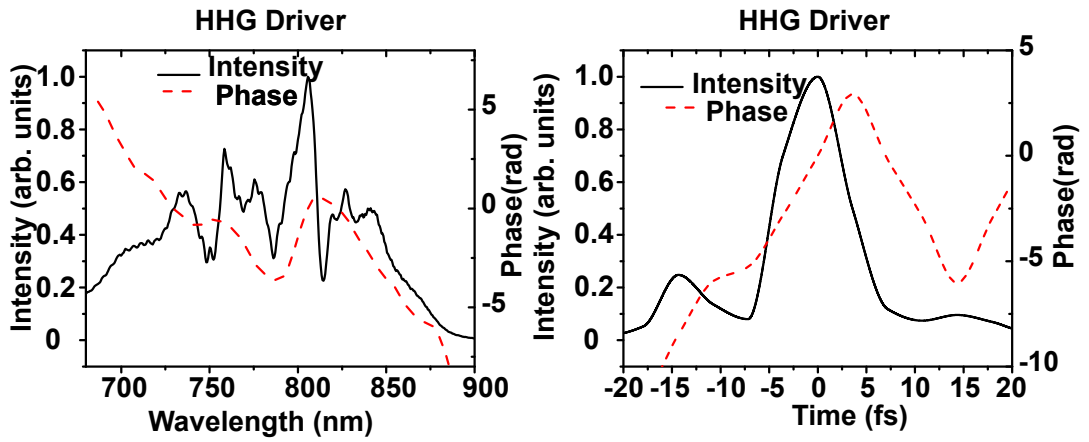

Figure 2.4: The spectrum and phase of the HHG driver pulse (left) and the temporal profile and phase (right) retrieved from SPIDER measurements. The pulse duration is 7 fs.

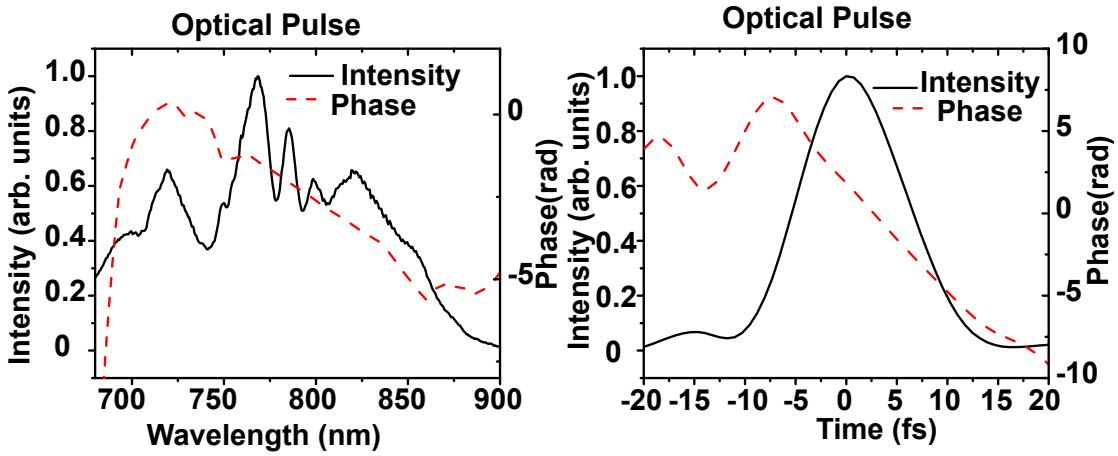

Figure 2.5: The spectrum and phase of the NIR optical pulse (left) and the temporal profile and phase (right) retrieved from SPIDER measurements. The pulse duration is 12 fs.

2.2.2 Vacuum apparatus

A schematic for the vacuum apparatus is shown in Figure 2.6. High harmonic generation takes place in the first vacuum chamber. The second chamber houses a mechanical iris, fitted with motorized actuators, for alignment of the system. A charged coupled device (CCD) camera is installed inside the iris chamber so that the beam pointing may be checked and optimized in vacuum. The main interaction chamber contains the annular filters to select the XUV spectrum, the XUV focusing optics, the interaction volume, and photoelectron time-of-flight. The final chamber is the spectrometer with a concave grating and blacklit X-Ray CCD camera to disperse and record the spectra of the attosecond pulse, respectively.

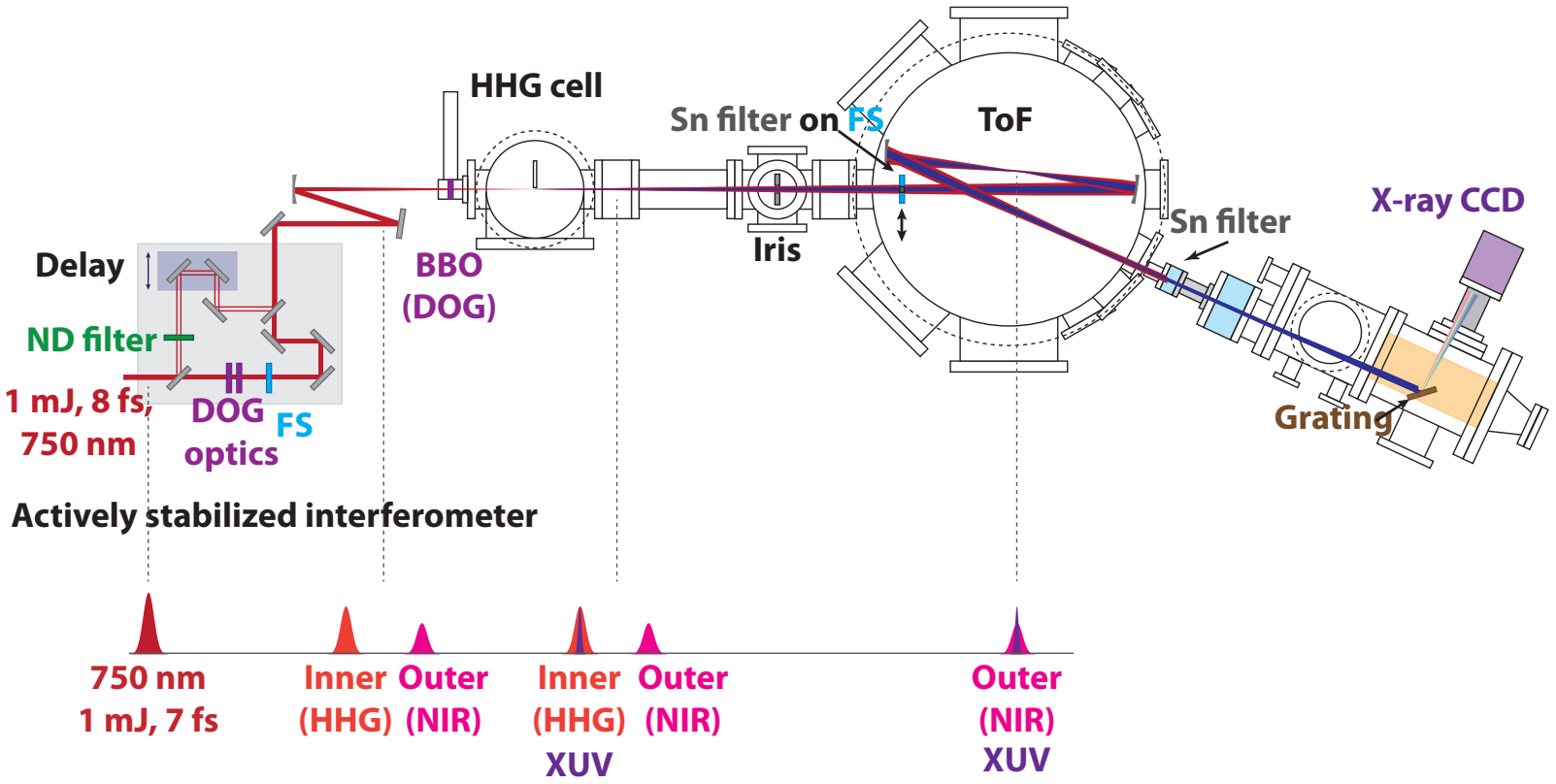

Figure 2.6: Diagram of the experimental vacuum system. High harmonics are generated in the first chamber. A mechanical iris in the second chamber is used for alignment. The residual NIR light is filtered using a metal filter in the third chamber (main interaction chamber). A 2 in diameter spherical focusing mirror focuses the attosecond pulses and the NIR pulses into the center of the main interaction chamber. A gas jet is installed for photoelectron time-of-flight measurements or a gas cell is installed for absorption measurements. The photoelectron time-of-flight is installed 1.5 cm from the center of the main chamber coming out of the page. The fourth chamber is a spectrometer for measuring the spectrum of the attosecond pulse.

2.2.3 DOG and harmonic generation

Double optical gating (DOG), the combination of two-color gating and polarization gating, is used to make isolated attosecond pulses [51, 52, 88]. The total field of the pulse used for harmonic generation has a time-dependent ellipticity and can be separated into two orthogonal components: the driving field (E_{drive}), which generates harmonics and the gating field (E_{gate}), which suppresses harmonic production. The driving field and the gating field are given by:

$$E_{drive}(t) = E_0\epsilon\left[e^{-2ln(\frac{t-T_d/2}{t_p})^2} + e^{-2ln(\frac{t+T_d/2}{t_p})^2}\right] cos(\omega_0 t + \phi_{ce}) \tag{2.1}$$

and

$$E_{gate}(t) = E_0\epsilon\left[e^{-2ln(\frac{t-T_d/2}{t_p})^2} + e^{-2ln(\frac{t+T_d/2}{t_p})^2}\right] sin(\omega_0 + \phi_{ce})(-1)^n \tag{2.2}$$

where E_0 is the field amplitude, ϵ is the ellipticity ($\epsilon = 1$ for circularly polarized light), T_d is the time delay between the two counter-rotating pulses and an integer (n) multiple of the optical period of the input pulse (2.6 fs), t_p is the pulse duration of the input pulse, ω_0 is the carrier frequency of the input pulse, and ϕ_{ce} is the carrier-envelope phase of the input pulse [39, 51]. The time delay, T_d between the two counter-rotating pulses can be estimated from:

$$T_d = L(\frac{1}{v_{eg}} - \frac{1}{v_{og}}) \tag{2.3}$$

where L is the thickness of the first quartz plate, v_{eg} and v_{og} are the group velocities of the extraordinary and ordinary rays [39]. The driving and gating fields for the conditions herein are plotted in Figure 2.7. The gate width, the time interval over which harmonic recombination is permitted, is 1.8 fs, so only one attosecond pulse will be produced even if the driving field is not phase stabilized [89]. This is in contrast to other isolated attosecond pulse generation methods where the carrier-envelope phase of the pulse must be stabilized to produce isolated attosecond pulses.

The optical axis of the second quartz plate is oriented parallel to the laser polarization (45° relative to the two time delayed copies of the laser pulse). The second quartz plate and the 150 μm thick type I β-barium borate (BBO) crystal together act as a zero-order quarter-wave plate. This is possible because the BBO is a negative uniaxial crystal (the extraordinary axis has a smaller index of refraction than the ordinary axis), while the quartz plate is a positive uniaxial crystal (the extraordinary axis has the larger index of refraction). The effect of the quarter-wave plate is to convert the extraordinary and ordinary pulses into right- and left-circularly polarized pulses. The BBO also generates the second harmonic with polarization parallel to the initial input pulse according to type I phase matching conditions [39]. The BBO must be located inside the vacuum system because transmission through the fused silica window at the entrance of the vacuum system would introduce different amounts of dispersion to the $\sim$ 400 nm second harmonic and $\sim$ 800 nm fundamental pulses. The phase matching angle of the BBO is adjusted on a daily basis to produce the most continuous

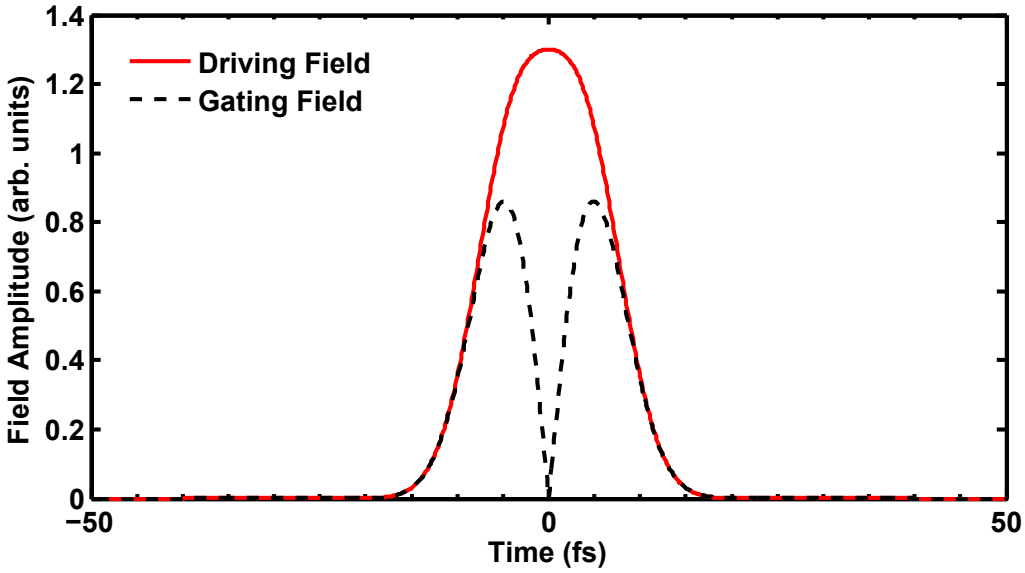

Figure 2.7: The DOG fields for a 7 fs input pulse and 8 fs delay between the counter-rotating pulses. The driving field (red solid) generates the attosecond pulses and the gating field (black dashed) suppresses harmonic recombination. A 250 μm thick quartz plate produces the delay between the counter-rotating pulses.

harmonic spectrum. The DOG optics are diagrammed in Figure 2.8. Because the BBO is in-line with the beam axis of the optical beam, it is possible to generate 400 nm optical pulses for use in streaking experiments, by introducing a half-wave plate to rotate the polarization of the optical beam by 90°, so that type I phase matching conditions produce 400 nm second harmonic in the optical pulse with polarization parallel to the harmonic driving field [54].

An $f = 50$ cm spherical mirror focuses the DOG pulse in the harmonic generation cell. The focal spot size (twice the beam waist) is approximately 70 μm and the estimated peak intensity is up to 3.5×10^{15} W/cm^2. The cell consists of a stainless steel tube (inner diameter: 3.2 mm, wall thickness: 0.8 mm) with 0.5 mm holes drilled on opposite sides of the tube to allow the beam to pass though. Teflon tape is wrapped around the cell, and drilled by the focused laser beam to produce the smallest possible holes in the harmonic generation cell. The harmonic cell can be retaped and redrilled in less than one hour, so retaping the cell for consistent harmonic generation may be done as frequently as necessary (typically once a month). Changes in the laser beam pointing may allow the laser to enlarge the apertures in the Teflon tape. The harmonic cell is placed after the $\sim$3 mm long focus so that only the short trajectories produce harmonics [68].

The typical harmonic spectra using argon (7 Torr) and krypton (2 Torr) as the harmonic

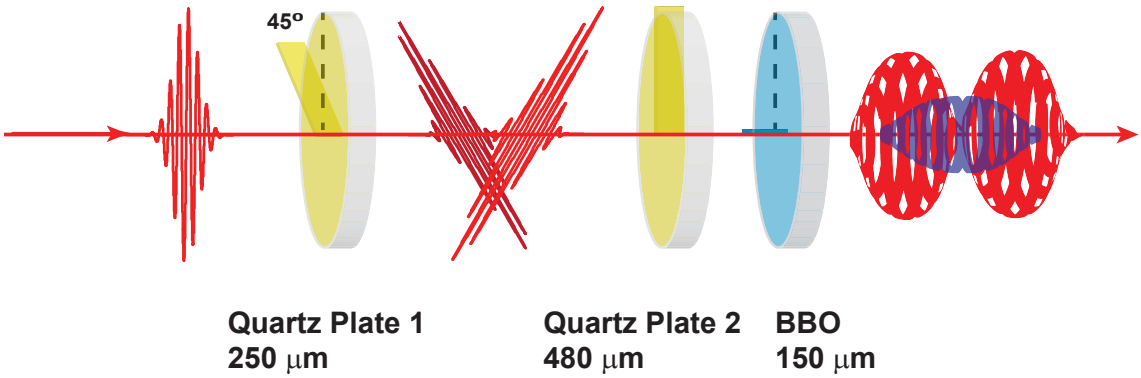

Figure 2.8: The DOG optics for use in the current experiments. A 250 μm quartz plate produces a delay between two orthogonally polarized pulses. A 480 μm quartz plate and 150 μm BBO act together as a quarter-wave plate to produce two counter-rotating circularly polarized pulses.

generating gases are plotted in Figure 2.9 and Figure 2.10. The spectra for femtosecond pulse trains of attosecond pulses have characteristically modulated spectra with peaks separated by $\sim$3 eV corresponding to the optical half-period of the driving laser (1.3 fs), while the spectra for isolated attosecond pulses are continuous. Aluminum and tin (both 200 nm thick) metal filters are used to reflect the residual NIR light from the HHG driving pulse, and to select the XUV spectrum. As shown in Figure 2.9, DOG supports attosecond pulses with a broad spectral range ($\sim$20 to 50 eV), but for experiments it may be desirable to select certain energy ranges to excite certain atomic and molecular transitions. The filters are mounted in annular 2 in diameter fused silica plates (1 mm or 2 mm thick) designed to transmit the optical pulse through the fused silica, and the attosecond XUV pulse thorough the metal foil. The fused silica imparts positive dispersion to the optical pulse and produces optimally compressed pulses. Typical harmonic flux is $\sim 10^5$ photons per laser pulse.

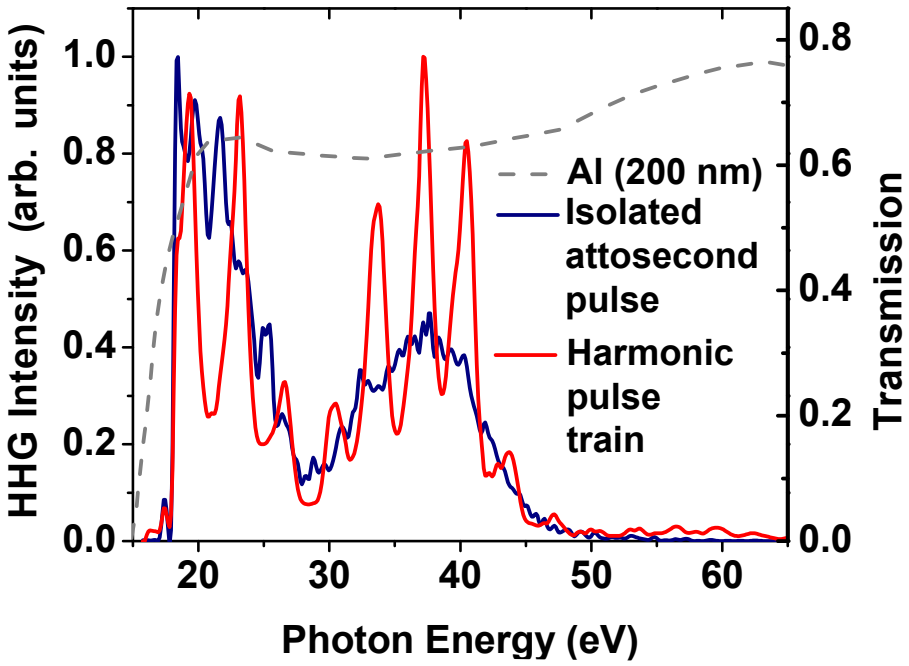

Figure 2.9: Typical harmonic spectrum measured without double optical gating (red trace) and with double optical gating (blue trace). The harmonic spectrum without double optical gating is modulated with peaks separated by 3 eV, corresponding to a train of attosecond pulses spaced in time by the optical half period of the driving laser (1.3 fs). The spectrum recorded with double optical gating is continuous. Argon gas at a pressure of 7 Torr is the harmonic generating medium. The residual NIR light from the HHG driving laser is filtered from the XUV high harmonics with a 200 nm thick aluminum foil. The transmission of the aluminum foil is plotted in gray [90]. The harmonic spectrum is measured from the photoelectron spectrum of neon gas (Ip = 21.56 eV). The dip in the spectrum near 30 eV corresponds to decreased reflectivity of the XUV focusing optic.

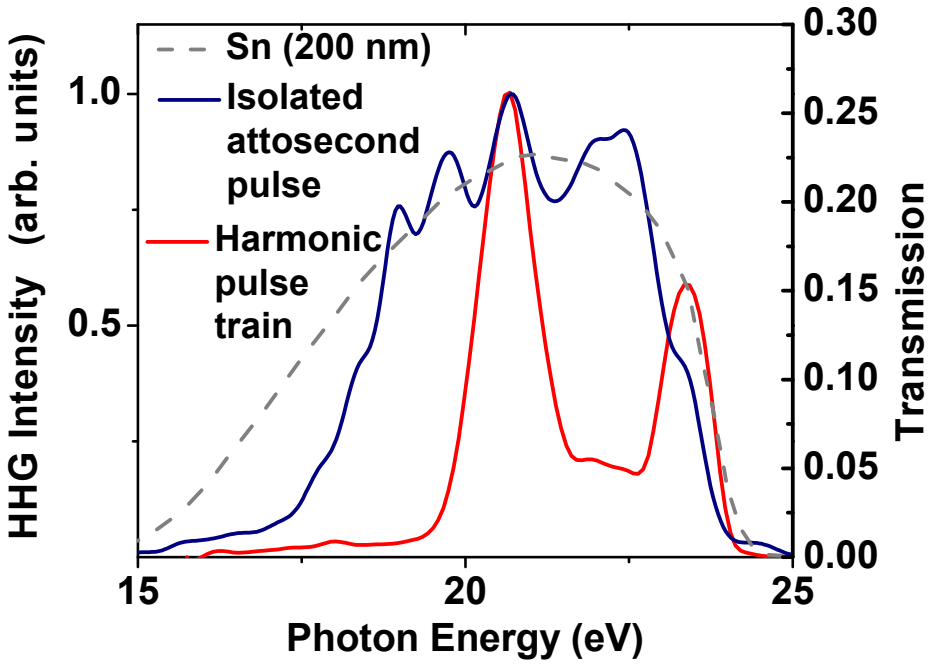

Figure 2.10: Typical harmonic spectrum measured without double optical gating (red trace) and with double optical gating (blue trace). Krypton gas at a pressure of 2 Torr is the harmonic generating medium. The residual NIR light from the HHG driving laser is filtered from the XUV high harmonics with a 200 nm thick tin foil. The transmission of the tin foil is plotted in gray [90]. The harmonic spectrum is measured from the photoelectron spectrum of argon gas (Ip = 15.76 eV).

2.2.4 Photoelectron time-of-flight

The duration of attosecond pulses is determined using photoelectron streaking [59, 91], which necessitates a method for determining momenta (or alternatively kinetic energies) of photoelectrons. A field-free photoelectron time-of-flight (TOF) is used to measure the kinetic energies of photoelectrons based on their arrival time at a detector. The technique requires that the electrons be generated at a well-defined staring position and travel a known distance to a detector [92]. The kinetic energy (KE) of the electron is given by:

$$KE = \frac{1}{2} m_e v_e^2 = \frac{1}{2} m_e (\frac{d}{t})^2 \tag{2.4}$$

where m_e is the mass of an electron, v_e is the velocity of the electron, d is the distance the electron travels to the detector, and t is the measured flight time. In the absence of the optical streaking field the kinetic energies of the photoelectrons are given by:

$$KE = \hbar\omega - BE \tag{2.5}$$

where $\hbar\omega$ is the photon energy of the incident pulse and BE is the electron binding energy [92]. The kinetic energies of photoelectrons ionized by an attosecond pulse will have a broad distribution corresponding to the broad spectrum of the attosecond pulse. For the experiments described here, electrons travel the 74.4 cm field-free flight tube from the interaction region to a chevron micro-channel plate (MCP) detector (Jordon TOF Products, Inc.). The MCP has a circular active area (diameter 40 mm) and a solid angle of 2.4×10^{-5} sr. The micro-channel plates are ceramic disks with 25 μm diameter channels, coated with a low work function material. When incident electrons strike the plates, electrons propagate down the channel towards an anode due to an applied electric field. For typical operation the grid in front of the MCP is grounded, the front face of the first MCP plate is at +200 V, the rear face of the first plate and the front face of the second plate is set to +1200 V, the rear face of the second plate is set to +2200 V, and the anode at +2400 V. The negative voltage spike produced from the incident electrons is capacitively coupled out and is sent to an analog constant fraction discriminator (Fast ComTec) to limit timing errors (estimated as 3 ns) caused by non-uniform pulse shapes. Timing jitter on the ns timescale is particularly important because the flight time for photoelectrons with 50 eV of kinetic energy is approximately 180 ns. The signal from the constant fraction discriminator is sent to a multichannel scaler card (Fast ComTec) for computer acquisition. The bin width on the multichannel scaler is set to 1 ns (the smallest bin width the scaler card supports).

A schematic for the TOF is shown in Figure 2.11. The TOF is installed in the center of the main interaction chamber shown in Figure 2.6. In Figure 2.6, the TOF axis is perpendicular to the page. A skimmer cone with a aperture diameter of 0.5 mm separates the TOF flight tube from the main interaction chamber; this allows the TOF flight tube to maintain a lower pressure than the main interaction chamber during experimental measurements. Typical pressures are 5×10^{-5} Torr and 1×10^{-6} Torr, in the main interaction chamber and the time-of-flight chamber, respectively. The flight tube of the TOF is shielded with mu-metal

(a material with a high magnetic permeability), to prevent stray fields (for example, from the geomagnetic field or fields from stainless steel vacuum components) from altering the flight time of the electrons. Brass apertures inside the flight tube prevent low kinetic energy secondary electrons (released when photoelectrons with high kinetic energies strike the metal flight tube) from reaching the detector. Brass components are used because they do not have a magnetic field.

The effusive gas jet used in experiments is a 50 μm inner diameter capillary. The small aperture jet allows high target densities ($\sim 10^{13}$ molecules/cm^3) near the exit of the jet, without deteriorating the vacuum conditions of the main chamber. The target density drops off rapidly, which limits ionization of the target gas by the attosecond pulse to a small fraction of the NIR focal volume. This is necessary for photoelectron streaking measurements, which rely on the instantaneous NIR field strength, because spatial averaging effects and the so-called Gouy phase slip across the focus are detrimental to accurate measurements [8, 93]. The homemade jets are constructed by affixing a steel capillary inside a $\frac{1}{4}$ in to $\frac{1}{16}$ in Swagelok reducing union with expoxy. Care is taken to ensure that the capillaries are aligned parallel relative to the Swagelok fittings. Silver epoxy, applied to the jets after the epoxy has set and cured, ensures that the capillaries have electrical connectivity to the body of the jet. Gas jets are tested for leaks and blockages with compressed gas prior to installation. A photograph of the jets is shown in Figure 2.12.

A typical kinetic energy spectrum is shown in Figure 2.13, where the raw TOF spectrum is converted to kinetic energy using Equation 2.4, and multiplying by the Jacobian given below:

$$\frac{-d\sqrt{m_e}}{2\sqrt{2}} \times KE^{-3/2} \tag{2.6}$$

Typically, spectra are acquired for 3×10^4 laser pulses (or 30 seconds of integration time at 1 kHz repetition rate). The integration time may be increased to 60 seconds or decreased to 20 seconds depending on conditions including harmonic efficiency and atomic or molecular ionization cross section. The experimental resolution is 1% for photoelectrons with 50 eV of kinetic energy. The resolution ($\frac{\Delta E}{E}$) for time of flight measurements is given by:

$$\frac{\Delta E}{E} = \frac{2\Delta T}{T} \tag{2.7}$$

where ΔT is the time resolution (in this case 1 ns from the bin width of the multichannel scaler card), and T is the measured flight time.

Time-of-flight alignment

For typical alignment (with all vacuum chambers vented to atmospheric pressure), the beam path of the NIR laser (attenuated with an OD 2 metallic neutral density filter) is set at the center of the BBO in the HHG chamber and the iris in the vacuum. The focus at the interaction region along the beam axis is found using the plasma generated at the focus. A translation stage under the spherical focusing mirror is adjusted until the focus is centered

under the TOF skimmer. Motorized actuators on the spherical mirror mount are used to align a low power NIR beam in the axis perpendicular to the beam axis. The placement is found by observing (with a dentist's mirror, flashlight, and IR viewer) the scattered NIR light on the skimmer aperture and adjusting the mirror pointing until the scattered light symmetrically illuminates the aperture (see Figure 2.14). The skimmer aperture must appear centered below the TOF flight tube and circular to the viewer while aligning or the alignment will be off center. The alignment along the beam axis and perpendicular to the beam axis must be iterated until the focus is consistently centered. Once the beam has been aligned to the cone, the beam is lowered using the vertical actuator on the focusing mirror until the scattered NIR light on the cone is no longer observed. The gas jet is then aligned into the focus using an XYZ translation stage fitted with micrometers, until the tip of the jet is illuminated with scattered NIR light. Finally, the jet is translated perpendicular to the beam axis, until no scattered light is seen.

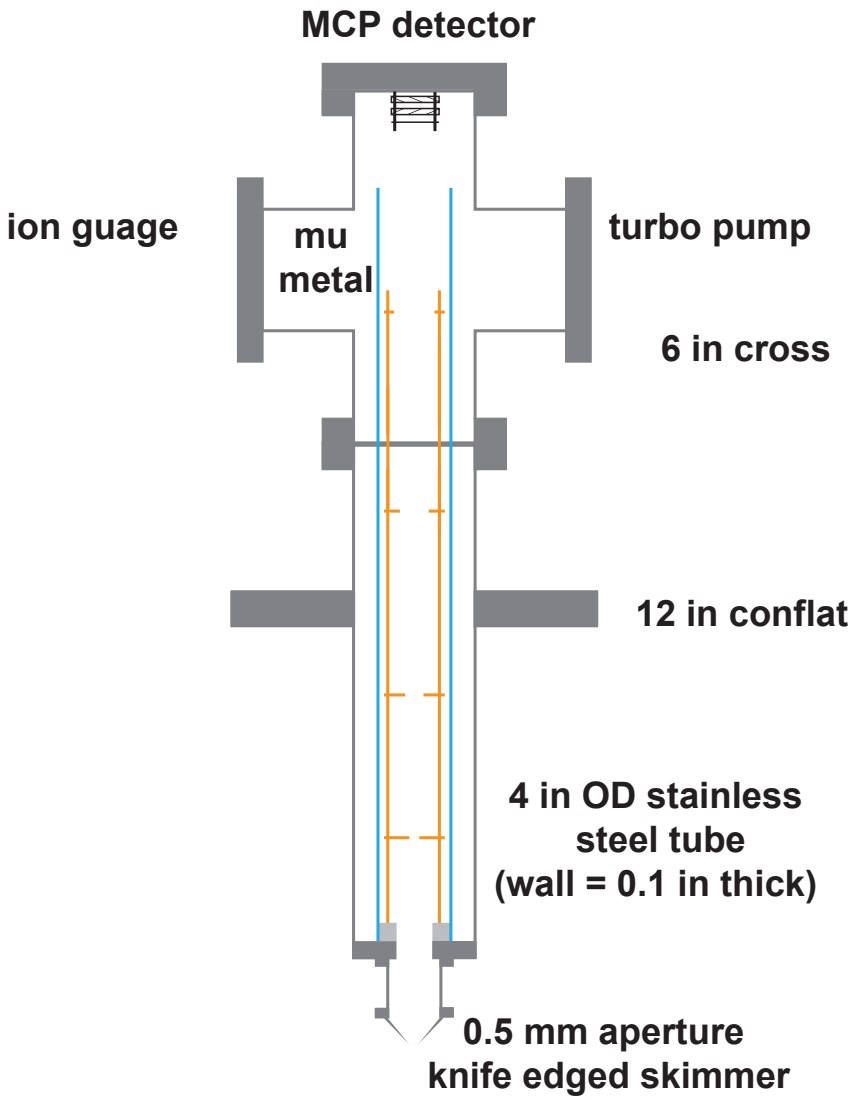

Figure 2.11: Schematic of photoelectron time-of-flight. The TOF has a 74.4 cm field-free flight tube, shielded from stray fields by a mu-metal tube (blue) that has been degaussed prior to installation. The aperture to the TOF flight tube is a 0.5 mm diameter skimmer. Brass apertures (yellow) limit the transmission of stray secondary electrons. An ion gauge and two turbo pumps (each 200 $\frac{l}{s}$) are installed on the 6 in cross to ensure that low pressure is maintained near the detector. The TOF is attached to the main interaction chamber via the 12 in conflat flange. To prevent the incoming and outgoing beams from being superimposed the TOF is offset from the center of the chamber by 1.5 cm.

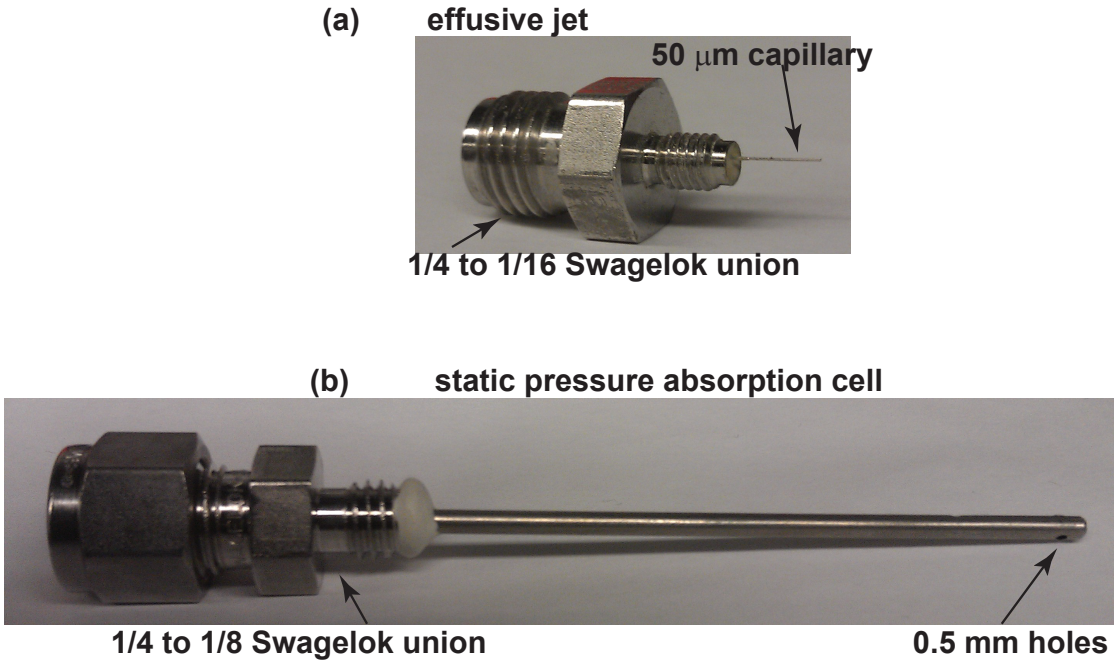

Figure 2.12: Gas jets for photoelectron (a) and transient absorption (b) measurements. Gas exits the effusive jet through a 50 μm capillary. The gas cell for absorption spectroscopy is a 1 mm stainless steel tube with half millimeter holes drilled. The holes are covered by scotch tape and drilled with the laser. Molecular targets with halogen atoms may react with the tape or adhesive and, as a result, will preclude the use of scotch tape on the absorption cell.

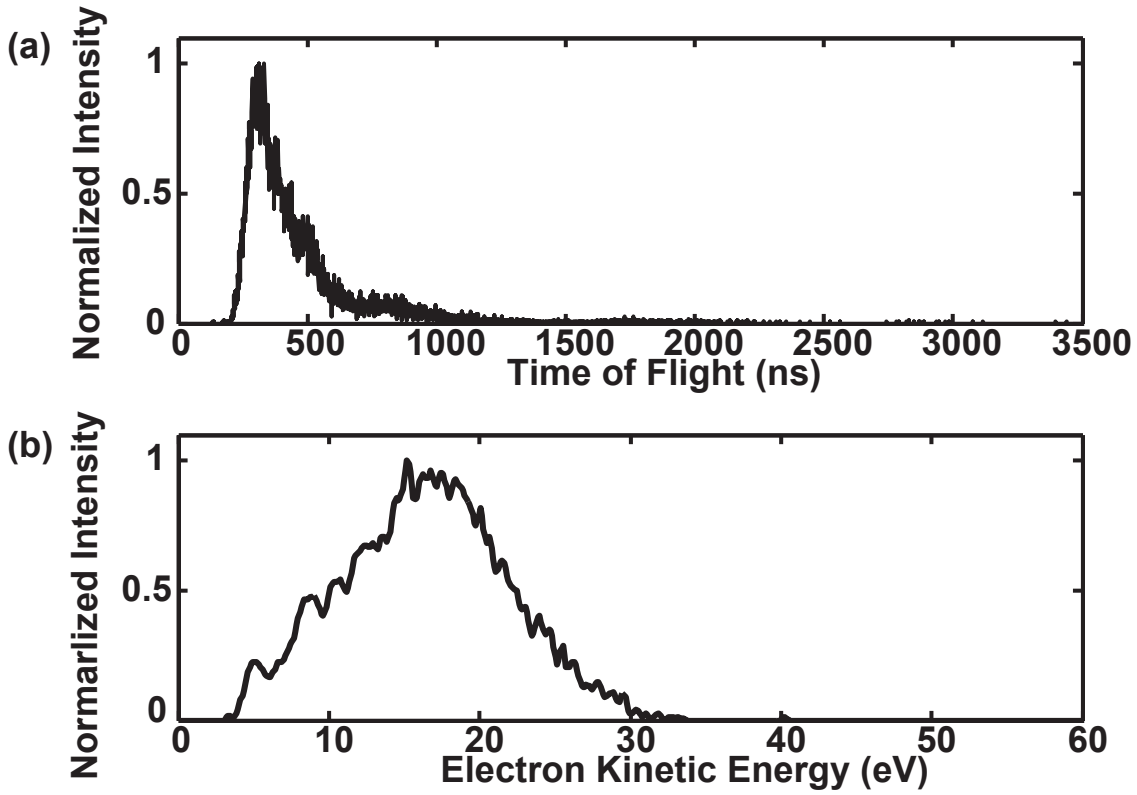

Figure 2.13: Typical raw (a) time of flight spectra for neon gas ionized by an attosecond pulse. The same time of flight data converted to electron kinetic energies (b). A 200 nm thick aluminum filter is used to reflect the residual NIR light. Spectra are recorded for 3×10^4 laser pulses.

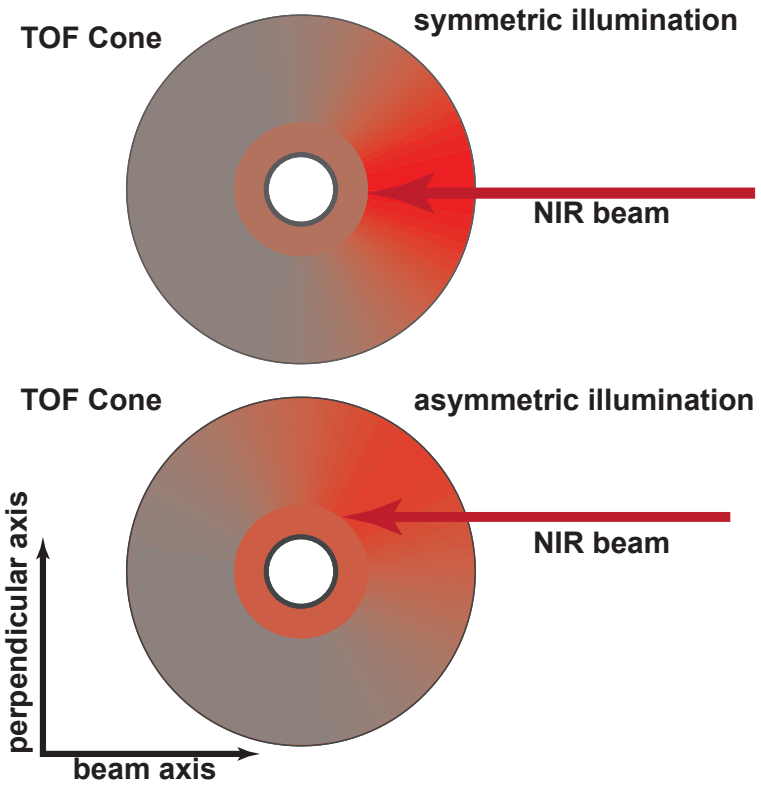

Figure 2.14: For correct alignment the cone should be symmetrically illuminated.

2.2.5 XUV optics

The XUV focusing optics are 2 in diameter, $f = 25$ cm super polished mirror substrates (Gooch and Housego) coated with multilayer coatings by either the Center for X-Ray Optics (CXRO at Lawrence Berkeley National Lab) or NTT Advanced Technologies (Japan). The multilayer coatings consist of alternating layers of materials with differing indices of refraction, for example alternating layers of molybdenum and silicon [94, 95]. The thickness of each bilayer (d) corresponds to the Bragg diffraction law at normal incidence:

$$d = \frac{\lambda}{2} \tag{2.8}$$

where λ is the wavelength reflected. As the number of bilayers increases the reflectivity of the coating increases, but the bandwidth the coating reflects becomes more narrow. The bandwidth (ΔE) of a multilayer mirror with a central reflectivity of E can be estimated as:

$$\frac{\Delta E}{E} = \frac{1}{N} \tag{2.9}$$

where N is the number of bilayers [96, 97]. For attosecond pulses, typical coatings of $10 - 20$ bilayers are used in order to produce broadband reflectivity. The reflectivity of the molybdenum/silicon multilayer coating obtained from the CXRO is plotted in Figure 2.15. The reflectivity and spectral phase of the molybdenum/silicon and the ruthenium/silicon multilayer coatings obtained from NTT Advanced Technologies are plotted in Figure 2.16 and Figure 2.17, respectively. Recent developments focusing on aperiodic multilayer mirrors designed to apply user-defined spectral phases to the attosecond pulses can produce nearly transform-limited attosecond pulses [97–99].

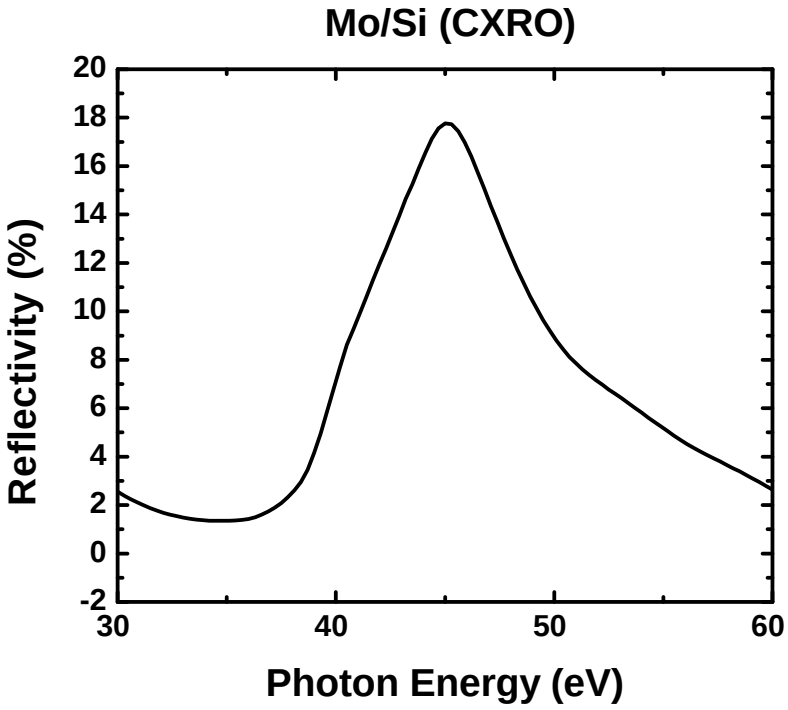

Figure 2.15: Reflectivity of molybdenum/silicon multilayer mirror coated by the CXRO. The reflectivity is centered at 45 eV, and a bilayer period of 14.8 nm is used. The reflectivity measurement is provided by the CXRO.

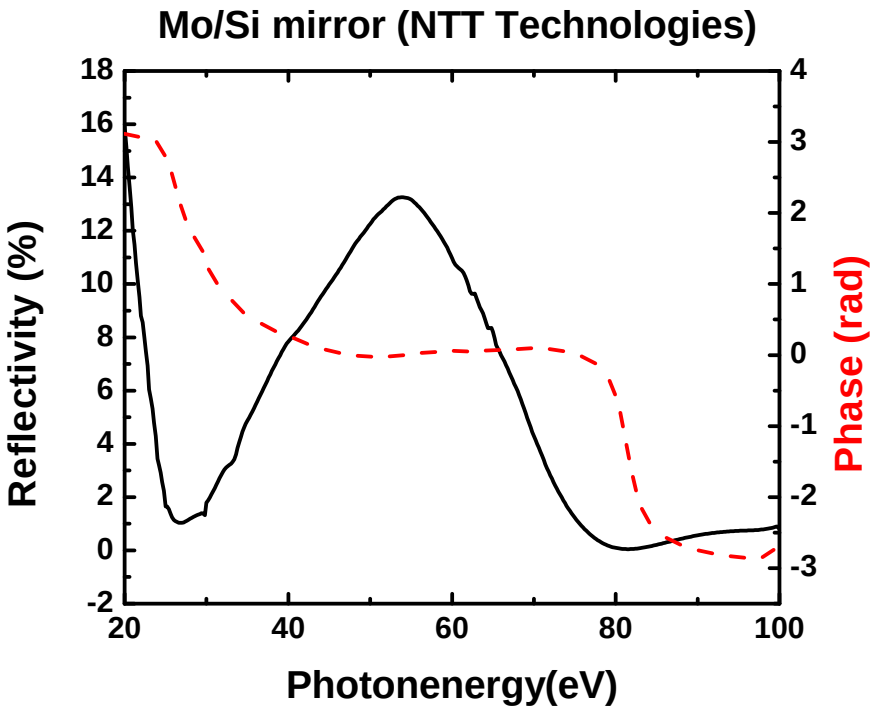

Figure 2.16: Reflectivity (black) and spectral phase (red) of molybdenum/silicon multilayer mirror coated by NTT Advanced Technologies. The reflectivity is centered at 53 eV and the coating has been optimized to impart minimal spectral phase to the attosecond pulse. The reflectivity and phase measurements are provided by NTT Advanced Technologies.

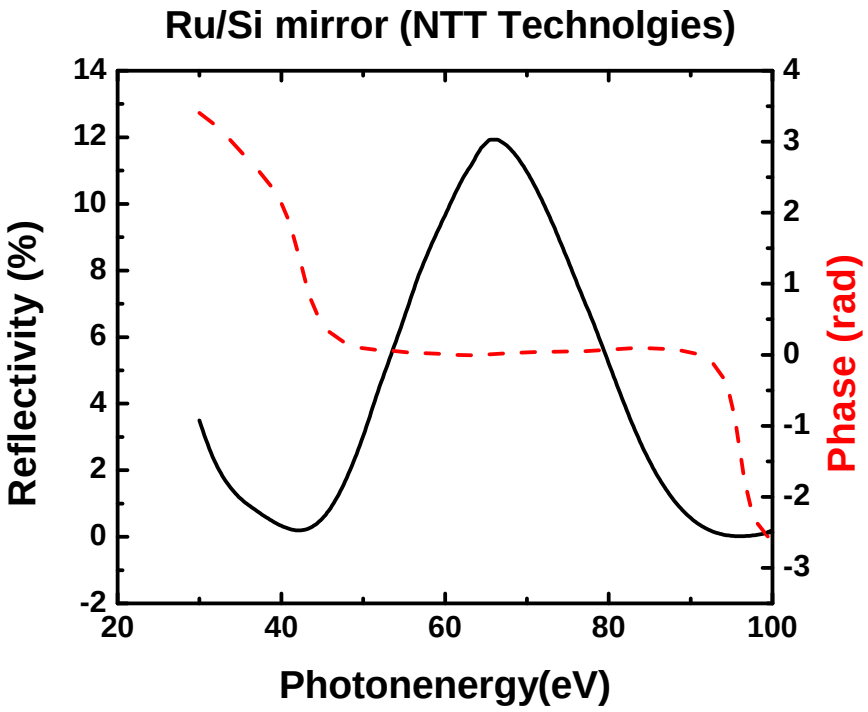

Figure 2.17: Reflectivity (black) and spectral phase (red) of ruthenium/silicon multilayer mirror coated by NTT Advanced Technologies. The reflectivity is centered at 65 eV and the coating has been optimized for broadband reflectivity and to impart minimal spectral phase to the attosecond pulse. The reflectivity and phase measurements are provided by NTT Advanced Technologies.

2.2.6 Photoelectron streaking measurements

Photoelectron streaking is used to measure the attosecond pulse duration [8, 59, 60, 91]. For the measurements the NIR (peak intensity of 5×10^{11} W/cm^2) and attosecond pulse are overlapped in the interaction region of the time-of-flight and the time delay scanned in 136 as (0.02 μm) steps. Time-of-flight spectra at each delay step are integrated for 3×10^4 laser pulses. The attosecond pulse ionizes the target and the nascent photoelectrons experience a shift in momentum that corresponds to the time they were born into the continuum. Photoelectron streaking traces measured with an aluminum filter and neon target gas, as well as a tin filter and argon target gas, are shown in Figures 2.18 and 2.19, respectively. Also shown are the retrieved pulse durations of 145 ± 10 as and 380 ± 10 as. The pulse durations are retrieved using frequency resolved optical gating for complete reconstruction of attosecond bursts (FROGCRAB) [60, 91] technique with the principle components generalized projection algorithm (PCGPA) [100]. The pulse duration of the attosecond pulse transmitted through the tin filter is longer then the pulse transmitted through the aluminum filter, because the tin filter transmits a significantly narrowed spectrum.

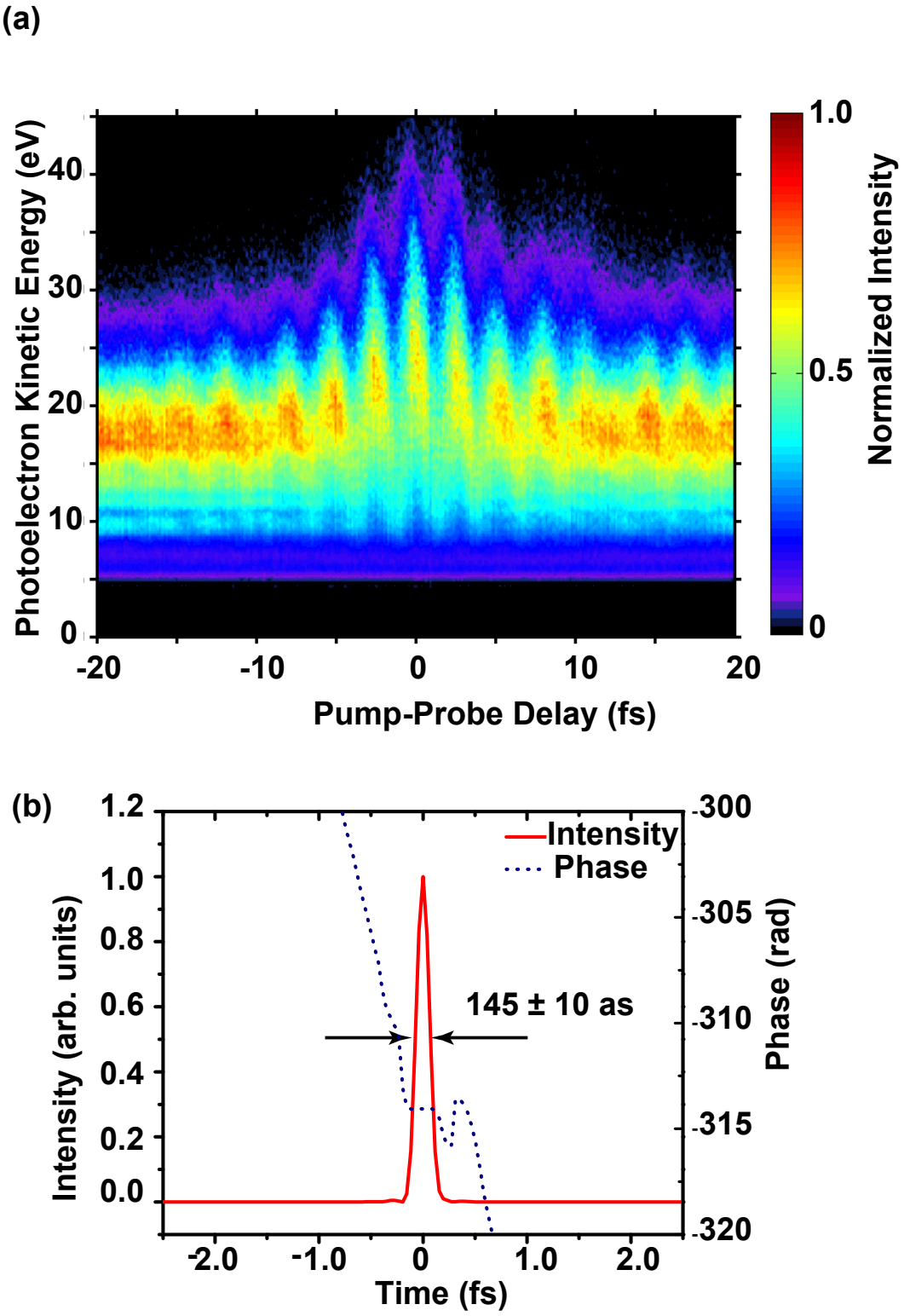

Figure 2.18: Photoelectron streaking spectrogram measured with aluminum filter limiting spectral bandwidth, and neon target gas. FROGCRAB is used to retrieved the pulse duration of 145 ± 10 as.

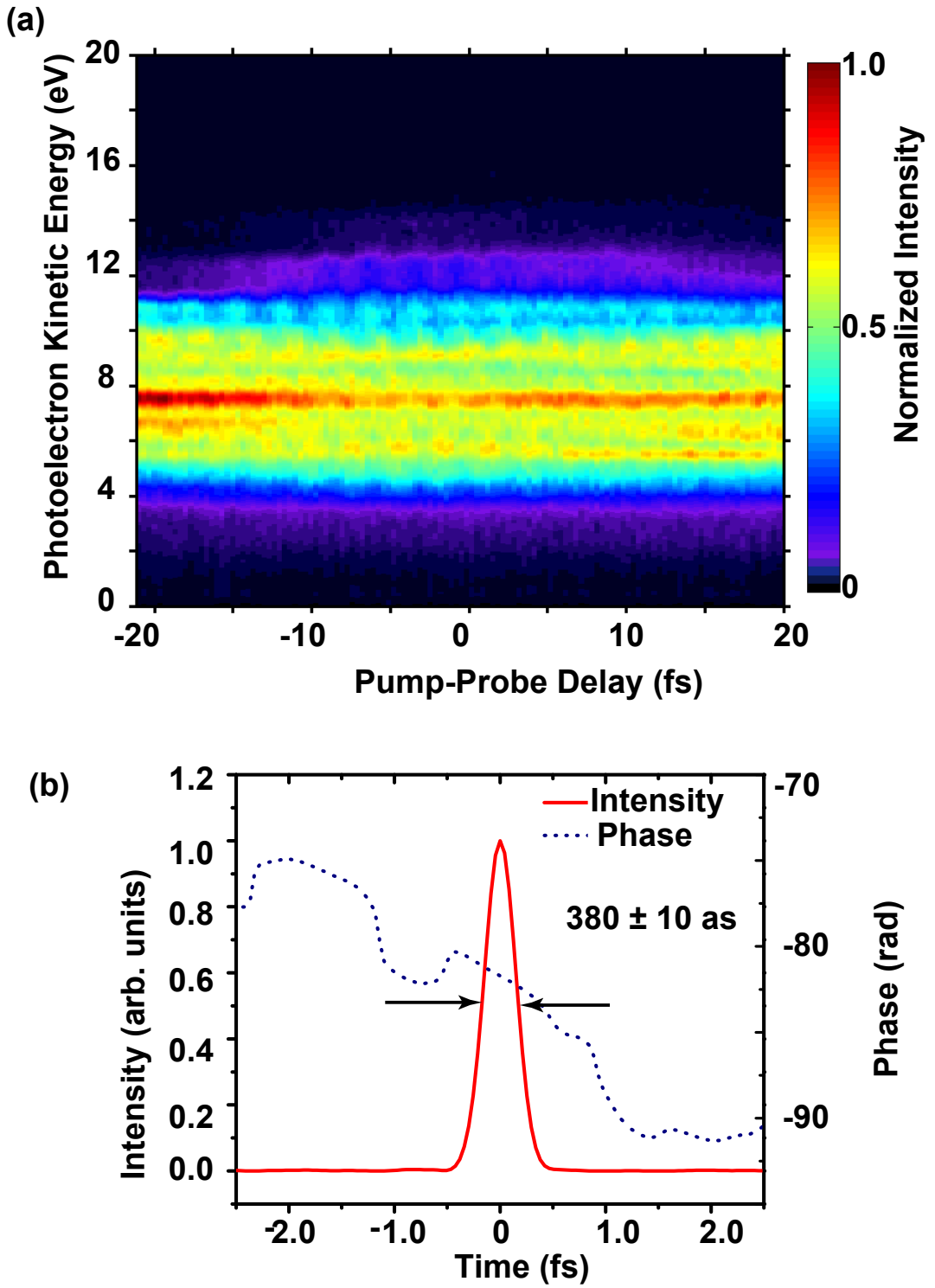

Figure 2.19: Photoelectron streaking spectrogram measured with tin filter limiting spectral bandwidth, and krypton target gas. FROGCRAB is used to retrieve the attosecond pulse duration of 380 ± 10 as.

2.2.7 Absorption spectrometer

A diagram of the home built spectrometer is shown in Figure 2.20. The attosecond

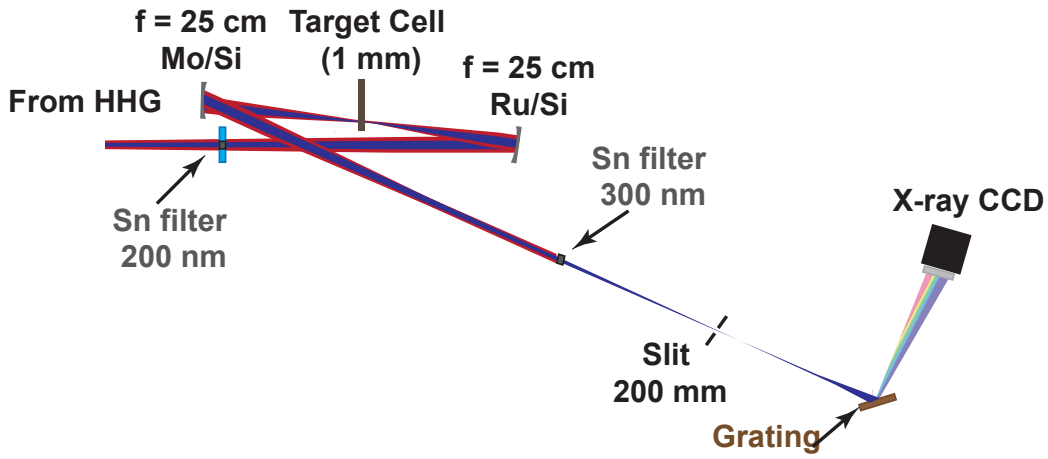

Figure 2.20: Diagram of spectrometer.

pulse is focused by a ruthenium/silicon multilayer mirror into the 1 mm long sample cell, and recollected by a molybdenum/silicon multilayer mirror and directed into the absorption spectrometer (both mirrors are coated by NNT Advanced Technologies). The distance between the mirrors is optimized to produce a focused beam $\sim$ 31 cm in front of the spherical aberration-corrected grating. However, the beam is still significantly astigmatic, with vertical and horizontal foci separated by $\sim$ 1.5 cm. Before the spectrometer a 200 nm tin filter is mounted in a gate valve (VAT), to prevent any scattered NIR light from reaching the X-Ray CCD. A small amount of NIR light is transmitted though the filters, so a 200 μm slit is installed in front of the grating. The slit width is significantly larger than the XUV spot size, so it only serves to reduce the NIR background, because the NIR beam is approximately 20 times larger than the XUV beam. The grating (model 001-0464 from Hitatchi High Technologies) has a groove density of 1200 grooves/mm, blaze angle of 3.2°, blaze wavelength of 60 nm, focal length of 50 cm, and is mounted at the manufacturer's recommended angle of 51°. Incident light (with wavelength λ) is diffracted according to:

$$Gm\lambda = sin(\alpha) + sin(\beta) \tag{2.10}$$

where G is the groove density, m is the diffraction order, α is the incident angle (51°), and β is the diffraction angle [101]. For 20 eV photons the angle β is 51°. The focus in front of the

grating and the X-Ray CCD camera are both located at a distance of 31 cm because the tangential focus (f_t) of the grating is given by [101]:

$$f_t = f_{grating}\ sin(\beta) = 50\text{ cm} \times sin(51^\circ) = 31\text{ cm} \tag{2.11}$$

The efficiency of the grating with a very low blaze angle (less than 5°) is roughly 50% efficiency (as compared to a flat mirror) for wavelengths between $0.67\lambda_b$ and $1.82\lambda_b$, where λ_b is the blaze wavelength (60 nm) [101]. For the grating here the range is 40.2 nm (30.84 eV) to 108 nm (11.48 eV). A flat mirrror mounted at a 51° angle will have an efficiency of approximately 10%, so an estimated 5% of light will be directed to the X-Ray CCD camera (Princeton Instruments Pixis-XO 400B) connected to a computer for data acquisition. The X-Ray CCD is thermoelectrically cooled to −70 °C during experimental acquisition in order to limit electrical noise. As a consequence, pressure in the spectrometer chamber must be below 5×10^{-6} Torr or condensation will form on the CCD chip. An X-Ray CCD camera is used to detect the diffracted light because the camera has an 8 μm pixel size, as compared to an imaging MCP detector coupled to a phosphor screen, where the pixel size is typically 30 μm. Microchannel plates do, however, have the advantage of being less sensitive to NIR background than the X-Ray CCD camera [102]. The X-Ray CCD camera reads out a two dimensional data set, however most data is acquired by integrating over the non-diffracted axis.

Typical spectra are recorded for 3×10^4 or 6×10^4 laser pulses. Figure 2.21 shows a typical transmitted spectrum as a function of pixels, and energy (eV).

The spectra are calibrated using the absorption lines from atomic helium as plotted in Figure 2.22 [103]. The optical density (OD) [71, 72] is calculated as:

$$OD(E) = -Log_{10}[\frac{I_{target}(E)}{I_0(E)}] \tag{2.12}$$

where $I_{target}(E)$ is the spectral intensity at energy (E) measured with 1.6 Torr helium gas and I_0 is the spectral intensity at energy (E) measured without helium target gas. The experimentally measured $OD(E)$ is related to the atomic cross section ($\sigma(E)$) at energy, E, by:

$$OD(E) = -Log_{10}[Exp(-n\sigma(E)L) * \sqrt{\frac{4ln2}{\pi\Delta^2}} \times Exp(-\frac{4ln2\ E^2}{2})] \tag{2.13}$$

where n is the target gas density, Δ is the full width at half maximum of a Gaussian function describing the experimental spectral resolution [72]. The energy calibration is plotted in Figure 2.23. Tin filters, which have a band-pass of $18 - 24$ eV, are used because the second-order diffraction of 40 eV photons will be superimposed on the first-order diffraction of 20 eV photons if the higher energy photons are allowed to pass into the spectrometer. The experimental resolution is 100 meV as measured using the absorption edge of neon at 21.56 eV, as shown in Figure 2.24. The theoretical limit of resolution for the grating is given by the resolving power (R):

$$R = \frac{\lambda}{\Delta\lambda} = \frac{Nd(sin(\alpha) + sin(\beta))}{\lambda} = \frac{W(sin(\alpha) + sin(\beta))}{\lambda} \tag{2.14}$$

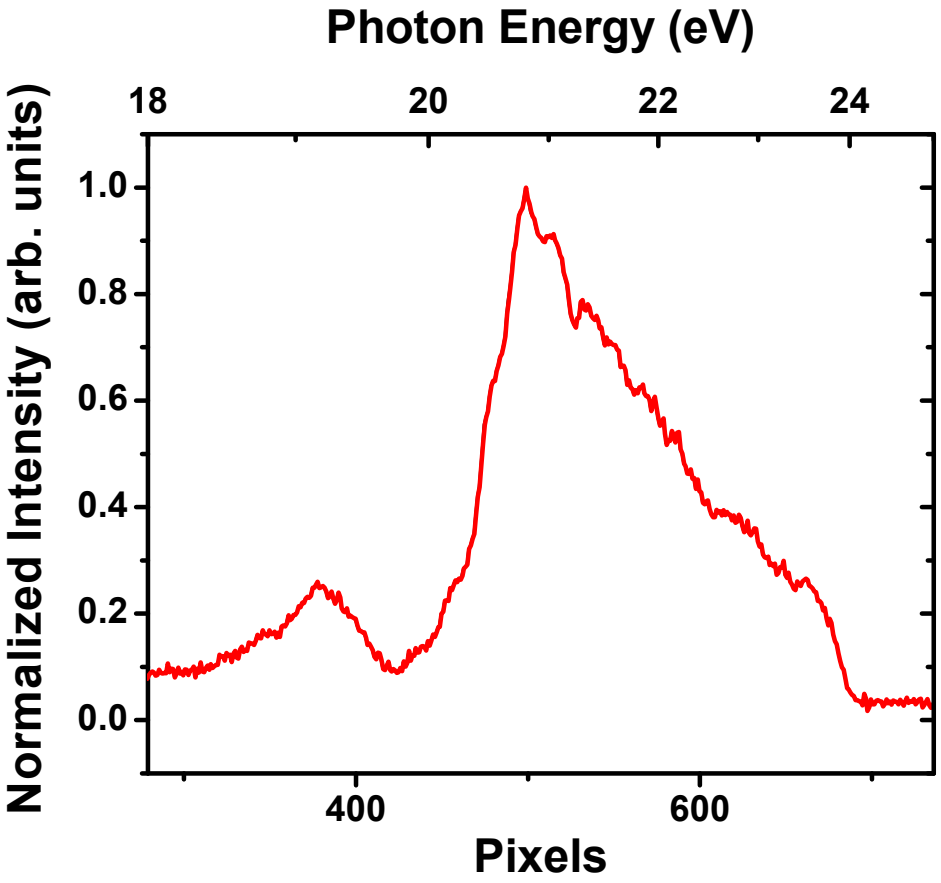

Figure 2.21: Typical spectrum of attosecond pulse, integrated for 6×10^4 laser pulses.

where N is the number of grooves illuminated, d is the groove spacing, and W is the width of grating that is illuminated [101]. Given the experimental geometry (angles β and α of 51°), assuming W as a 0.5 mm diameter XUV spot on the grating, and wavelength of 62 nm or 20 eV, the best resolution achievable at 20 eV is ~ 5 meV. The considerably astigmatic beam directed into the spectrometer is the likely source for the poor resolution.

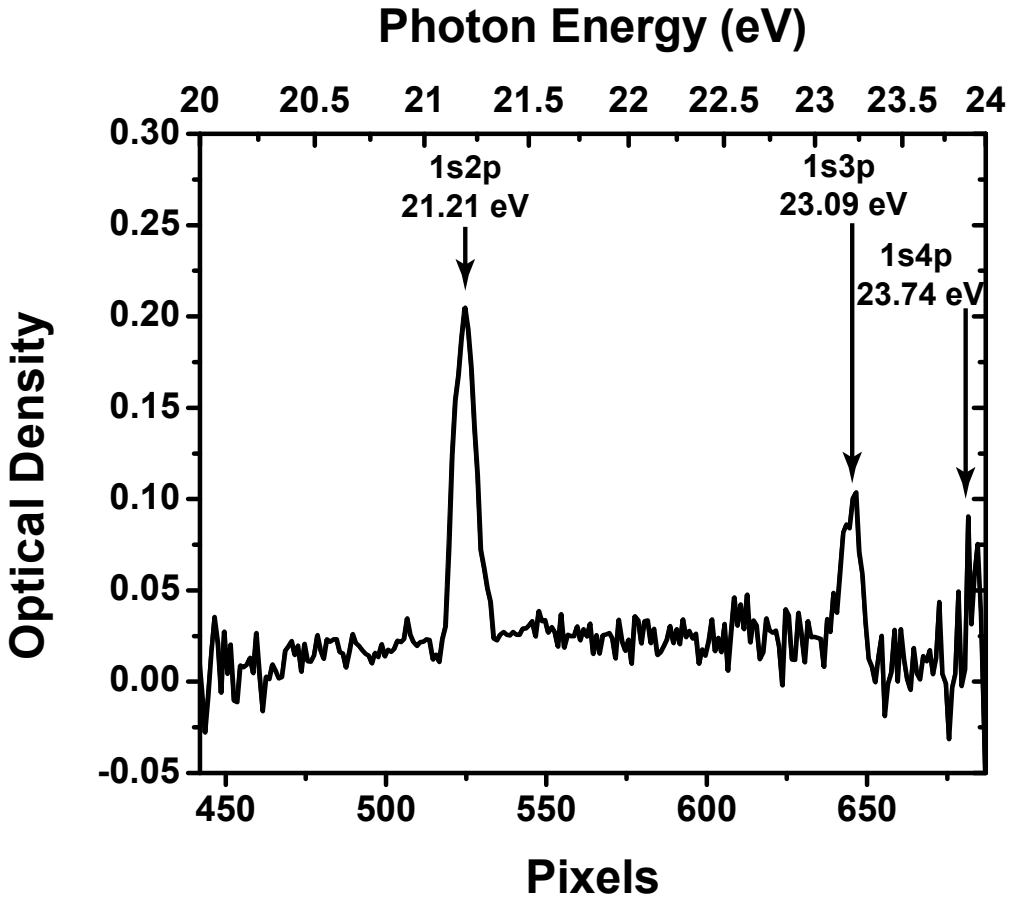

Figure 2.22: Absorption spectrum of helium used to calibrate the spectrum.

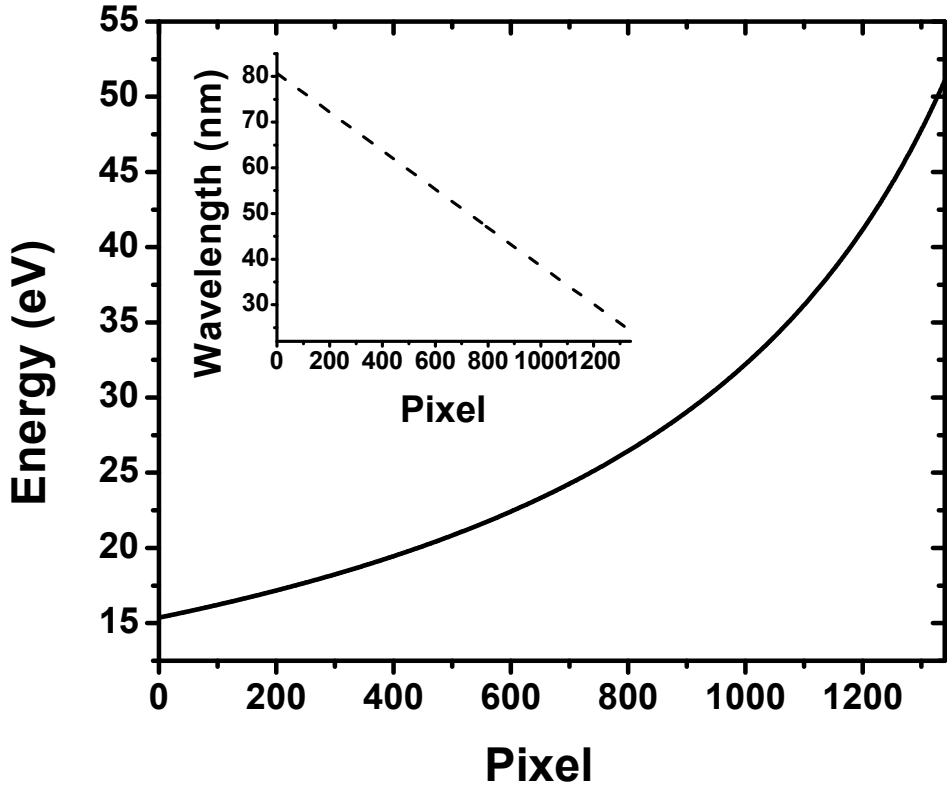

Figure 2.23: Calibration of spectrometer. The photon energy of each CCD pixel and (inset) the wavelength of each pixel.

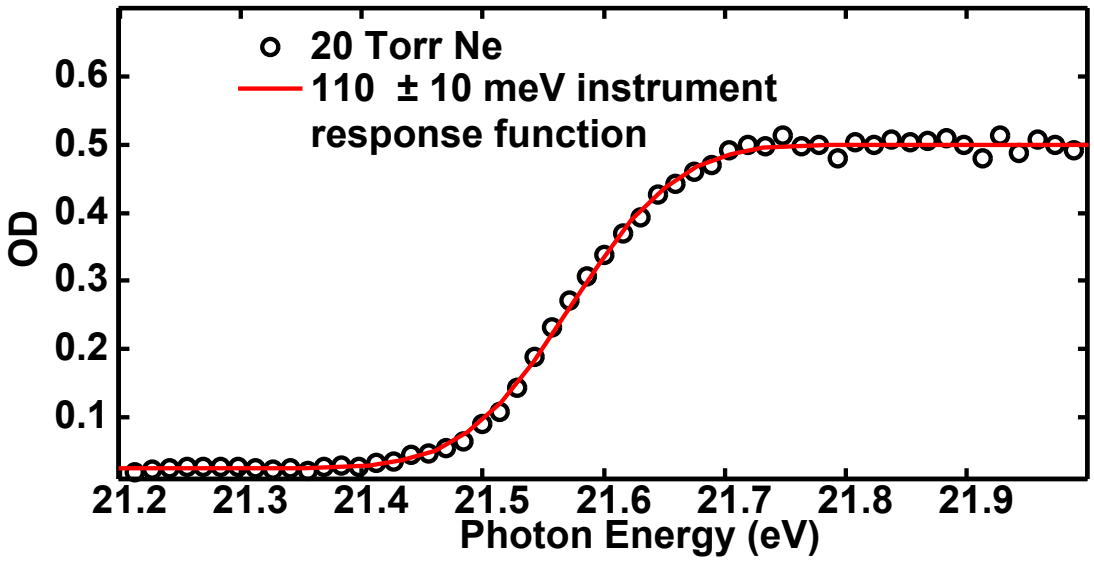

Figure 2.24: Experimental resolution determined from neon absorption edge at 21.56 eV. The absorption spectra of neon gas is recorded in the region of the ionization edge, and fit with an error function, corresponding to a Gaussian with a 110 ± 10 meV full width at half maximum.

Chapter 3

Light-induced states in attosecond transient absorption spectra of laser-dressed helium

Portions of the content and figures of this chapter are reprinted or adapted from S. Chen, M. J. Bell, A. R. Beck, H. Mashiko, M. Wu, A. N. Pfeiffer, M. Gaarde, D. M. Neumark, S. R. Leone, and K. J. Schafer, Phys. Rev. A: At. Mol. Opt. Phys. 86, 063408 (2012). Reproduced by permission of The American Physical Society.

3.1 Dressed absorption

Attosecond transient absorption spectroscopy provides numerous opportunities for the design of experiments that take advantage of the complex interactions between an isolated attosecond pulse (IAP), a strong laser field, and a target medium [3, 4, 76, 104]. Of particular interest are nonlinear processes that combine the IAP and laser fields. Nonlinear coupling schemes, such as those associated with laser-dressed absorption, are powerful tools in many disciplines for creating state-selected populations and aligned molecules [105], modifying optical properties of media (for example, causing transparency [106]), and processing quantum information [107].

Initial computational studies by Gaarde and Schafer et al. [108] investigating the absorption of XUV attosecond pules (with energies between $20 - 24$ eV) by helium atoms bathed in an electric field inspired experimental studies in the Leone and Neumark labs, which were concurrent with continued theoretical studies by Chen, Gaarde, Schafer, and co-workers. Gaarde and Schafer's initial results exhibited additional structures in the XUV absorption spectra in the range of $20 - 24$ eV and motivated further experimental and theoretical work to examine the time evolution of the transient features.

This Chapter presents a joint experimental and theoretical study that focuses on the time-resolved absorption of IAPs by helium atoms at energies between 20 and 24 eV in the

presence of a delayed near-infrared (NIR) pulse. The experimental measurements of dressed absorption were performed at the University of California, Berkeley and Lawrence Berkeley National Lab, while the theoretical calculations were performed in the research group of Gaarde and Schafer at Louisiana State University. The theoretical methods and calculations are included here so that experimental measurements may be fully understood.

When the IAP and NIR pulses overlap, several new features in the transient absorption spectra below the single ionization threshold are observed which are not associated with any dipole-allowed extreme ultraviolet (XUV)–driven transition. Theoretical investigation reveals that each of these light-induced structures (LISs) involves the transfer of population from the ground $1s^2$ state to $1sns$ or $1snd$ states via resonant second-order processes requiring both the XUV and the NIR fields. In our experiment, the broad bandwidth of the IAP allows the simultaneous observation of all the LISs for each delay where the two fields are overlapped. As the NIR intensity or the NIR-IAP delay is changed, the light-induced states are observed to shift in energy and absorption strength, in agreement with the calculations.

Most previous absorption studies on laser-dressed He have been carried out with attosecond pulse trains (APTs). Modification of the ionization probabilities [109, 110] and the absorption [111, 112] as a function of NIR-APT delay has been observed for APTs overlapped in time with NIR fields. Additional work with APTs has considered the sensitive dependence of the ionization probability on the XUV wavelength chosen to resonantly excite specific $1snp$ states of He [113, 114]. Recent work on transient IAP absorption in He focused on the sub-cycle changes in the linear XUV absorption around the $1s3p$ and $1s4p$ dipole allowed states [115]. This is in contrast to the work reported here, where multiple, resonant second-order transitions are observed and theoretically understood across the large bandwidth of the IAP.

3.2 Experimental and theoretical methods

The experimental setup is shown in Figure 3.1. The IAPs are generated in krypton gas via double optical gating and spectrally limited to $20 - 24$ eV by a 200 nm thick Sn filter [54, 88]. They are then are overlapped with a 12 fs, 780 nm NIR pulse in the absorption cell of an attosecond transient absorption spectrometer with a variable time delay between the pulses. In the absorption spectrometer, the NIR and IAP pulses are collinearly focused by a Ru/Si multilayer mirror (f = 25 cm) in a 1 mm long target gas cell, filled with 20 Pa He. Transmitted XUV light is recollected by a Mo/Si multilayer mirror (f = 25 cm) and directed through an additional 200 nm Sn filter and onto the entrance slit of the XUV spectrometer. A gold-coated, aberration-corrected grating spectrally disperses the IAP onto an X-Ray charge-coupled device (CCD) camera, where the transmitted spectrum is recorded. The XUV spectrometer resolution is 100 meV, as determined from measurement of $1s2p$ and $1s3p$ He absorption lines.

The 400-as IAPs are characterized by photoelectron streaking [60, 116], while the NIR pulse is measured by the spectral phase interferometry for direct electric field reconstruction (SPIDER) method [87]. For streaking, Kr gas is ionized by the IAP and overlapped with the

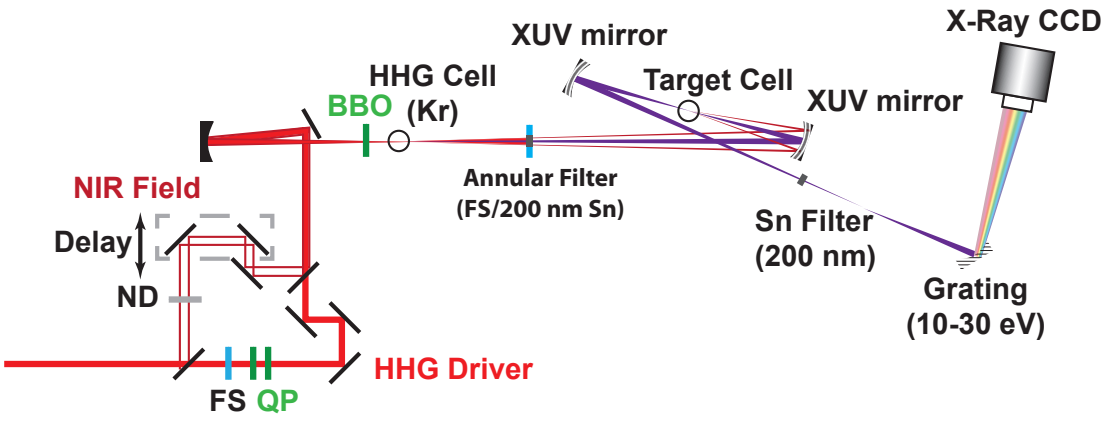

Figure 3.1: Experimental setup. Schematic of attosecond transient absorption instrument. ND, neutral density filters; FS, fused silica; and QP, quartz plates. Optics for double optical gating are shown in green. IR beam paths are shown in red. IAP is shown in purple.

NIR pulse, and a Ru-Si multilayer mirror is used to combine the two pulses. The principal component generalized projections algorithm [60, 63] issued to reconstruct the pulses and, upon convergence, the extracted duration is 380 ± 10 as. The XUV pulses are not transform-limited—the spectral phase of the attosecond pulse varies by approximately one radian across the pulse.

Transient absorption spectra are recorded as the average of five pump-probe scans, each of which is acquired for 30,000 laser pulses at every pump-probe time delay point. Absolute optical density (OD) spectra are constructed as:

$$OD = -Log[\frac{I_{sample}(E)}{I_0(E)}] \tag{3.1}$$

where $I_{sample}(E)$ is the measured spectral intensity of the IAP after it passes through the 1 mm long sample cell filled with 20 Pa He, and $I_0(E)$ is the spectral intensity of the IAP after it passes through the empty sample cell. To obtain a broad overview of the onset and evolution of the LISs, time delay scans over tens of femtoseconds are required. To that end, delay steps of 1.3 fs (one-half NIR cycle) were used in the experiment.

The theoretical treatment of laser-dressed absorption is based on the semi-classical picture of a quantum atom driven by a classical field [108, 117]. Chen, Gaarde, and Schafer calculate the single-atom frequency-dependent response function:

$$\widetilde{S}(\omega) = 2Im[\tilde{d}(\omega)\widetilde{E}^*(\omega)] \tag{3.2}$$

where $\tilde{d}(\omega)$ is the Fourier transform of the dipole moment $d(t)$, obtained by solving the time-dependent Schrödinger equation (TDSE) using the full IAP + NIR electric field $E(t)$ in the single-active-electron approximation. Details of the method are given in Ref. [108].

Calculating the response non-perturbatively is advantageous because the atom exchanges energy with the light field over a large range of frequencies in many different orders of nonlinearity. The calculations treat all of these processes on an equal footing. For positive frequencies, $\widetilde{S}(\omega)$ is the energy gained or lost per unit frequency by the atom, meaning that positive or negative values of $\widetilde{S}(\omega)$ represent absorption or emission at frequency ω. In this work, we concentrate on absorption, which dominates the response.

The calculation of the energy exchange between the atom and the field requires a timescale for the decay of the dipole initiated by the driving fields. In an experiment, dephasing (collisional broadening, for example), spontaneous decay, and finite spectrometer resolution all serve to define effective timescales for the dipole decay. In the calculations, these processes are absent and a numerical dephasing time is provided instead, by multiplying a smooth window function onto the calculated time-dependent dipole moment before Fourier transforming it to obtain the response function. In the work presented here we are primarily interested in the modification of the absorption by the NIR field, and using a dephasing time that is much longer than the NIR pulse duration is, therefore, sufficient. The 65 fs dephasing time used in this work gives a minimum spectral bandwidth of 20 meV. Doubling the dephasing time in the calculations does not change any of the conclusions presented below.

A full theoretical treatment of transient absorption requires solving the Maxwell wave equation (MWE) for the time propagation of the light fields through the atomic medium. This is done using polarization and ionization source terms in the MWE that are obtained by solving the single-atom TDSE [108]. Coupling the MWE and TDSE solvers in this fashion requires much more numerical effort than the calculation of the single-atom response alone. A calculation of the full propagated light fields for XUV and NIR pulses that are overlapped with zero time delay and a pressure of 400 Pa shows that even though there is strong absorption, the time structure of the IAP is remarkably robust and does not undergo reshaping, only a small time shift of a few attoseconds. Repeating this calculation for several XUV-NIR time delays near zero shows that the macroscopic absorption spectra obtained from the full propagated light fields are similar in all their features to the single-atom results, scaled by the density. This means that it is sufficient to calculate the single-atom response in order to understand the experimental results.

3.2.1 Results

Figure 3.2 shows experimental measurements (left panels) of the transient absorption of atomic He and compares them to theoretical calculations (right panels) of the frequency-dependent response function, both versus the NIR-IAP delay. Measurements were made using two NIR intensities estimated from *in situ* streaking shifts to be 1.6×10^{12} W/cm^2 and 4.8×10^{11} W/cm^2 (Figures 3.2(a & c), respectively). The intensity of the NIR field is controlled by a neutral density filter. Using the intensity profile of the NIR focus (measured with a CCD) and XUV focal spot size (calculated as twice the beam waist with standard Gaussian optical techniques) the NIR intensity is estimated to vary by 20% across the XUV focal spot. The theoretical calculations were made for the same peak intensities using 12 fs

transform-limited pulses with a central wavelength of 780 nm (Figures 3.2(b & d)). The delay step in the calculations is 0.16 fs. The overall agreement between experiment and theory is very good. Many of the features presenting only near zero delay are in notable accord, and features visible over the whole range of time delays are also reproduced.

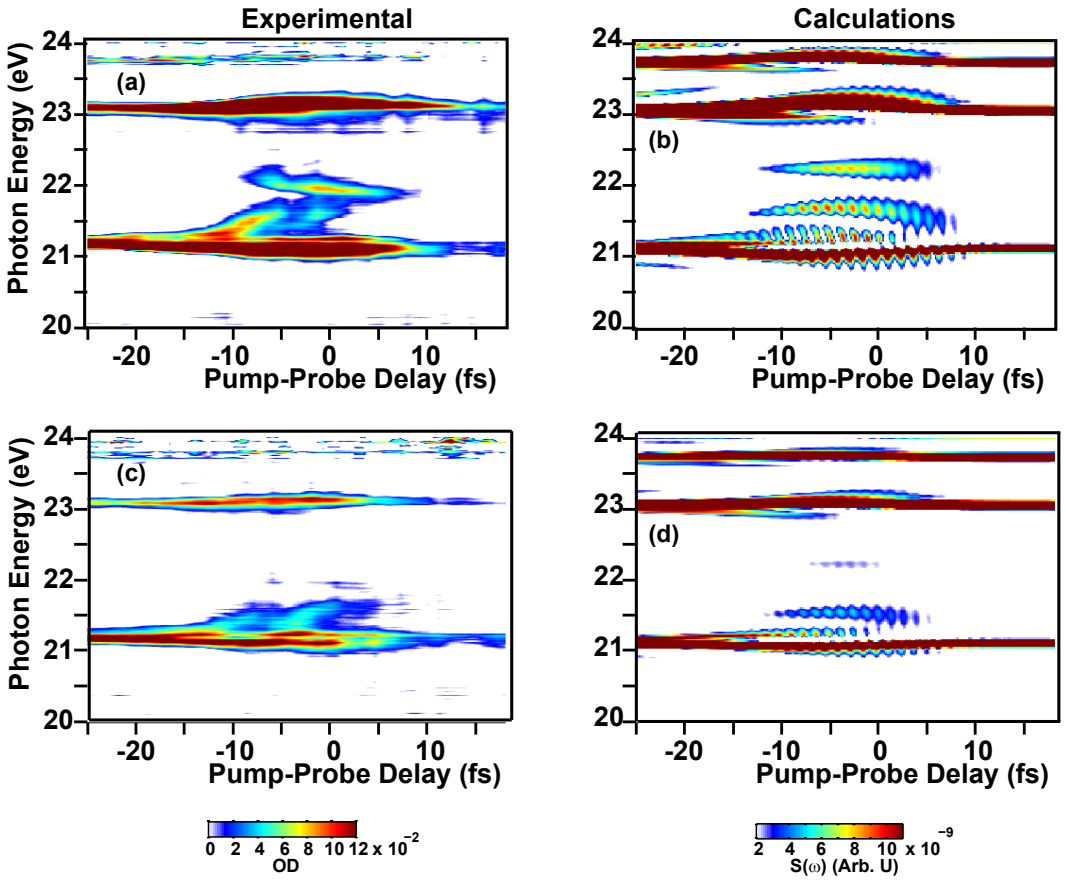

Figure 3.2: Comparison of experimental (right hand side) and calculated (left hand side) absorption spectra of helium atoms dressed by a 780 nm field. The top figures correspond to measurements with peak NIR intensity of 1.6×10^{12} W/cm^2 and the lower row corresponds to 4.8×10^{11} W/cm^2. The theoretical plots use a small, nonzero value of the minimum response to better mimic the experiment. The $1s2p$ resonance is at 21.21 eV and the $1s3p$ resonance is at 23.09 eV.

In Figure 3.2, delay times of $t_d > 10$ fs correspond to the NIR pulse arriving well before the IAP. Here, the absorption spectra comprise only resonant features due to excitation of the $1snp$ states by first-order XUV processes, identical to the case when no NIR is present. The NIR field is not strong enough to excite the atom out of its ground state. Because the instrumental resolution in the experiment is much larger than the Doppler broadened

linewidth, the measured absorption resonances are observed as peaks of the same area spread over a larger spectral range. This implies that absorption of the XUV photons on resonance is much higher than expected from measured optical densities. In contrast, the absorption spectra are strongly modified when the XUV and NIR pulses overlap (-15 fs $< t_d <$ 10 fs). Most striking is the enhanced absorption at frequencies that cannot be assigned to any linear XUV absorption process that reaches a field-free atomic state. Some of these LISs appear at energies between 21.25 and 22.5 eV in Figure 3.2, energies that are distinct from the XUV-driven dipole allowed transitions to the $1s2p$ and $1s3p$ states.

For delays of $t_d < -15$ fs the calculations show several delay-dependent sidebands around the $1s2p$ absorption feature. These sidebands are due to perturbed free polarization decay [118], caused by the modulation of the $1s^2 - 1s2p$ coherence by the NIR pulse, which arrives after the XUV has excited the system. The delay-dependent sidebands are spaced as the reciprocal of the pump-probe delay, which is quite a bit smaller than the experimental resolution for large delay times. Although the sidebands are not observed in the experimental absorption spectra, the absorption strength appears to broaden and increase in this region; the broadening is real, but the absorption increase could be due to detector saturation on line center. Because of the finite spectrometer resolution, the limited number of XUV photons, and the strong and narrow lines of the He, the line centers can appear as if there is total absorption on some CCD camera pixels, with concurrent broadening of the features to adjacent pixels due to the wings of the lines. These complications can make precise comparison of the absolute intensities with theory difficult.

3.2.2 Asymmetry

The experimental absorption spectra are asymmetric with respect to pump-probe delay (i.e. the absorption is greater for negative pump-probe delays). At negative pump-probe delays the attosecond pulse arrives at the target before the NIR pulse. In this case the attosecond pulse induces a polarization in the helium target that is subsequently perturbed by the NIR pulse. As a result the absorption features have additional structure. The structure is analogous to perturbed free induction decay observed in the femtosecond absorption measurements [118]. The additional structure appears as increased absorption due to the combined effects of the limited spectral resolution and spectral flux.

This effect is illustrated in Figures 3.3 and 3.4. Where the transmission of a 1 mm long cell filled with 1×10^{-1} Torr He, has been calculated using the Doppler linewidth of the $1s2p$ transition at room temperature (~ 0.1 meV) and a literature value of oscillator strength [119]. The transmission is thresholded at 10^{-5} (to simulate the effect of absorption saturation), and shown for two cases: infinitely fine resolution (black) and 100 meV resolution (red, found by convolving the transmitted spectrum with a Gaussian that has a full width at half maximum equal to 100 meV). The optical density is plotted below the transmission. In Figure 3.4, the linewidth is assumed to be broadened to twice the Doppler linewidth. The transmitted spectra and the optical density are calculated as in Figure 3.3 for both the cases of infinitely fine resolution and 100 meV resolution. Comparing the bottom right of Figure 3.3 to the

bottom right of Figure 3.4, the resolution limited optical density assuming a larger linewidth is higher than the narrower linewidth.

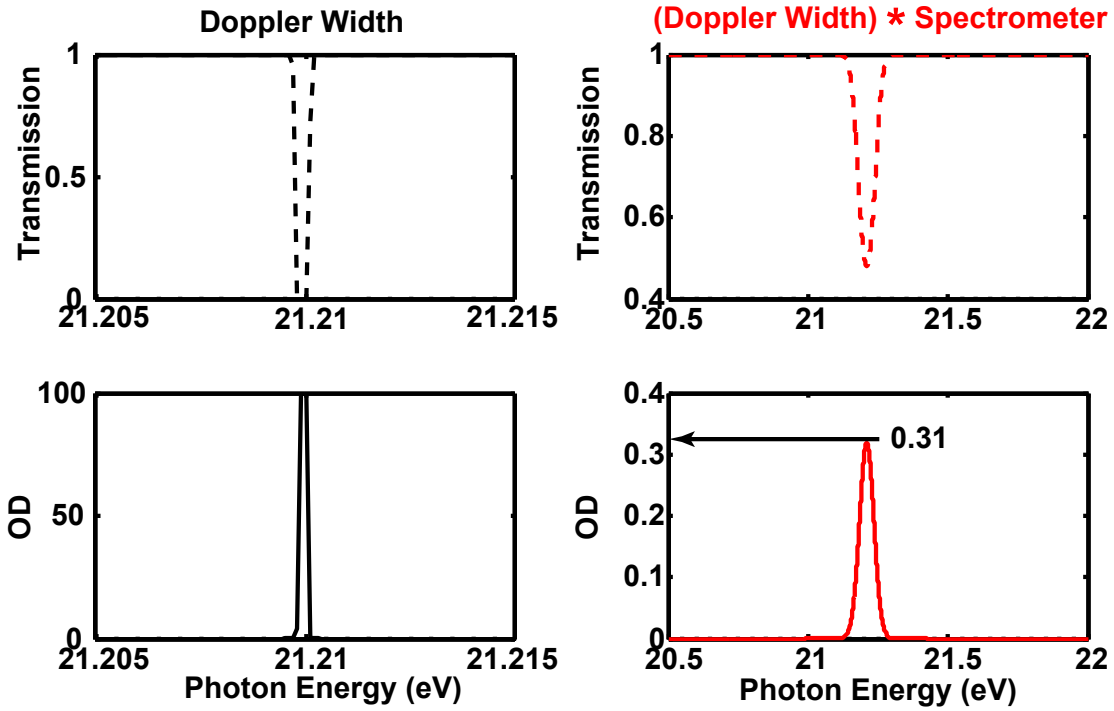

Figure 3.3: The transmission (top left) and optical density (bottom left) of a 1 mm long cell filled with 1×10^{-1} Torr He, assuming infinitely fine resolution and a Doppler broadened linewidth. The Doppler broadened peak appears wider than ~ 0.1 meV due to saturation effects. The transmission (top right) and optical density (bottom right) assuming 100 meV resolution and a Doppler broadened linewidth.

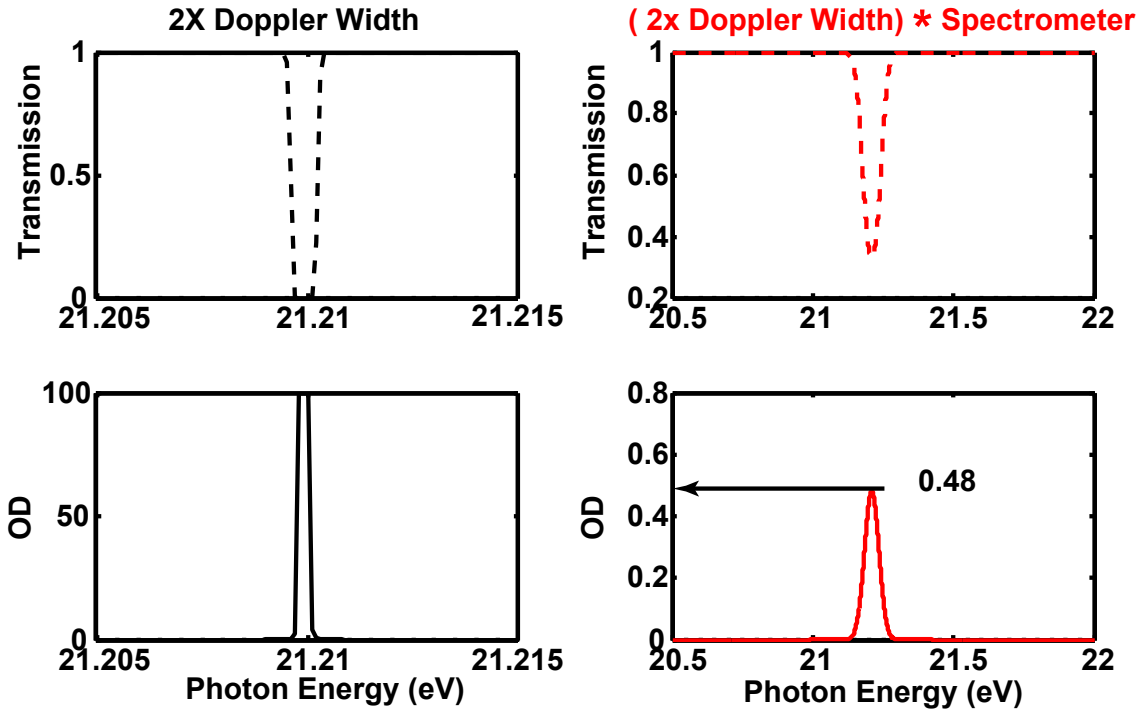

Figure 3.4: The transmission (top left) and optical density (bottom left) of a 1 mm long cell filled with 1×10^{-1} Torr He, assuming infinitely fine resolution and a linewidth equal to twice the Doppler linewidth. The transmission (top right) and optical density (bottom right) assuming 100 meV resolution and a Doppler broadened linewidth.

3.3 Interpretation

Figure 3.5 provides an intuitive interpretation of the light-induced structures near zero delay in the transient absorption spectra. Line spectra for both NIR intensities, measured at one pump-probe delay (-2.7 fs), are plotted in Figure 3.5(a), with dashed lines indicating peak positions occurring in the 1.6×10^{12} W/cm^2 intensity spectrum. The position of the LISs suggests the interpretation diagrammed in Figure 3.5(b), where we assume that the strongest modification to the XUV absorption spectrum will be due to first-order NIR processes. Resonant processes are possible if the combination of XUV and NIR fields can couple the ground $1s^2$ state to $1sns$ or $1snd$ states. The LISs in the absorption spectrum are then interpreted—in the frequency domain—as the intermediate states of processes that involve the absorption or emission of an additional NIR photon. For example, the absorption feature at 22 eV near zero delay indicates an intermediate state that couples the ground state to the $1s2s$ state. This "$1s2s$" LIS is located at approximately:

$$\omega_{LIS} \approx \omega_{1s2s} - \omega_{1s^2} + \omega_{NIR} \tag{3.3}$$

Similarly, LISs correlated to the $1s3d$ and $1s3s$ states are located approximately one NIR

photon below these states at 21.6 and 21.25 eV, respectively. These experiments can thus be thought of in analogy to stimulated Raman spectroscopy studies of atoms [120], but with broadband NIR and XUV pulses. Typical stimulated Raman transitions are two-photon processes where the difference between frequencies of Raman pump and probe pulses is chosen to be resonant with a transition in the target media [121]. In the present case this resonance condition is automatically satisfied in a relatively narrow band of XUV frequencies, picked out of the broadband IAP continuum.

The case for this absorption mechanism can be strengthened by examining the calculations presented in Figure 3.2 in more detail. A simple check is provided by repeating the calculations in Figure 3.2 while using a TDSE time propagation routine that dynamically eliminates the $1s2s$, $1s3d$, and $1s3s$ states by projecting them out at each time step. As shown in Figure 3.6(a), this eliminates the LIS features and causes the $1s2p$ absorption line to become an unshifted, delay-independent feature, in contrast to the full result in Figures 3.2(b) and 3.2(d). This shows that the splitting and shifting of the $1s2p$ state are dominated by NIR-induced couplings to the nearby ns and nd states. In addition, if the LISs are related to processes that couple the ground state to dipole forbidden states, then the strength of the LISs should be related to the population in those states at the end of the laser pulse. As an example, Figure 3.6(b) compares the final population in the $1s2s$ state to the calculated integrated absorption around 22.2 eV (the $1s2s$ LIS). This comparison is straightforward because $\widetilde{S}(\omega)$ is a probability per unit frequency, which means that the integrated response in a range of frequencies $\Delta\omega$ around the LIS can be directly compared to the population in a given bound state at the end of the pulse. The calculations show that when (and only when) the $1s2s$ LIS is observed, population is efficiently transferred to the $1s2s$ state after the pulses have passed. Likewise, the delay-dependent final population in the $1s3d$ and $1s3s$ states follow the strengths of the $1s3d$ and $1s3s$ LISs. Taken together, these results support the explanation of the LISs outlined in Figure 3.5(b).

The second-order process that gives rise to the $1s2s$ LIS is the simplest example of the proposed absorption mechanism. The transfer of population from the $1s^2$ ground state to the $1s2s$ state is enabled by the presence of the nearby $1s2p$ state, which has a strong dipole coupling to both states. Solving the TDSE using just these three states is thus helpful for interpreting the absorption data shown in Figure 3.2, using the same laser parameters as the full calculation: A peak Rabi frequency of 170 THz (0.7 eV) and a detuning, $\Delta_{1s2s} = \omega_{NIR} - \omega_{1s2s-1s2p}$, of 1 eV. Figure 3.6(c) shows that the three-level model (TLM) reproduces the LIS around 22 eV quite well.

Figures 3.2 and 3.6 show that both the full calculations and the TLM calculations predict sub-cycle oscillations in the absorption features when the two pulses are overlapped in time. The modulations happen at twice the laser period and can be seen in both the absorption strengths and the final populations for the $1snp$, $1sns$, and $1snd$ states. These sub-cycle oscillations are not washed out even though the absorption probability is a time-integrated measure. Using the language of a TLM, one can interpret these oscillations as driven by the counter-rotating terms in the coupling between the $1snp$ and the $1sns$ or $1snd$ states (they are absent in a TLM employing the rotating wave approximation [122]). These counter-rotating

terms can be prominent when the NIR Rabi frequency is comparable to the photon energy as in this case [123]. In a true three-level system one would expect these oscillations to be $\pi/2$ out of phase with the driving field because of the large detuning. Indeed, in Figures 3.6(c) and 3.6(d) both the $1s2s$ LIS absorption and the $1s2s$ final population peak a quarter cycle after the NIR electric field. In the full calculation, Figure 3.6(b), the timing is complicated by the $1s2p$ state interacting with multiple $1sns$ and $1snd$ states, and the LIS absorption does not necessarily peak at the same time as the s and d final-state populations. A full description of these sub-cycle features is beyond the scope of this chapter, but the presence of the sub-cycle features suggests a rich area for future experimental and theoretical study.

Returning to the experimental data in Figures 3.2(a), 3.2(c), and 3.5(a), as the NIR intensity is increased, the strength of absorption of the $1s2s$ LIS near 22 eV increases significantly, whereas those of the $1s3d$ and $1s3s$ LISs decrease slightly. This is observed in the calculations in Figures 3.2(b) and 3.2(d) as well. Both the experimental and theoretical results in Figure 3.2 also show that the central energy of the LISs can change with NIR delay. The calculations suggest that this is due to the change in NIR intensity with delay. This intensity dependence is studied further in Figure 3.5(c) which shows calculations of the central energies of the $1s2s$, $1s3d$, and $1s3s$ LISs as a function of NIR intensity, at a delay of -2.7 fs (solid lines). The experimental intensities are limited to the lower energy portion of the intensity range studied in Figure 3.2(c). To better understand the changes in the LIS absorption energy and strength, the full calculations in Figure 3.2(c) are compared to TLM calculations constructed separately for each LIS as was done for the $1s2s$ LIS above. These show that the changes are qualitatively explained by the degree of field detuning involved in each LIS. For example, the $1s2s$ LIS, which has the largest detuning (1 eV) from the NIR laser wavelength, is barely visible in low-intensity data, consistent with a resonant absorption picture where transition strength decreases as detuning increases. The large detuning of the $1s2s$ LIS also explains why the NIR intensity has little effect on its energy. On the other hand, the central energies of the $1s3d$ and $1s3s$ LISs have a much larger dependence on the NIR intensity due to the smaller detunings involved. Note, however, that the intensity dependence of the $1s3d$ and $1s3s$ LISs in the full calculation is much bigger than that predicted by the TLM. The TLMs of these LISs break down because the $1s3d$ and $1s3s$ states are resonantly coupled by the NIR field to states near threshold, and these additional couplings cannot be ignored when calculating the position of the LISs. This sensitivity to the NIR intensity can be exploited to make accurate measurements of the LIS properties, to control non-dipole coupled-state populations, and to better understand the behavior of these states in a strong NIR field.

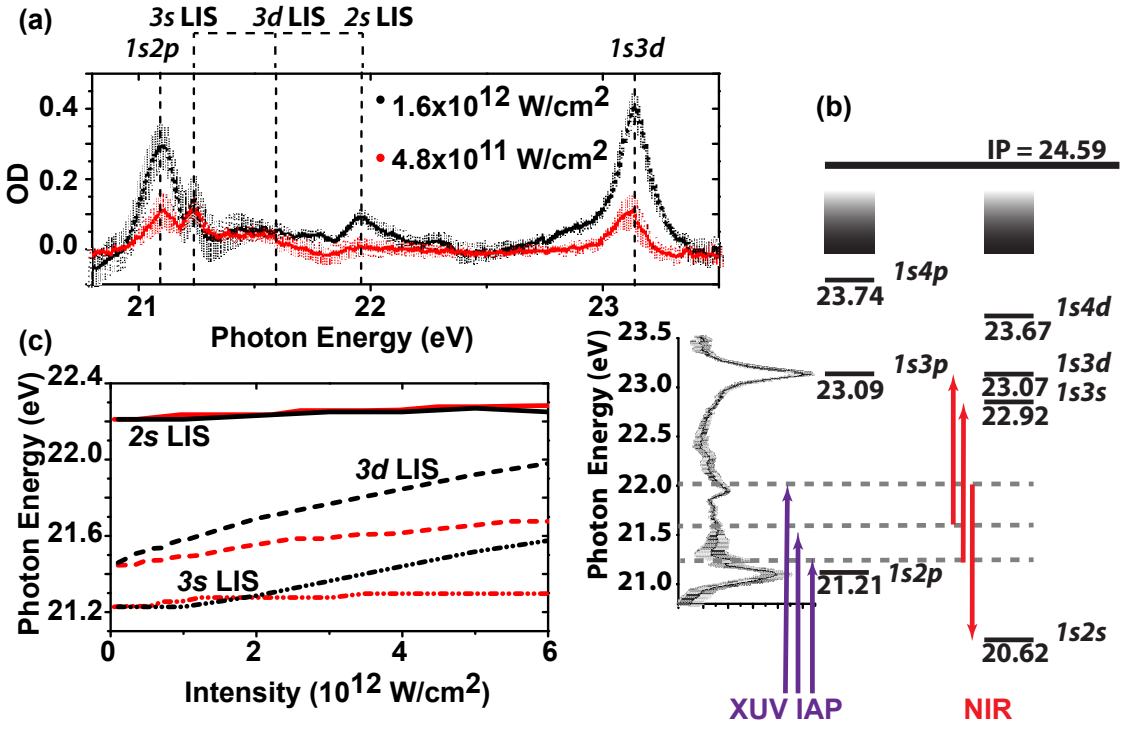

Figure 3.5: (a) Line spectra at a pump-probe delay of -2.7 fs for intensities 1.6×10^{12} W/cm^2 (black) and 4.8×10^{11} W/cm^2 (red). Error bars represent $\pm\,\sigma$. (b) Schematic energy level diagram for excitation of light-induced states. Line absorption spectrum measured with overlapped NIR and IAP pulses is shown in black. Peaks in the absorption spectrum around 22, 21.6, and 21.25 eV clearly do not result from excitation to dipole-allowed $1snp$ levels. LISs couple the ground state to $1sns$ and $1snd$ states via absorption of one XUV photon (purple) and absorption or emission of one NIR photon (red). (c) Calculated positions of $1s2s$, $1s3d$, and $1s3s$ LISs vs NIR intensity for a delay of -2.7 fs. Full calculations (solid black lines) are compared to three-level model calculations (dashed red lines).

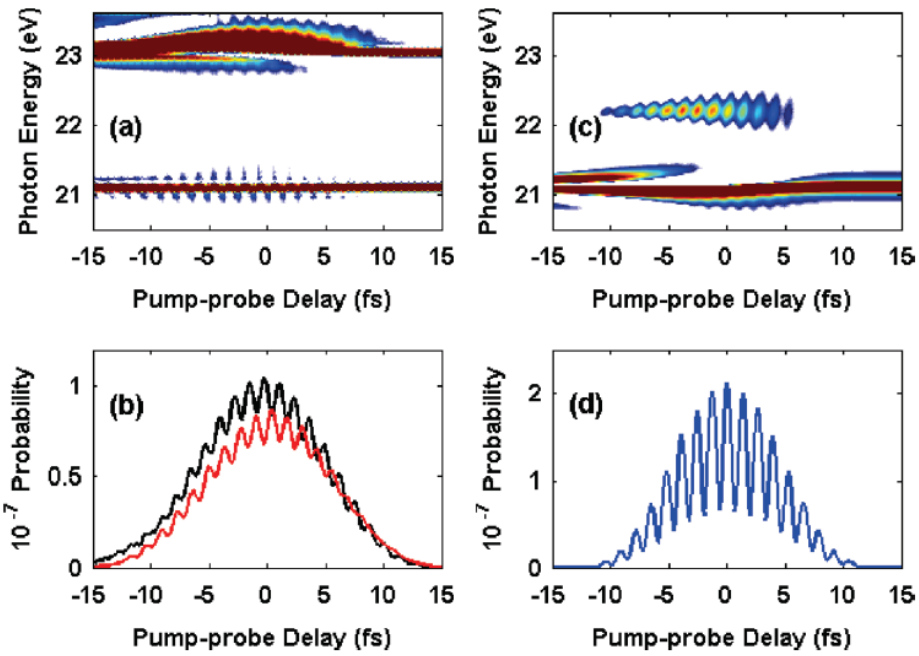

Figure 3.6: (a) Same as Figure 3.2(b) but with the $1s2s$, $1s3s$, and $1s3d$ states all subtracted out during the time propagation. (b) Calculated integrated absorption probability around the 22.2-eV LIS in Figure 3.2(b) (black) and the final $1s2s$ population (red) vs the pump-probe delay. (c) Three-level model of the response function $\tilde{S}(\omega)$ near the $1s2s$ LIS with the $1s^2$, $1s2p$, and the $1s2s$ states included. The XUV and NIR pulses are the same as in the full calculations in Figure 3.2(b). (d) The $1s2s$ population at the end of the pulses in the three level model of part (c). Note that the units in panels (b) and (d) are the same, without any modification of the original data.

3.4 Conclusions

In summary, modifications of He atomic absorption spectra are observed in measurements using IAPs in an attosecond transient absorption instrument. The dressed absorption features include LISs, which can be interpreted in terms of second-order resonant transitions to non-dipole coupled atomic states. These absorption features can be thought of in analogy to stimulated Raman spectroscopy studies of atoms [120], and they are observed here in the domain of attosecond spectroscopy. The use of broadband, coherent XUV radiation allows the observation of LISs without specifically tuning to a two-photon transition as would be required with narrowband XUV light. Because the resonance condition is automatically satisfied regardless of the precise NIR frequency, this stimulated absorption technique can be used to study the strong field coupling of excited states in systems more complicated than the simple atomic system used in this study. Both experiment and theory indicate that the properties of the observed LISs can be controlled by varying the NIR intensity and/or the NIR-IAP delay.

Chapter 4

Intensity dependence of light-induced states observed in laser dressed absorption of helium near the $1s2s$ state

Transient absorption spectroscopy, the technique of recording a transmitted spectrum of a laser pulse (probe pulse) as a function of delay time between the probe pulse and a second pulse (pump pulse), has been successful in measuring multi-femtosecond molecular dynamics for over two decades [75]. This technique is well suited to attosecond spectroscopy because isolated attosecond pulses necessarily have large bandwidths that allow spectral features over a broad range to be monitored. As examples, electronic coherence [4], modification of optical properties of insulating materials [73], and lifetimes of autoionizing states [3] can be measured with attosecond transient absorption spectroscopy.

Owing to the limited number of photons in isolated attosecond pulses, typical attosecond pump-probe measurements incorporate a strong near-infrared (NIR) pulse (intensities of 10^{12} W/cm^2 or higher) together with the attosecond pulse. The NIR laser pulse can induce dynamics [4] or probe reaction products [29] (via field or multiphoton ionization), when overlapped in time with the XUV attosecond pulse. An active area of research focuses on elucidating the extent that the strong NIR field may be affecting measured dynamics. For example, studies have focused on the necessary conditions for extracting field-free parameters from experimental measurements. The strong NIR field can couple atomic and molecular excited states resulting in a modified ("laser-dressed") absorption spectrum. Autler-Townes splittings, electromagnetically induced transparency [124, 125], and light-induced states [126] have been measured with atoms in strong optical fields by femtosecond and attosecond XUV pulses.

This chapter focuses on light-induced states (LISs) [126], transient absorption features that occur when the attosecond and NIR pulses are overlapped in time and are not related to the field-free absorption spectra. These features are observed in the attosecond transient

absorption spectra of laser-dressed helium and are experimentally manipulated as a function of NIR intensity on a few-femtosecond timescale.

Most previous studies of laser dressed helium have utilized attosecond pulse trains. Laser dressed absorption has been used to control the ionization probability of helium by rescattering [109, 111] and interference [110, 127] mechanisms. In the case of isolated attosecond pulses, recent work has focused on sub-optical cycle features [74, 115] and the Raman-like two photon mechanism [126] occurring in the absorption spectra discussed in this chapter.

4.1 Effect of NIR laser intensity on energies of LISs

Following the initial experiments presented in Chapter 3, a more in depth experimental investigation was undertaken in the Leone and Neumark groups, to study the effect near-infrared (NIR) laser intensity has on the energy locations of LIS.

The second-order transitions observed in the dressed absorption spectra of helium in the range of the $1s2p$ transition are explored here with a broader range of NIR intensities $(5 \pm 2) \times 10^{10}$ to $(1 \pm 0.4) \times 10^{13}$W/cm^2) than utilized previously [126]. The larger range of NIR intensities provides the opportunity to experimentally investigate the intensity dependence of the LISs. The NIR dressing intensity has two effects on the LISs: 1) Additional LISs appear as the dressing intensity increases. 2) The energies of the LISs may shift as the dressing intensity increases. The LISs result from the NIR laser coupling of the $1s2p$ state to the $1s3s$, $1s3d$, and $1s2s$ states of He. Both intensity dependent effects are related to the coupling strength and the detuning of the laser from the transition energy. The transient feature resulting from the $1s2p \rightarrow 1s2s$ ($1s2s$ LIS) coupling is observed for intensities above $(1.5 \pm 0.6) \times 10^{11}$, while the transient features resulting from $1s2p \rightarrow 1s3s$ ($1s3s$ LIS) and $1s2p \rightarrow 1s3d$ ($1s3d$ LIS) are seen at intensities above $(7.5 \pm 3) \times 10^{10}$. Above intensities of $(5 \pm 2) \times 10^{12}$ W/cm^2 absorption features that possibly correspond to $1s4s$, $1s4d$, $1s5s$, and $1s5d$ LISs are observed. For intensities between $(7.5 \pm 3) \times 10^{10}$ and $(1.5 \pm 0.6) \times 10^{12}$ W/cm^2, the $1s3s$ and $1s3d$ LIS may shift in energy as the NIR intensity is increased. The other absorption features are relatively stable.

4.2 Experimental

The attosecond transient absorption spectrometer has been described in detail earlier in this work, and is diagrammed in Figure 4.1. Briefly, isolated attosecond pulses are generated via high harmonic generation (HHG) with Double Optical Gating (DOG) [51, 52, 54] in a cell filled with 2.7 hPa (2 Torr) krypton gas. The DOG optics are selected so that the HHG gate width is 1.8 fs, which means that in the present case only one isolated attosecond pulse will be generated when driving harmonic generation even though the driving pulse is not carrier-envelope phase-stabilized [89].

An $f = 25$ cm Ru/Si multilayer mirror focuses the attosecond and NIR pulses into a 1 mm long absorption cell and an $f = 25$ cm Mo/Si multilayer mirror directs the transmitted

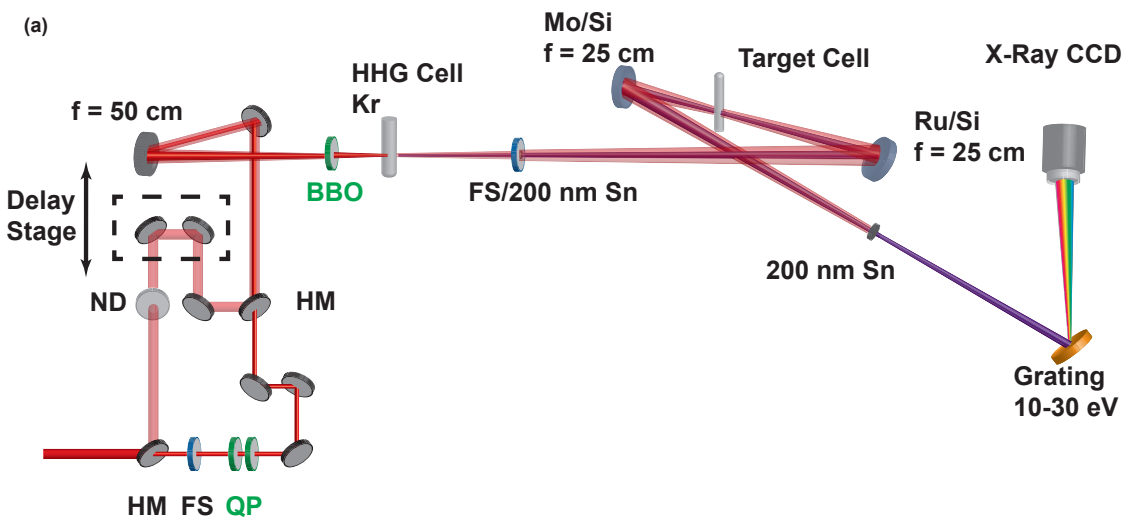

Figure 4.1: Attosecond transient absorption instrument.

attosecond pulse onto an aberration-corrected, gold-coated grating (1200 grooves/mm). An X-Ray CCD camera records the dispersed spectrum. The resulting spectral resolution is 100 meV. An interferometer incorporating an actively stabilized piezo transducer delay stage controls the delay between the NIR and attosecond pulses. In the interferometer, an annular hole mirror separates the incoming beam into an inner circular portion to drive HHG and an outer ring that serves as the optical dressing field. A neutral density filter controls the intensity of the NIR field.

Spectral interferometry for direct electric field reconstruction (SPIDER) [87] measurements characterize the 12 fs long NIR pulse. The NIR pulses are longer than the 7 fs pulses that drive HHG because the spectral broadening from the hollow-core fiber used for few-cycle pulse generation is weaker near the edges of the beam. Photoelectron streaking [59] measurements and the Frequency Resolved Optical Gating for Complete Reconstruction of Attosecond Bursts (FROG-CRAB) technique with the Principle Components Generalized Projection Algorithm (PCGPA) [91, 100, 116] characterize the attosecond pulse.

DOG produces attosecond pulses with a measured duration of 145 $\pm$ 10 as, when a 200 nm thick Al filter (band-pass of $18 - 72$ eV [90]) removes the residual NIR field. A 200 nm thick Sn filter (band-pass of $15 - 24$ eV [90]) limits the XUV spectrum to energies to just below the ionization potential of He and prevents second-order diffraction of $\sim 40 - 50$ eV photons overlapping with first-order diffraction of $\sim 20 - 25$ eV photons on the CCD camera. The resulting attosecond pulse covers the spectral range of $20 - 24$ eV and its duration is 380 $\pm$ 10 as, limited by the 24 eV high energy cut-off of the Sn filter. Material dispersion from Sn filters used to select the bandwidth of the attosecond pulse in conjunction with phase effects from the HHG process and the XUV multilayer mirror also contribute to the pulse duration.

The absorption target cell is a ~ 1 mm diameter cylindrical tube. The attosecond and

NIR beams pass through apertures laser-drilled by the femtosecond NIR HHG driver pulse prior to experiments. Gaussian beam propagation equations estimate the NIR beam diameter (twice the beam waist) at the cell walls to be 300 μm, placing an upper limit on the aperture diameter. Calibration of target gas densities uses the absorption continuum above the He ionization potential at 24.58 eV; this procedure is similar to the methods used by Loh et al. [72] to estimate target density of xenon in transient absorption measurements. Estimating the target pressure using absorption above the ionization continuum limits any effect that the relatively broad spectral resolution may have on estimating target density from much narrower absorption lines (for example, at room temperature the Doppler broadened bandwidth of the $1s2p$ resonance is on the order of 0.1 meV, while the experimental resolution is 100 meV). This calibration is performed using Xe as the HHG medium, since it has a harmonic cut-off low enough to prevent second-order diffraction from overlapping first-order diffraction on the CCD camera. An Al filter that, unlike the Sn filter, transmits photon energies above the ionization potential of the He is used to block the residual NIR light. The NIR laser intensity is estimated using the *in situ* streaking shift measured in photoelectron streaking measurements. The $1/e^2$ width of the NIR beam is 90 $\pm$ 10 μm, measured by removing the absorption cell and inserting a CCD camera into the focus in the interaction region. Gaussian beam propagation estimates the $1/e^2$ width of the XUV beam at the focus as 15 $\pm$ 1 μm.

The absorption spectra in Section 4.3 use the transmitted spectra of the attosecond pulse (without any He gas in the absorption cell) as a reference. Negative pump-probe delays correspond to cases where the attosecond pulse arrives at the target cell before the NIR pulse.

4.3 Results

The energy levels of atomic He accessible by one photon of the attosecond pulse are plotted in Figure 4.2(a). The transmitted spectra of the attosecond pulse with and without the He target gas are plotted in Figure 4.2(b) and the absolute optical density, $OD(\omega)$, is plotted in Figure 4.2(c). The absolute optical density is given by:

$$OD(\omega) = -\left[I_f(\omega)/I_i(\omega)\right] \tag{4.1}$$

where $I_i(\omega)$ is the initial spectra recorded without He target gas and $I_f(\omega)$ is the transmitted spectrum with He target gas present. The target gas density is 1.6 $\pm$ 0.05 hPa.

Peaks in the absorption spectrum corresponding to the $1s2p$, $1s3p$, and $1s4p$ transitions at 21.21, 23.09, and 23.74 eV [128] shown in Figure 4.2(a) are visible in the OD plotted in Figure 4.2 (c).

The transient absorption spectra are given by:

$$OD(\omega, t) = -\left[I_f(\omega, t)/I_i(\omega)\right] \tag{4.2}$$

where $I_i(\omega)$ is the initial spectra recorded without He target gas and $I_f(\omega, t)$ is the transmitted spectrum with He target gas present at pump-probe delay t. The target gas density is 1.6 $\pm$

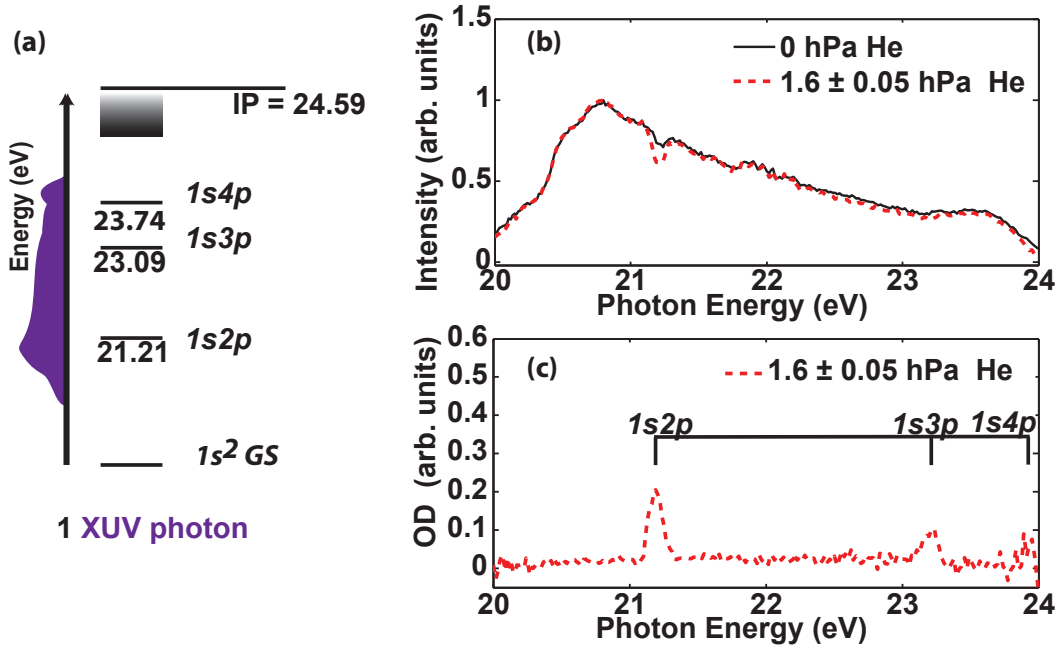

Figure 4.2: States of helium accessible in experiments. (a) Atomic states of helium in the range of the attosecond pulse. (b) Transmitted spectrum of helium and (c) OD calculated from the spectrum in (b). Transitions from $1s^2$ ground state to $1s2p$, $1s3p$, and $1s4p$ states are labeled in (c).

0.05 hPa. Figures 4.3-4.5 show transient absorption spectra plotted against pump-probe delay time for NIR intensities ranging from $(5.0 \pm 2) \times 10^{10}$ W/cm^2 to $(1 \pm 0.4) \times 10^{13}$ W/cm^2. This range of intensities, over two orders of magnitude, is more extensive than previously studied [126] and allows the intensity dependence of transient features to be investigated. Spectra were recorded for 1.5×10^5 laser pulses at each time delay step, with He target gas at a pressure of 1.6 ± 0.05 hPa.

The transient absorption spectrum recorded with the lowest NIR laser intensity, $I_0 = (5.0 \pm 2) \times 10^{10}$ W/cm^2, is plotted in Figure 4.3(a). For positive pump probe delays, the NIR pulse arrives at the target before the attosecond pulse and only features that directly correspond to the field-free absorption spectra in Figure 4.2 are visible. At zero pump-probe delay, the attosecond pulse and the NIR pulse are overlapped in time in the gas target, and a weak transient absorption feature is visible around 21.5 eV.

As the NIR intensity is increased, the transient features become more pronounced. Figures 4.3(b-c) show transient absorption spectra recorded at NIR intensities of 1.5 I_0 and 3 I_0, respectively. In Figures 4.3(b-c) two transient features A and B, that are not due to the field-free absorption spectra of He, are visible near 21.25 and 21.5 eV, respectively. Feature B is well separated from the $1s2p$ absorption peak at 21.2 eV, while feature A begins to emerge as a shoulder on the $1s2p$ absorption peak. The centroid of each feature, as a function

of pump-probe delay, has been superimposed on top of the two dimensional pump-probe experimental spectra in magenta to guide the eye. The absorption features shift in energy across the pump-probe delay scan, so defining a feature by a particular energy is difficult, but the centroids clearly identify the spectral features.

As in Figure 4.3(a), only absorption features corresponding to field-free absorption are visible at large positive pump-probe delays. For negative pump-probe delays (the attosecond XUV pulse arrives at the target before the NIR pulse) the spectra appear to be broadened and increased in intensity. There is also an asymmetry; the absorption features at negative pump-probe delays appear stronger. As described earlier in Chapter 3, the asymmetry is attributed to the increased broadening of the helium absorption lines by the NIR laser appearing as increased absorption due to detector saturation at the transition frequencies. Figure 4.4(a-c) shows the transient absorption spectra recorded with NIR intensities of 30 I_0, 100 I_0, and 200 I_0. In Figure 4.4(a), features A and B are visible, and a new feature, C, near 22 eV appears. The $1s2p$ absorption line has split into a lower energy component at 21.00 eV and feature A. In Figures 4.4(b-c) two new features, E and F, near 22.2 and 22.4 eV, respectively, are visible near zero delay. Similar to the spectra plotted in Figure 4.3, the absorption spectra plotted in Figure 4.4 are asymmetric with respect to pump-probe delay: the absorption features are stronger for negative pump-probe delays.

Line spectra at zero fs delay are plotted in Figure 4.5. In the line spectra measured with 1.5 I_0, 3 I_0,, and 30 I_0 (plotted in Figure 4.5 in teal, magenta, and green), the peaks A, B, and the $1s2p$ peak may shift in energy. Comparing the spectra measured with 1.5 I_0 to 3 I_0, the $1s2p$ absorption feature broadens and shifts lower in energy and shoulder A begins to separate from the $1s2p$ absorption peak as the intensity is increased. As the intensity increases from 3 I_0 to 30 I_0, feature A and the lower energy component of $1s2p$ further split. Feature B slightly increases in energy as the intensity is increased from 1.5 I_0 to 3 I_0 and again, as the intensity is increased from 3 I_0 to 30 I_0. At intensities of 100 I_0 and 200 I_0, no clear shifts in peak position are observed. The peak positions at zero fs delay are listed in Table 4.1.

The origin of the new transient absorption features and the splitting of the $1s2p$ absorption feature at the overlap of the XUV attosecond pulse and the NIR pulse will be discussed in more detail in Section 4.4. The changes in the photon energies of the absorption features and the variations with intensity necessary to observe the features will be discussed.

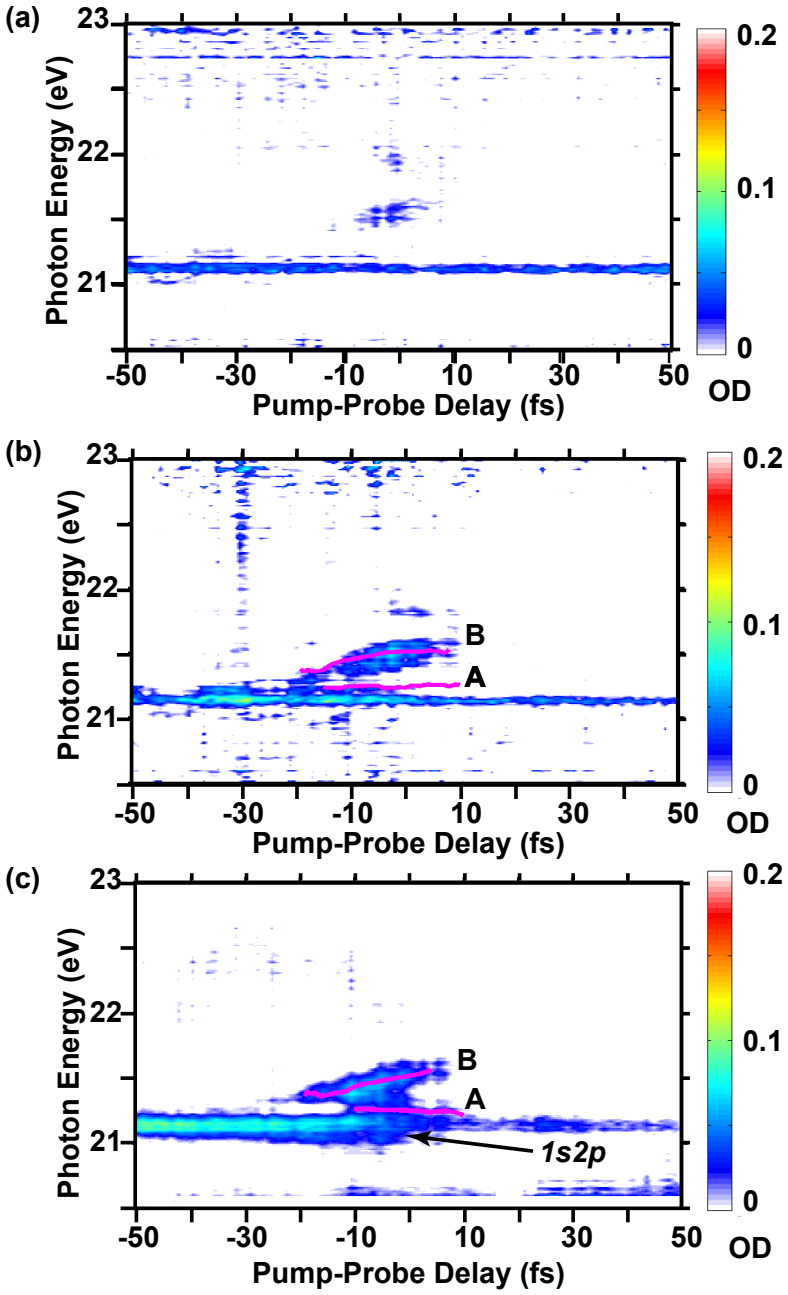

Figure 4.3: Transient absorption spectra recorded with NIR intensity of $I_0 = (5.0 \pm 2) \times 10^{10}$ W/cm^2(a), 1.5 I_0 (b), and 3 I_0 (c). Features near zero femtosecond delay are labeled according to the text and the centroid of each peak, as function of pump-probe delay, is superimposed in magenta.

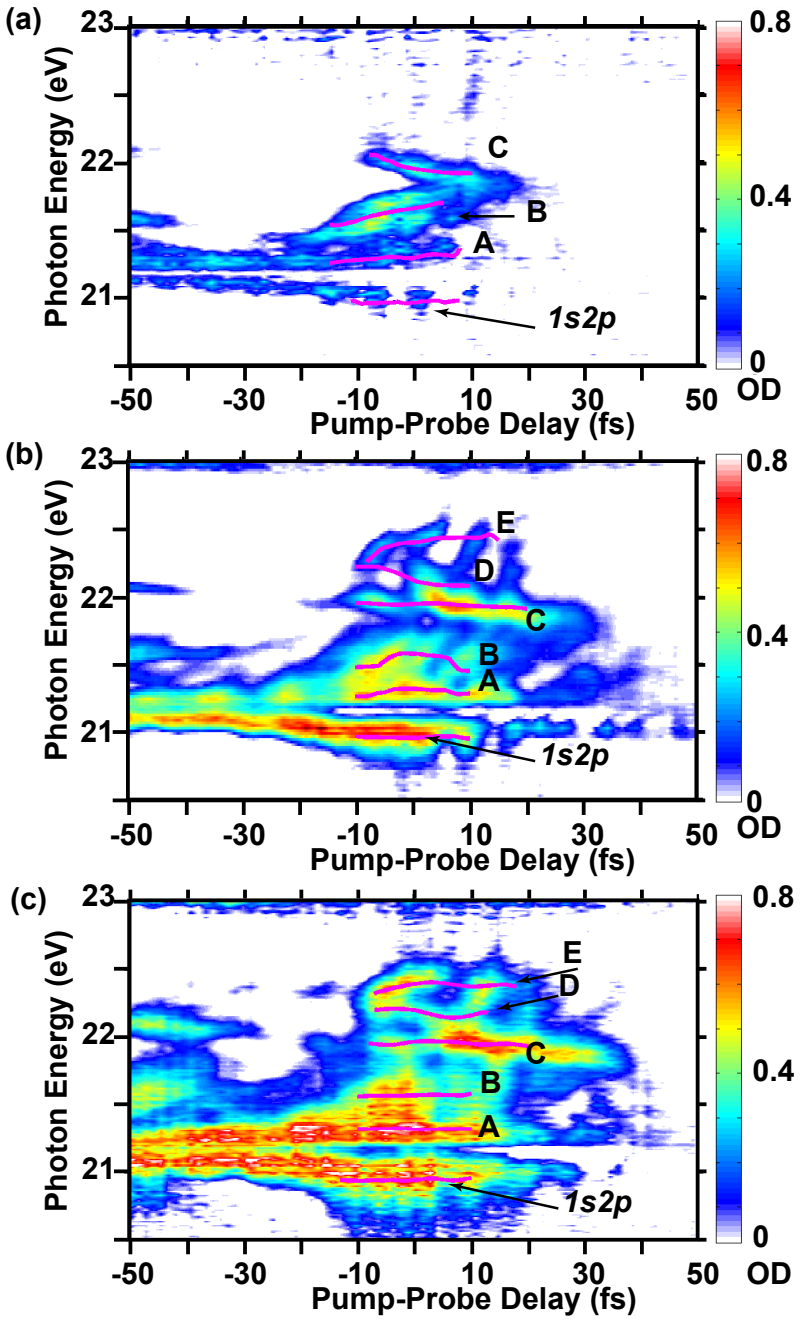

Figure 4.4: Transient absorption spectra recorded with NIR intensity of 30 I_0 (a), 100 I_0 (b), and 200 I_0 (c). Features near zero delay are labeled according to the text and the centroid of each peak is superimposed in magenta.

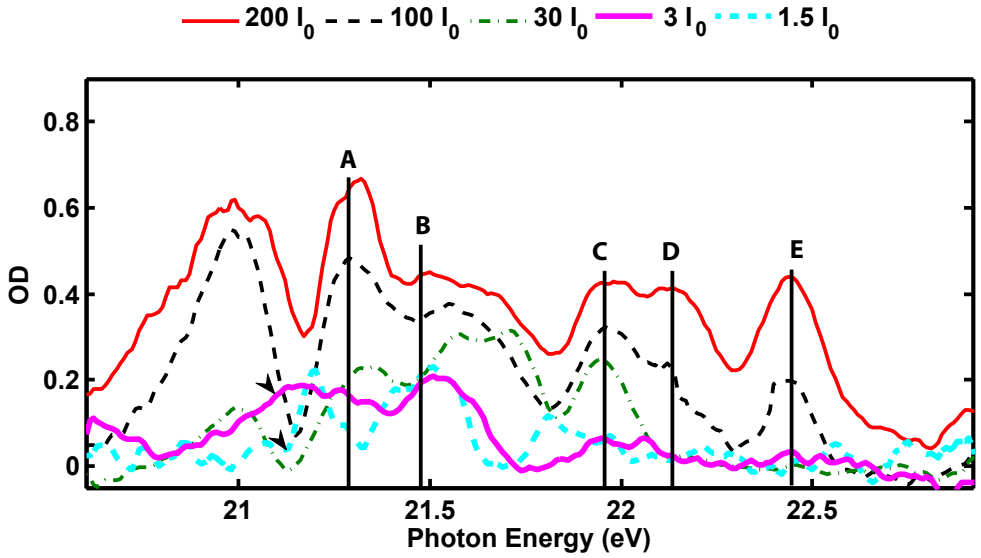

Figure 4.5: Line spectra at zero femtosecond pump-probe delay recorded with NIR intensity of 200 (red solid), 100 (black dashed), 30 (green dot-dashed), 3 (magenta solid), and 1.5 (teal dashed) I_0. 3 and 1.5 I_0 have been scaled by a factor of 3. Features near zero femtosecond delay are labeled according to the text. Vertical lines correspond to two-photon transitions described in Section 4.4.

	Peak position (eV)					
Intensity	$1s2p$	A	B	C	D	E
1.5 I_0	21.20	21.25	21.50			
3 I_0	21.15	21.30	21.55			
30 I_0	21.00	21.35	21.65	21.95		
100 I_0	20.95	$\sim$ 21.3	$\sim$ 21.6	21.95	22.15	22.4
100 I_0	20.95	$\sim$ 21.3	$\sim$ 21.6	21.95	22.15	22.4

Table 4.1: Positions of absorption features at zero pump-probe delay. The positions are taken as the value of the centroids plotted in Figures 4.3 and 4.4 at 0 fs.

4.4 Analysis and discussion

Near zero pump-probe delay, features in the absorption spectra that are not present in the field-free absorption spectra occur (for example at 21.25 eV and 21.50 eV in Figure 4.3). Following the approach described previously [126], the absorption features near zero femtoseconds pump-probe delay are interpreted as light-induced states (LISs) that are the intermediate step in the Raman-like two photon transitions from the ground state of He to $1snx$ and $1snd$ excited states of He. The two photon pathway is shown by:

$$\begin{aligned}
&1s^2 \overset{h\nu_{XUV}}{\rightarrow} 1s3s\ LIS(\text{feature A}) \overset{+h\nu_{NIR}}{\rightarrow} 1s3s \\
&1s^2 \overset{h\nu_{XUV}}{\rightarrow} 1s3d\ LIS(\text{feature B}) \overset{+h\nu_{NIR}}{\rightarrow} 1s3d \\
&1s^2 \overset{h\nu_{XUV}}{\rightarrow} 1s2s\ LIS(\text{feature C}) \overset{-h\nu_{NIR}}{\rightarrow} 1s2s \\
&1s^2 \overset{h\nu_{XUV}}{\rightarrow} 1s4s/d\ LIS(\text{feature D}) \overset{+h\nu_{NIR}}{\rightarrow} 1s4s/d \\
&1s^2 \overset{h\nu_{XUV}}{\rightarrow} 1s5s/d\ LIS(\text{feature E}) \overset{+h\nu_{NIR}}{\rightarrow} 1s5s/d
\end{aligned} \tag{4.3}$$

The energies of the LIS are approximately:

$$\begin{aligned}
\hbar\omega_A &= \hbar\omega_{1s3d\ LIS} \approx \hbar\omega_{1s3d} - \hbar\omega_{NIR} \\
\hbar\omega_B &= \hbar\omega_{1s3s\ LIS} \approx \hbar\omega_{1s3s} - \hbar\omega_{NIR} \\
\hbar\omega_C &= \hbar\omega_{1s2s\ LIS} \approx \hbar\omega_{1s2s} + \hbar\omega_{NIR} \\
\hbar\omega_D &= \hbar\omega_{1s4s/d\ LIS} \approx \hbar\omega_{1s4s/d} - \hbar\omega_{NIR} \\
\hbar\omega_E &= \hbar\omega_{1s5s/d\ LIS} \approx \hbar\omega_{1s5s/d} - \hbar\omega_{NIR}
\end{aligned} \tag{4.4}$$

Vertical lines plotted in Figure 4.5 correspond to the energies given by Equation 4.4. The energy of the $1s2s$ LIS (feature C at 21.95 eV) is offset from the value given by Equation 4.4 (22.21 eV). The two photon transitions are diagrammed in Figure 4.6.

For example the absorption features A and B at 21.25 and 21.50 eV in Figure 4.4(a) result from absorption of one photon from the XUV attosecond pulse and absorption of one photon of NIR to reach, respectively, the $1s3s$, and $1s3d$ states of He. Similarly, feature C at 21.95 eV in Figure 4.4(a) acts as the intermediate step in a two photon pathway connecting the ground state to the $1s2s$ state by absorption of one XUV photon and emission of one NIR photon. Features D and E in Figures 4.4(b-c), which were not previously observed in lower intensity measurements, may be the intermediate step in a two photon absorption process to reach the $1s4s$ and $1s4d$ (D) states and the $1s5s$ and $1s5d$ (E) states of He; analogous to the mechanism producing features A and B.

The experimental resolution (0.1 eV) combined with the NIR laser bandwidth (0.3 eV) prevents the $1s4s$ and $1s4d$ or the $1s5s$ and $1s5d$ LIS from being resolved. At intensities of 100 I_0 and 200 I_0, the absorption spectra become increasingly complex near zero delay with broad absorption features, possibly due to multiplet splitting of the LISs. Multiplet splitting of absorption features is predicted [122] and observed [125] for high-field dressed absorption measurements of atomic xenon in the XUV spectral region. Due to the possibility of multiplet splitting and increasing complexity of the absorption spectra, the assignments of the $1s4s/d$

and $1s5s/d$ LISs are tentative. Equations 4.3 and 4.4 are convenient for identifying the new absorption features, but the equations do not directly identify which states of helium are interacting.

Figure 4.6 compares the calculated positions of the $1s2s$, $1s3d$, and $1s3s$ LISs calculated previously [126] with the experimentally observed features C, B, and A as a function of field intensity. In the calculations the single atom frequency dependent response has been calculated using the methods detailed in Ref. [108]. For intensities up to 30 I_0, the positions of features A and B are reasonably correlated to the calculated positions of the $1s3s$ and $1s3d$ LISs. At higher intensities there is a discrepancy between features A and B and the calculated positions of the LISs. The inconsistency between the calculations and the current experimental results (in addition to similar behavior observed in Ref. [74]) suggest an open avenue for further study. With this in mind, the analysis will focus on why the energies of the $1s3s$ and $1s3d$ LIS are sensitive to changes in the field intensity (at least for intensities between 1.5 and 30 I_0).

Further analysis of the positions of the LISs will utilize the dressed absorption perspective, where a manifold of states that correspond to the emission and absorption of successive NIR laser photons are coupled [129, 130]. When the energy difference between the field-free transition frequency and the dressing frequency ($\hbar\omega_{1s2p} - \hbar\omega_{NIR}$) is large compared to the interaction between the coupled states, dressed absorption can be interpreted as two photon transitions, similar to the Raman-like mechanism described previously [129]. The advantage of this interpretation is that it explicitly takes into account which field-free states are interacting and the frequency shifts of absorption features can be straightforwardly interpreted without calculating the polarization field (as in prior XUV dressed absorption calculations [76, 108, 122, 125]). The following model is less sophisticated than methods of Chen, Gaarde, Schafer, and co-workers [108], where the time-dependent Schrödinger equation for a quantum atom in a semi-classical electric field is solved. The non-perturbative calculations by Chen, Gaarde, Schafer, and co-workers include effects that depend on the electric field at many degrees of nonlinearity. However, the model described here can provide insight into dressed absorption with a significantly smaller layout of computational resources.

The second-order perturbation theory correction to the energy of a state (E_n) in an oscillating electric field is given by [129, 130]:

$$E_n = \frac{1}{4}\sum_{m\neq n}\{\frac{\left|\overrightarrow{E_0}\bullet\overrightarrow{d_{nm}}\right|^2}{E_n - E_m - \hbar\omega_{NIR}} + \frac{\left|\overrightarrow{E_0}\bullet\overrightarrow{d_{nm}}\right|^2}{E_n - E_m + \hbar\omega_{NIR}}\} \tag{4.5}$$

where $\overrightarrow{E_0}$ is the electric field vector, $\overrightarrow{d_{nm}}$ is the transition dipole for field-free states n and m with energies E_n and E_m, respectively. In the present case, the $1s2p$ state is coupled to the $1s3s$, $1s3d$, and $1s2s$ states via one photon transitions, resulting in features A, B, and C and a shifted $1s2p$ absorption peak. Features D and E in Figures 4.4(b-c) may result from either the $1s2p$ or the $1s3p$ coupling to the $1s4s/d$ and $1s5s/d$ states via one photon transitions. The $1s3p$ state is expected to have the larger contribution because the NIR photon energy is close to resonance for the $1s3p \rightarrow 1s4s/d$ and $1s3p \rightarrow 1s5s/d$ transitions

than for the $1s2p \rightarrow 1s4s/d$ and $1s2p \rightarrow 1s5s/d$ transitions and the transition dipoles for the $1s3p \rightarrow 1s4s/d$ and $1s3p \rightarrow 1s5s/d$ pathways are larger [119].

Equation 4.5 depends on the magnitude of $\overrightarrow{E_0} \bullet \overrightarrow{d_{nm}}$ and the energy difference between the atomic transition and the photon energy of the dressing field (i.e. the detuning). The detunings of the dressing laser frequency from the field-free atomic transition and the Rabi frequencies ($\Omega_r = \frac{-1}{\hbar}\overrightarrow{E_0} \bullet \overrightarrow{d_{nm}}$) calculated at 30 I_0 (1.5×10^{12} W/cm^2) are listed in Table 4.2. These values correspond to the denominator and numerator terms in Equation 4.5. Also listed in Table 4.2 are the E_n for the LIS calculated from Equation 4.5. For example, the detuning for the $1s3s$ LIS, (feature A), is smaller than the Rabi frequency, therefor the E_n calculated from Equation 4.5 is larger than the converse case. The central energy of the NIR laser is 1.6 eV (390 THz), and the bandwidth is 0.3 eV (∼73 THz), so the $1s3s$ and $1s3d$ LISs are resonant or near-resonant with the laser frequency. Transition dipoles are taken from Ref. [119]. The field intensity used to calculate the parameters in Table 4.2 is 30 I_0, because 30 I_0 is the largest intensity where a shift in energy is observed in experimental results. The shifts in Figure 4.6 calculated by Chen, Gaarde, Schafer, and co-workers [126], however, increase at higher intensities.

From Table 4.2, the detunings for the $1s3s$ and $1s3d$ LIS (features A and B) are considerably smaller than the detunings for the other LISs (features C, D, and E), therefore the $1s3s$ and $1s3d$ LIS are expected to appear at lower NIR field strengths. Direct comparison of the onset intensities between the n = 4 and 5 LIS and the n = 2 and 3 LIS may be complicated because the n = 4 and 5 LISs most likely result from coupling of the $1s3p$ state while the n = 2 and 3 LISs result from coupling of the $1s2p$ state.

Equation 4.5 yields the largest energy corrections for the $1s3s$ and $1s3d$ LIS (features A and B). These are the states that are closest to resonance with the NIR coupling field, and the states that may increase in energy as the field intensity increases at field intensities up to 30 I_0. Equation 4.5 overestimates the energy shifts, as compared to the results of Chen, Gaarde, Schafer, and co-workers in Figure 4.6, but both the calculations of Chen, Gaarde, Schafer, and co-workers and Equation 4.5 predict the smallest shift for the $1s2s$ LIS. Equation 4.5 serves as a cursory gauge of relative tendency of LIS to shift in response to field intensity. The coupling also results in the $1s2p$ absorption peak decreasing in energy as the field intensity increases; however, due to the multiple couplings of the $1s2p$ state (for example coupling to the $1s2s$, $1s3s$, and $1s3d$ states) the intensity dependence of the $1s2p$ state is not straightforward to interpret.

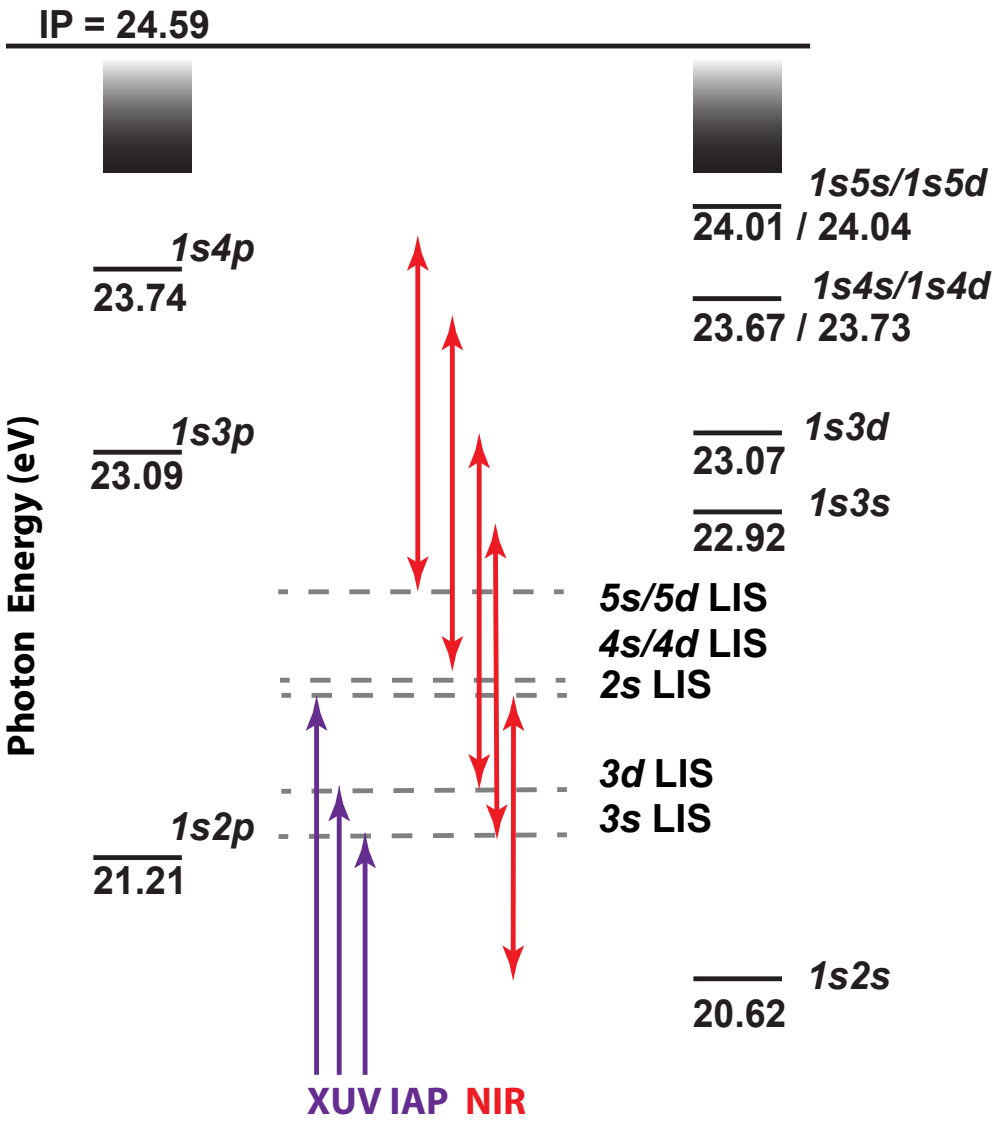

Figure 4.6: Mechanism for light-induced states. The attosecond XUV pulse where the NIR field (red arrows) couple the states to surrounding ns and nd states.

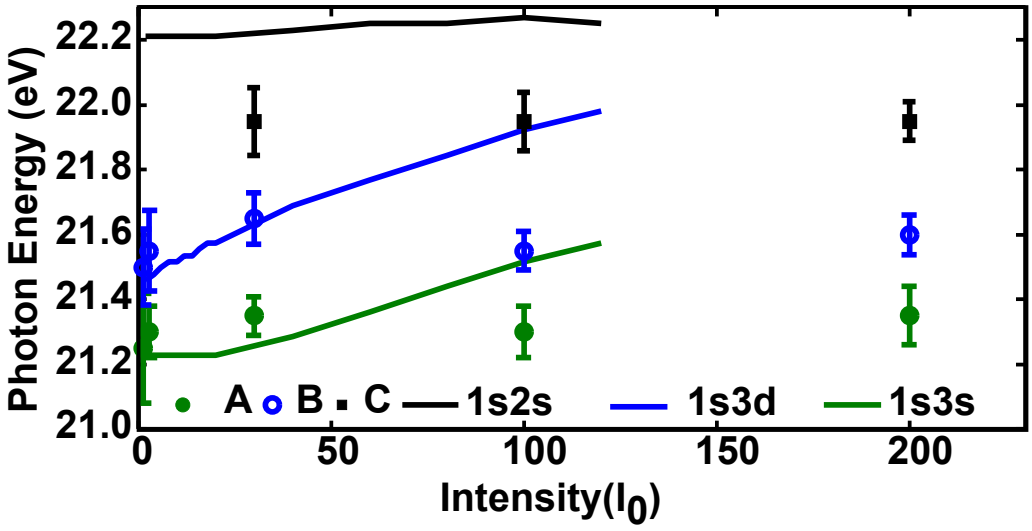

Figure 4.7: The positions of the experimental absorption features A (green filled circles), B (blue open circles) and C (black filled squares) are plotted as a function of dressing intensity. The calculated positions of the LISs from Ref. [126] are plotted for comparison.

LIS	*Feature*	Detuning		RabiFrequency at 30 I_0 (1.5×10^12 W/cm^2)		E_n	
		(THz)	(eV)	(THz)	(eV)	(THz)	(eV)
$1s3s$	A	-26	-0.11	80	0.3	60	0.26
$1s3d$	B	-62	-0.26	130	0.55	75	0.31
$1s2s$	C	240	1	220	0.9	25	0.11
$1s4s/d$	C	-240	-1	210	0.85	-25	-0.1
$1s5s/d$	E	-170	-0.7	80	0.3	-7	-0.03

Table 4.2: The detunings, Rabi frequencies, and E_n calculated from Equation (4.5). Both frequency and energy units are given. The LISs that have the largest E_n have the largest ratio of Rabi frequency to detuning. The transition dipoles are taken from Ref. [119].

4.5 Conclusions and future outlook

Attosecond transient absorption spectroscopy is employed to measure the intensity dependence of LISs in the absorption spectra of helium in the region of the $1s2p$ resonance at 21.21 eV. At intensities of $(7.5 \pm 3) \times 10^{10}$ W/cm^2 LISs resulting from coupling of $1s2p$ to $1s3d$ and $1s3s$ states are observed, while the LIS resulting from the coupling of $1s2p$ to $1s2s$ state is visible at intensities of $(1.5 \pm 0.6) \times 10^{11}$ W/cm^2. Above intensities of $(5 \pm 2) \times 10^{12}$ W/cm^2 absorption features that likely correspond to $1s4s/d$ and $1s5s/d$ LISs are observed. The $1s3s$ and $1s3d$ LISs may increase in energy as the NIR intensity is increases. The difference in intensity response is attributed to the detuning of +240 THz (+1.0 eV) for the $1s2p \rightarrow 1s2s$ transition, compared to -62 THz or -26 THz (-0.26 or -0.11 eV) for the $1s2p \rightarrow 1s3d$ and $1s2p \rightarrow 1s3s$ transitions. These considerations will be useful for the preparation of state specific samples in future measurements, as well as future attosecond pump-probe spectroscopy measurements, where the wavelength and intensities of the optical pulses can be selected so that specific atomic and molecular states are affected more strongly than others. For example, in attosecond transient absorption measurements of autoionization lifetimes, the optical pulse can be selected to strongly couple an autoionization resonance to other nearby states, or the optical pulse can be selected to favor a multiphoton ionization process.

Several studies have focused on features in the absorption spectrum that oscillate on timescales faster than the optical period of the NIR field [74, 112, 115, 126]. These sub-optical-cycle features result from interference between one and multiple (two and three) photon pathways to reach bound states either directly or via a bound intermediate state. Future investigations of sub-cycle features can provide intriguing opportunities to study experimental targets where there may be some nuclear dynamics that will curtail the interference on a characteristic timescale. For example, the bound states of a dissociating molecule may shift so that an intermediate or final state in the multiphoton pathway is no longer resonant or near resonant with the field and the interference is suppressed.

Chapter 5

Measurement of ultrashort lifetimes: $5s5p^6 6p$ and $5s5p^6 7p$ autoionizing states of xenon

5.1 Ultrashort lifetime measurements

Time-resolved spectroscopy with isolated attosecond pulses has the potential to measure ultrashort lifetimes [7–9, 11, 39]. Several previous works have focused on autoionization decay mechanisms because autoionization is driven by electron-electron interactions, and occurs on timescales ranging from picoseconds to attoseconds [131–134]. One of the earliest applications of attosecond spectroscopy was measurement of ultrashort lifetimes of core-hole excited states in atomic krypton that rapidly decay via an autoionization process, specifically Auger decay [11]. Photoelectron streaking measurements determined the emission time of the ejected Auger electrons. The dynamics of short-lived states may also be ascertained from absorption spectroscopy measurements, where sharp resonances result from the two pathway interference between direct ionization and ionization mediated by a short-lived state. Time-resolved absorption measurements with isolated attosecond pulses demonstrated retrieval of lifetimes of autoionizing $3s3p^6 4p$ and $3s3p^6 4p$ states of argon where one electron from the inner valence $3s$ orbital has been promoted to a $4p$ or $5p$ orbital [3]. In addition to determining lifetimes of states, transient absorption studies of autoionizing states have observed multielectron dynamics and strong field effects. Interesting experimental and theoretical work has focused on changes to the autoionization lineshape of by coupling the autoionizing $2s2p$ and $2s^2$ states of helium at 60.15 and 62.06 eV using both attosecond and femtosecond trains of high harmonics [124, 135, 136]. The Autler-Townes splitting of autoionizing states in atomic xenon has been measured using femtosecond XUV absorption spectroscopy and theoretically studied for isolated attosecond pulses [122, 125]. This chapter focuses on preliminary measurements of the $5s5p^6 6p$ and $5s5p^6 7p$ autoionizing states of atomic xenon.

5.1.1 Fano resonances

The line shape of atomic states below the ionization threshold has a characteristically Lorentzian line shape and the lifetimes of the state corresponds to the resonance linewidth by the uncertainty principle:

$$\Delta E \Delta t \geq \hbar \tag{5.1}$$

where ΔE is the measured linewidth, Δt is the lifetime of the state. For atomic states that lie above the ionization potential, like the autoionization resonances mentioned, an asymmetric and broader line shape can be observed. The lineshape becomes asymmetric due to the possibility for two pathway interference between ionization channels: either direct ionization to the continuum or excitation to a short-lived state followed by ionization. The linewdiths are greater because the autoionization decay rates are faster than those due to fluorescence. Autoionization lifetimes (on the order of attoseconds to picoseconds) are significantly shorter than fluorescence lifetimes (hundreds of picoseconds to nanoseconds); and, as a consequence, autoionizing states do not fluoresce significantly. The measured lifetime of the state is given by:

$$\frac{1}{\tau_m} = \frac{1}{\tau_{ai}} + \frac{1}{\tau_f} \tag{5.2}$$

where τ_m is the measured lifetime of the state, τ_{ai} is the autoionization lifetime, and τ_f is the fluorescence lifetime. The contribution of τ_f to the measured linewidths of autoionizing resonances is small and may be neglected.

Fano [131, 132] described autoionizing states as an unobservable discrete state (ϕ) coupled via configuration interaction to a set of continuum states ($\psi_{E'}$)

$$\Phi = \phi + P \int \frac{V_{E'} \psi_{E'}}{E - E'} \tag{5.3}$$

where Φ is the modified observable state, and $V_{E'} = \langle \phi | H | \psi_{E'} \rangle$ is the interaction between the discrete and continuum states. The P indicates that the integral is the Cauchy principal part. The spectral profile is given by:

$$I(\epsilon) = \frac{(q + \epsilon)^2}{1 + \epsilon^2} \tag{5.4}$$

where q is the parameter that describes lineshape (or profile index), $\epsilon = \frac{E - E_r - \delta_E}{\frac{1}{2}\Gamma}$ is the reduced energy variable, E is the excitation energy, E_r is the resonance energy, δ_E is the shift in resonance energy due to configuration interaction, and $\Gamma = 1/\tau_{ai}$ is the linewidth. The Fano parameter q is given by:

$$q = \frac{\langle \Phi | d | i \rangle}{\pi V_E^* \langle \psi_E | d | i \rangle} \tag{5.5}$$

where d is the transition dipole operator and $|i\rangle$ is the initial state of the atom or molecule. A rearrangement of q (with the substitution of $\Gamma = 2\pi |V_E|^2$) provides the result:

$$\frac{1}{2}\pi q^2 = \frac{|\langle \Phi | d | i \rangle|^2}{|\langle \psi_E | d | i \rangle|^2 \Gamma} \tag{5.6}$$

Equation 5.6 shows that the square of the Fano parameter is proportional to the ratio of the transition probabilities to the modified discrete state Φ, and a range of continuum states with a bandwidth equal to Γ. Representative plots of transition profile are plotted for several values of q in Figure 5.1. For small values of q the line shape is a window resonance, so called

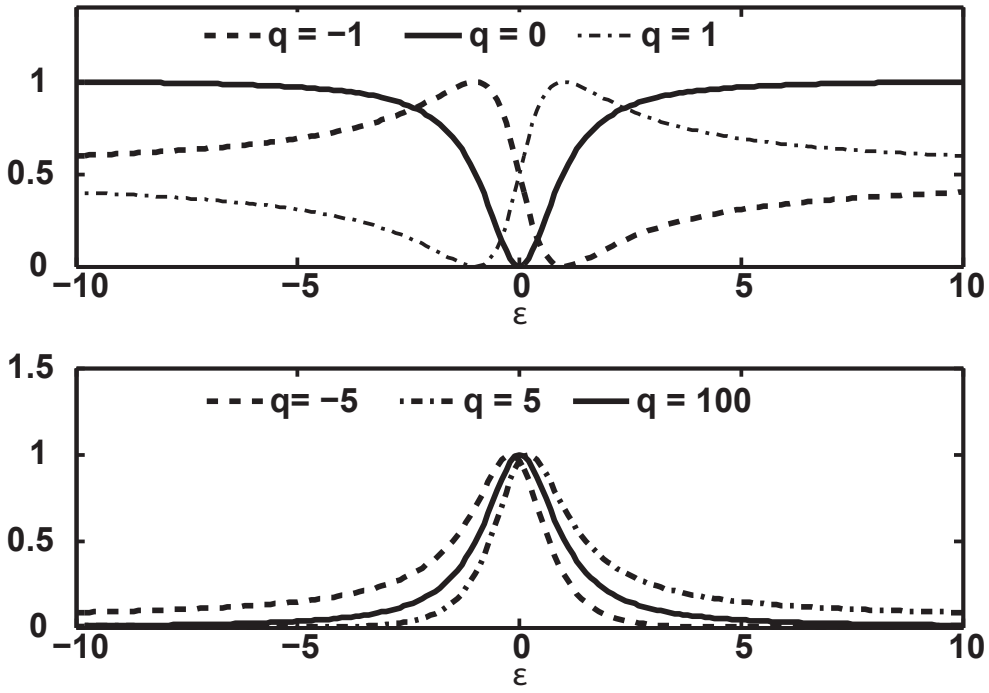

Figure 5.1: Spectral profile for representative values of q.

because the cross section on resonance is less than the surrounding areas. As q increases in size the interaction between the admixture of continuum states and the discrete state decreases and the resulting profile becomes a Lorentzian lineshape. For $q = \pm 1$ the contributions from both the direct ionization and indirect pathways are comparable and the spectral shape has the largest interference.

5.1.2 Xe $5s5p^6 6p$ and $5s5p^6 7p$ autoionizing states

The absorption cross section of the $5s5p^6 6p$ and $5s5p^6 7p$, are shown in Figure 5.2(a) [128]. The cross section was determined by electron energy loss measurements and converted to optical absorption. The high resolution absorption cross section in the region of the $5s5p^6 6p$ state is plotted in Figure 5.2(b) [134]. The absorption spectra in Ref. [134] were acquired by monitoring the transmission of synchrotron radiation (via the signal from a tungsten photocathode) as the frequency is scanned across the autoionization resonance.

The high resolution measurements feature additional peaks in the vicinity of the autoionization resonance identified in Figure 5.2(b), at least two of the peaks labeled 2, 3, and

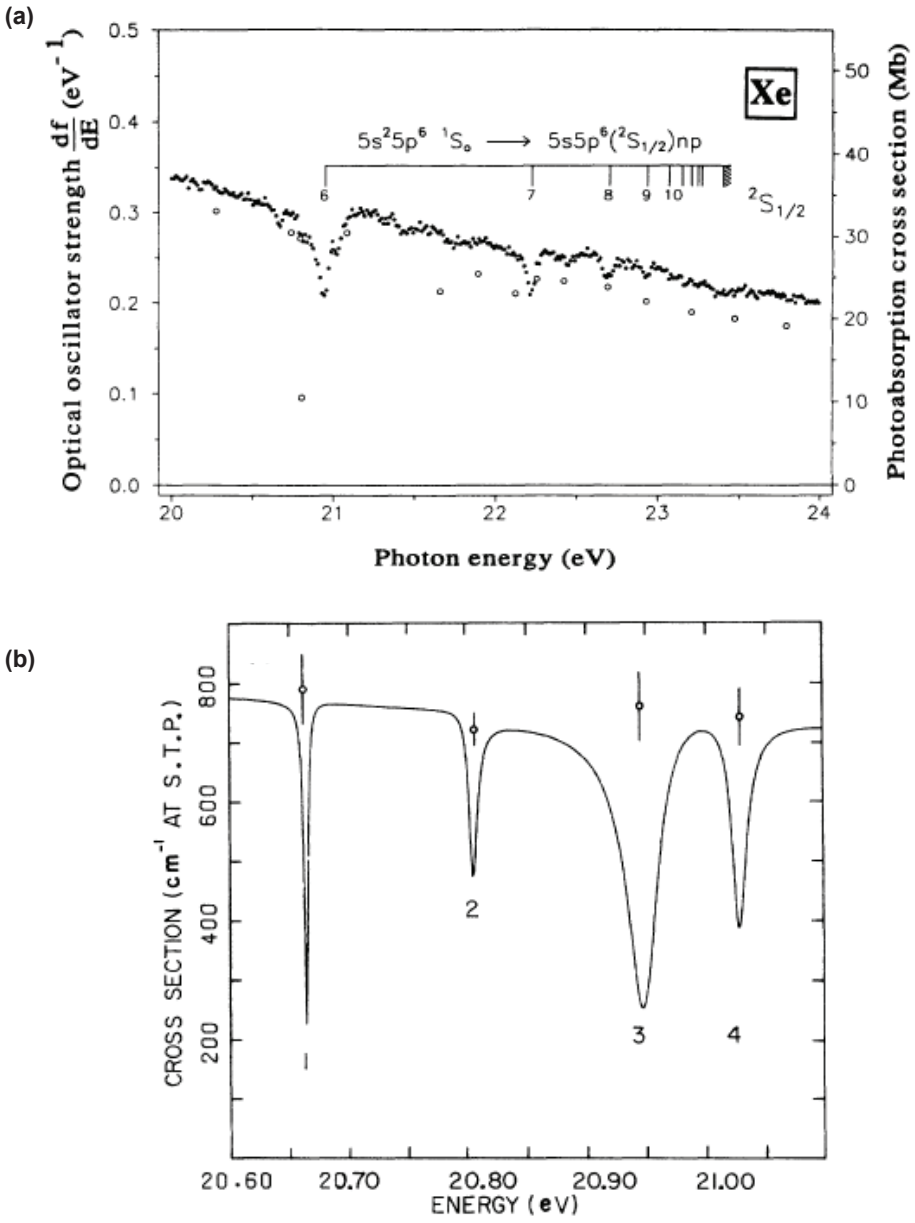

Figure 5.2: (a) The measured absorption cross section of Xe in the region of the $5s5p^66p$ to $5s5p^610p$ autoionizing states [128]. (b) High resolution measurement of the absorption cross section in the region of $5s5p^66p$ state with several peaks, at least two of which comprise a spin-orbit pair [134]. Open circles indicate the value of the non-resonant cross section and the bar represents one standard deviation.

state	q	E_r (eV)	Γ (meV)	τ (fs)
$5s5p^6 6p$	0.23 ± 0.04	20.951	31.2 ± 0.08	22.1
$5s5p^6 7p$	0.16 ± 0.04	22.226	13.02 ± 0.06	50.1

Table 5.1: Spectroscopic parameters for autoionization resonances measured in atomic Xe from Refs. [133, 134].

4 are thought to be the spin-orbit pairs of the $5s5p^6 6p$ state [137–140]. The $5s5p^6 6p$ and $5s5p^6 7p$ excited states of Xe are not well described by LS angular momentum coupling, and instead are described by jj coupling. In the case of jj coupling the j for each electron is coupled to produce a total J, in contrast to LS coupling where the total L and S from the electrons is used to calculate a total J [141]. For one photon transitions from the $^1S_0$ ground state (well described by LS coupling) of Xe, selection rules dictate that $\Delta J = 0, \pm 1$, for linearly polarized light $\Delta M_J = 0$, and Π, the parity of the state, must be odd ($\Pi = -1$). The autoionizing states are described by $(j_c, j_e)_J$, where J is the total angular momentum, j_c and j_e are the angular momentum of the unpaired $5s$ ("core") and $6p$ or $7p$ ("excited") electrons, respectively. The autoionizing states of Xe must have $J = 1$. The $5s$ electron may have $j_c = 1/2$ and the excited $6p$ or $7p$ electron may have either $j_e = 1/2$ or $j_e = 3/2$. The two allowed configurations to produce $J = 1$ are $(1/2, 1/2)_1$ and $(1/2, 3/2)_1$. Respectively, the $(1/2, 3/2)_1$ and the $(1/2, 1/2)_1$ states correlate to the singlet and triplet states that result from LS coupling. High resolution measurements in the vicinity of the $5s5p^6 7p$ are not available at this time. As a consequence, measurement of the $5s5p^6 6p$ and $5s5p^6 7p$ lifetimes may be complicated by the presence of multiple states, each with their own autoionization lifetime. The spectroscopic parameters for the $5s5p^6 6p$ and $5s5p^6 7p$ autoionizing states are shown in Table 5.1 [133, 134].

Figure 5.3 is an energy level diagram in the vicinity of the autoionization states.

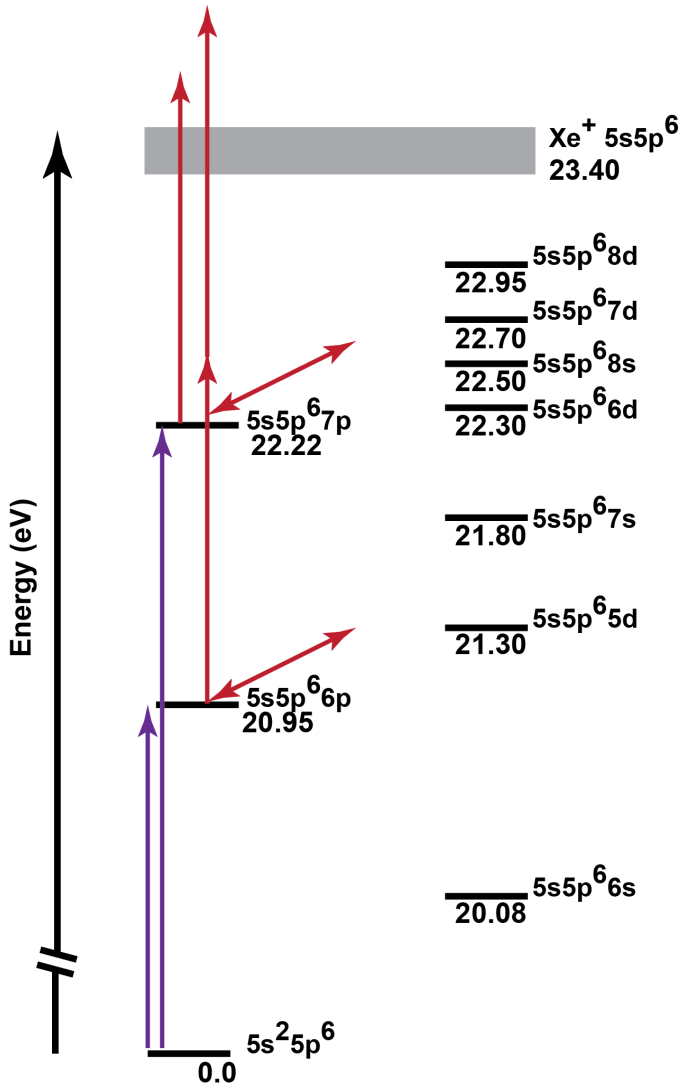

Figure 5.3: Energy level diagram for states of Xe near the $5s5p^6 6p$ and $5s5p^6 7p$ autoionizing states [133, 134, 142, 143]. The states on the left hand side are accessible via one photon from the XUV attosecond pulse. A time delayed near-infrared (NIR) pulse may couple the autoionizing states to the states (with $l = s$ & d) on the right hand side, that are not accessible via one photon transitions from the ground state. The autoionizing states may be ionized by one or two NIR photons to the $5s5p^6$ state of Xe^+.

5.2 Experimental

5.2.1 Experimental details

The experimental system is similar to those described in previous works [54, 126] and described in detail in Chapter 2. The output of a chirped-pulse amplifier, titanium:sapphire

laser system ($780\ \text{nm}, 20-25\ \text{fs}, 2\ \text{mJ/pulse}, 1\ \text{kHz}$) is spectrally broadened in a 400 μm inner diameter hollow core fiber filled with 2 bar Ne gas. The resulting pulse is directed to a set of chirped mirrors to compress the output to 7 fs. The pulse is sent to an interferometer to control the pump-probe delay. Hole mirrors in the interferometer separate the beam into two portions: the inner circular beam will generate high harmonics, the outer ring shaped beam is the optical pulse used in pump-probe experiments. The pulse duration of the inner beam is 7 fs, the pulse duration of the outer beam is 12 fs.

Isolated attosecond pulses are generated using double optical gating and ~ 2 Torr krypton gas as the harmonic up conversion medium. A 200 nm thick tin filter spectrally limits the attosecond pulse to a spectral range of $20-24$ eV. The pulse duration as measured by photoelectron streaking is ~ 400 as. The attosecond and optical pulses are focused into an absorption cell by a $f = 50$ cm spherical Ru/Si multilayer mirror (NTT Advance Technologies). The 1 mm long static absorption cell holds Xe at a backing pressure of 5 Torr. The transmitted XUV spectrum is recollected by a Mo/Si multilayer mirror ($f = 50$ cm; NTT Advance Technologies) and directed through a 200 nm thick Sn filter to a 1200 grooves/mm, gold-coated grating (Hitachi High Technologies model 001-0464). An X-Ray CCD camera records the dispersed spectrum for computer acquisition. Prior to the measurements, a spectrum is recorded with only the optical pulse focused into the absorption cell and no attosecond pulse to determine if the optical pulse is capable of producing high harmonics in the absorption cell. This spectrum is flat and at zero spectral intensity indicating that no high harmonics are generated in the absorption cell.

5.2.2 Absorption spectra

Static transmitted spectra are shown below in Figure 5.4 and converted to optical density in Figure 5.5. The optical density is computed as:

$$OD(E) = -Log\left[\frac{I_f(E)}{I_i(E)}\right] \tag{5.7}$$

where $I_f(E)$ is the measured spectrum with target gas in the absorption cell and $I_i(E)$ is the measured spectrum with no target gas in the absorption cell.

The absorption spectra have a background of absorption that corresponds to direct ionization of Xe to Xe^+. Features superimposed in the absorption spectra corresponding to the $5s5p^6 6p$ and $5s5p^6 7p$ states identified before are clearly visible. However, the multiple peaks identified in the high resolution absorption measurements of Ederer et al. [134] near the $5s5p^6 6p$ resonance are not resolved.

The experimental spectra are fit with the following parameterization [134] in Figure 5.6:

$$\sigma(E) = \sigma_c + \frac{\sigma_a q \frac{\Gamma}{2}(E - E_{res}) + \sigma_a(q^2-1)(\frac{\Gamma}{2})^2}{(E-E_{res})^2 + (\frac{\Gamma}{2})^2} \tag{5.8}$$

where $\sigma(E)$, σ_c, and σ_a are the measured cross section, the continuum cross section, and the cross section for continuum states interacting with autoionizing state, respectively. As before,

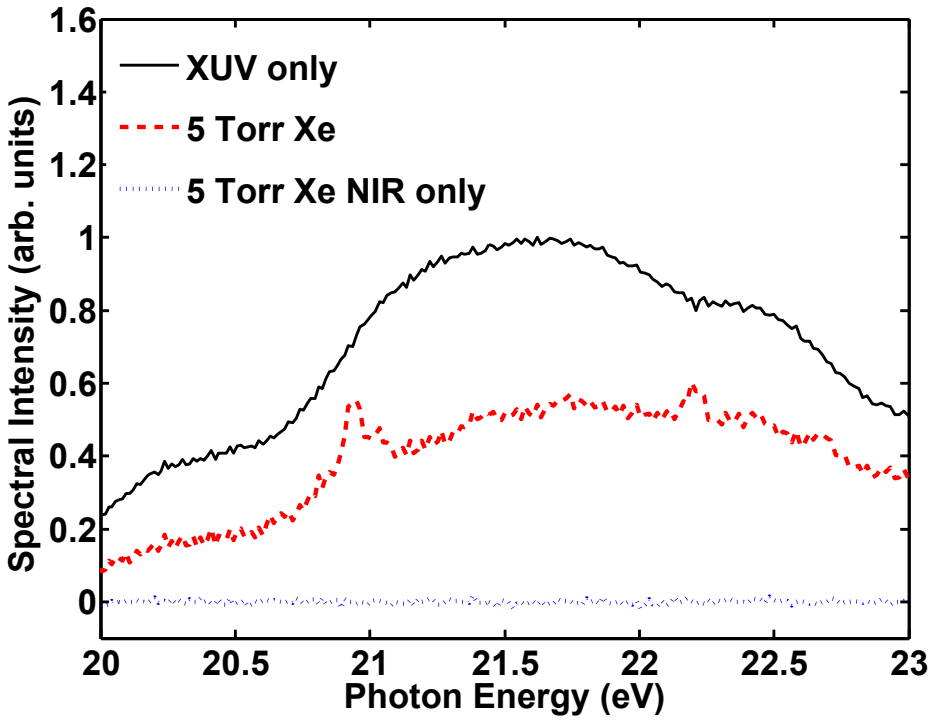

Figure 5.4: Transmitted spectra in the region of the $5s5p^6 6p$ and $5s5p^6 7p$ autoionizing states of atomic Xe. The autoionizing states have q values close to 0 and so appear as window resonances. The dotted line is the spectrum recorded with no attosecond pulse, verifying that the optical pulse cannot produce harmonic radiation in the absorption cell. The spectra are recorded for a total of 3×10^5 laser pulses.

q is the profile index, Γ is the linewidth, and E_{res} is the central frequency of the autoionization resonance. The non-resonant background has been subtracted from the absorption spectrum. The fit values of q for the $5s5p^6 6p$ and $5s5p^6 7p$ states are 0.239 ± 0.1 and -0.065 ± 0.3, respectively. The fit Fano peaks are reasonably accurate for the $5s5p^6 6p$ state, but the fit q parameter for the $5s5p^6 7p$ differs significantly from the literature values. The instrumental spectral resolution of $\sim$100 meV contributes to the errors. The fit value of q for the $5s5p^6 6p$ state must be taken with the caveat that there may be multiple peaks under the single observed peak at 20.95 eV.

The time-dependent absorption spectra (non-resonant background subtracted) are shown in Figure 5.7. The optical density ($OD(\omega, t)$) is given by:

$$OD(\omega, t) = - \, Log[I_t(\omega)/I_i(\omega)] \tag{5.9}$$

where $I_t(\omega)$ is the transmitted spectrum of the attosecond pulse recorded with He target gas and at pump-probe delay t. The plotted spectra are the average of five pump-probe scans. For each pump-probe scan, the spectrum at every pump-probe delay is recorded for 6×10^4

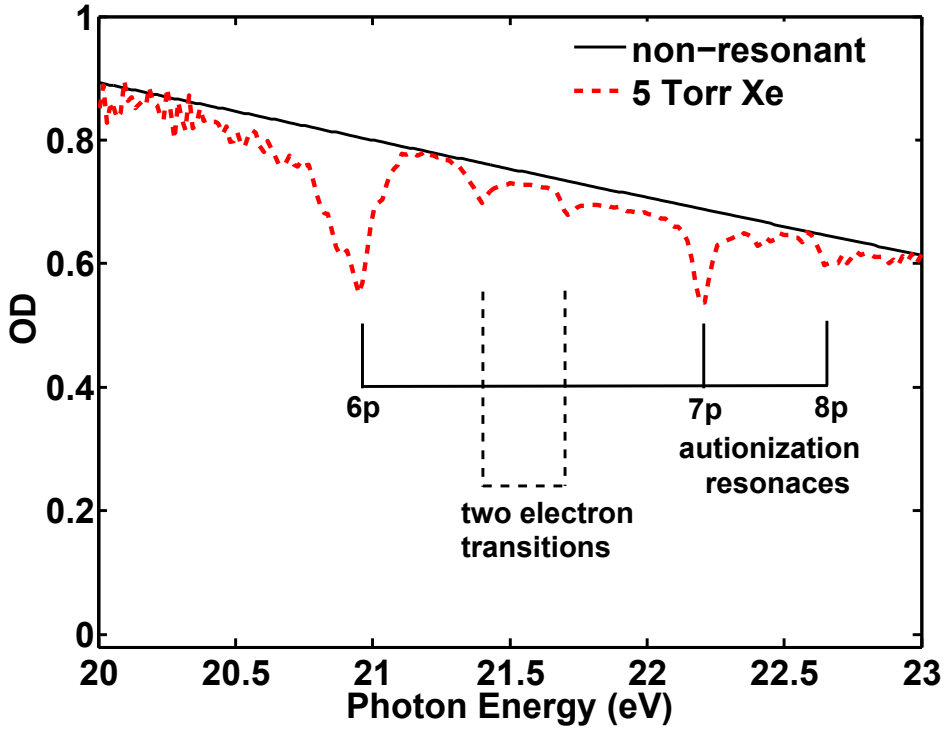

Figure 5.5: Optical density (OD) with $5s5p^6 6p$ and $5s5p^6 7p$ states and two electron transitions identified.

laser pulses. The near-infrared (NIR) pulse duration is approximately 12 fs and the NIR intensity is $(1 \pm 0.4) \times 10^{12}$ W/cm^2. The pump-probe delay is scanned in 0.33 fs steps. The pump-probe spectra were recorded with pump-probe delays extending to only -40 fs because the decreased absorption signal was anticipated to follow the lifetime of the autoionizing state. Positive pump-probe delays correspond to the NIR pulse arriving at the target gas cell before the attosecond pulse. In Figure 5.7, pump-probe delay is the x-axis, photon energy is the y-axis, and the optical density is given by the color scale. Line spectrum at +10 fs is plotted to the right of the time-dependent absorption spectrum, with the $5s5p^6 6p$ and $5s5p^6 7p$ peaks labeled. Below the two-dimensional false color plot, the absorption signal at 20.95 eV is plotted as a function of pump-probe delay.

The dark red region in the absorption spectrum near 21 eV corresponds to the $5s5p^6 6p$ state and the orange region around 22.2 eV corresponds to $5s5p^6 7p$ state. At positive times, the NIR pulse arrives before the attosecond pulse and the absorption spectra resemble the field-free absorption. As the pump-probe delay approaches 0 fs, the autoionization peaks become less pronounced. The $5s5p^6 6p$ obviously becomes less intense, while changes to the $5s5p^6 7p$ autoionization state are less clear. As the pump-probe delay becomes increasingly negative, the autoionization peak recovers. There is an asymmetry: the decline at positive times occurs more rapidly than the recovery at negative times, as seen in the line-out plotted

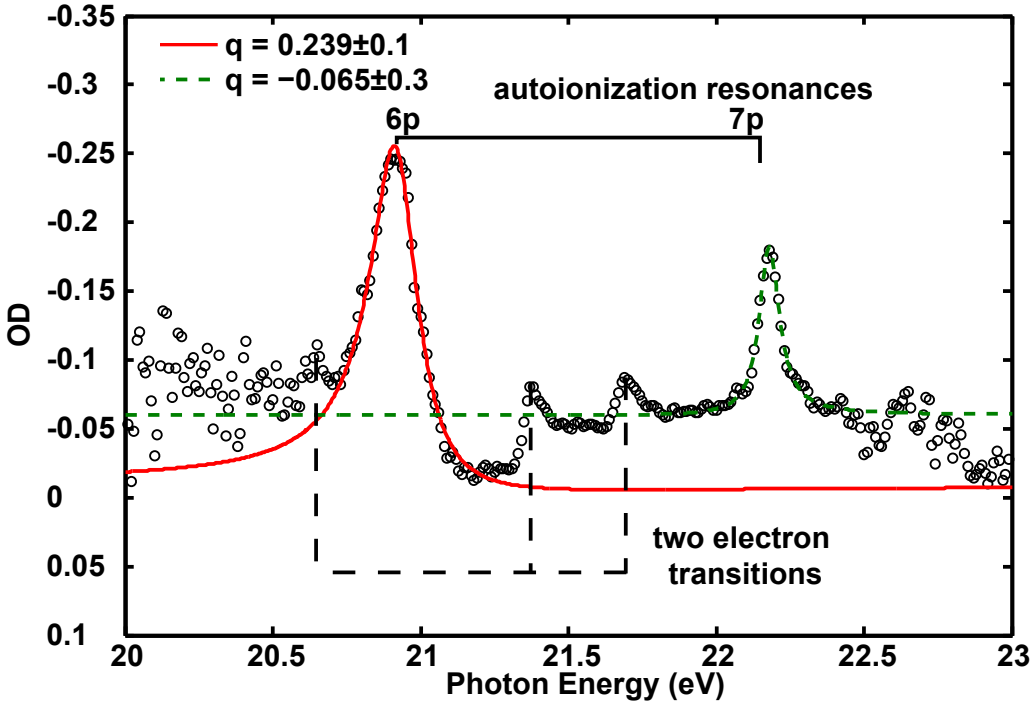

Figure 5.6: Absorption spectrum fit with Fano parameters. The non-resonant background has been subtracted.

at the bottom of Figure 5.7.

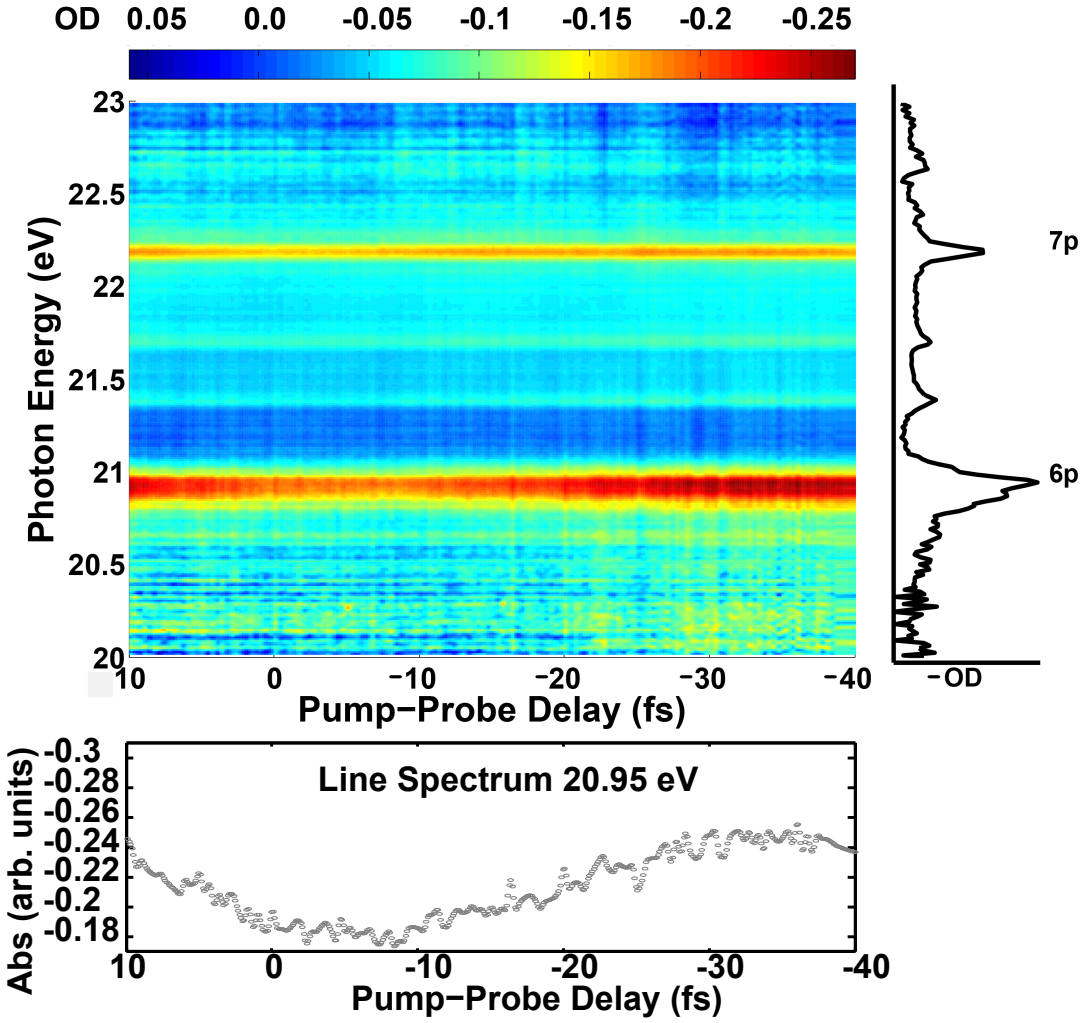

Figure 5.7: Time-dependent absorption spectra. A two-dimensional false color plot of the absorption spectra is plotted (top), a line-out of OD measured at 20.95 eV is plotted (bottom), and a line spectrum at +10 fs is plotted to the right.

5.3 Analysis and discussion

5.3.1 Attenuation of autoionization peaks

When the attosecond pulse and the NIR pulse are overlapped (near zero fs delay in Figure 5.7) the autoionization features decrease. To understand this the field perspective of absorption is employed [75–77]. The attosecond XUV field induces a polarization of the $5s5p^6 6p$ and $5s5p^6 7p$ autoionizing states. The induced polarization will radiate out with a

decay constant ($\tau_p = \frac{1}{\Gamma/2}$) that corresponds to twice the lifetime of the state [71]. This is a consequence of the population of the autoionizing state depending on the square of the state's wavefunction, while the polarization depends on the wave function. For a state with a lifetime $1/\Gamma$:

$$\text{Population(t)} \propto e^{-t\Gamma} = |e^{-t\Gamma/2}|^2 \tag{5.10}$$

$$\text{Polarization(t)} \propto e^{-t\Gamma/2} \tag{5.11}$$

Both the field from the induced polarization and the transmitted XUV field are detected. The signal that the detector (in this case an X-Ray CCD camera) records is the Fourier transform of the combined field from the induced polarization and the incident field. In the time-dependent measurements plotted in Section 5.2 the induced polarization is modified by the subsequent NIR field, resulting in a depletion of the autoionizing state. The polarization may be modified by the NIR field coupling the autoionizing states to continuum states (ionization), or to other excited states of Xe. The exact mode of action is not known. As the NIR laser arrives later and later after the XUV attosecond pulse, the polarization has already had time to decay, resulting in the autoionization peak recovering as the pump-probe delay becomes increasingly negative.

5.3.2 Fitting time-resolved spectra

Figure 5.8 plots the optical density at 20.95 eV (the $5s5p^6 7p$ resonance) as a function of pump-probe delay. The absorption is fit with a function corresponding to an instrument response function convolved with an exponential decay [144]. The functional form of the equation is:

$$\sigma(t)_{rec} = A \times Exp[-\frac{t-t_0}{\tau} + \frac{\sigma_{cc}^2}{2\tau^2}] \times (1 + Erf[\frac{1}{\sqrt{2}}(\frac{t-t_0}{\sigma_{cc}} - \frac{\sigma_{cc}}{\tau}]) + B \tag{5.12}$$

where $\sigma(t)_{rec}$ is the measured absorption, τ is recovery constant for the autoionization signal, σ_{cc} is the experimental cross-correlation of the pump and probe pulses, and A and B are constants. Based on prior measurements with argon [3], the recovery constant τ is expected to be the polarization decay constant τ_p (or twice the lifetime given by the linewidth).

The expected decay constant for the the $5s5p^6 7p$ autoionizing state is 44 fs. A fit with with τ fixed at 44 fs is plotted as the red curve in Figure 5.8, which does not fit the data well. The blue dashed-doted curve is the best fit, however the recovery constant (13.7 ± 1.6 fs) is significantly shorter than the value expected from spectroscopic measurements. All other fit parameters were allowed to freely vary. A fit constraining the value of τ to 22 fs is also plotted for reference.

The recovery of decay constants is improved by fitting the absorption spectrum at each pump-probe delay according to the parameterized absorption function in Equation 5.8 to find the value of σ_a as a function of pump-probe delay. The values of σ_a are then fit according to Equation 5.12. The values of σ_a are plotted in Figure 5.9 and plotted with several fits of

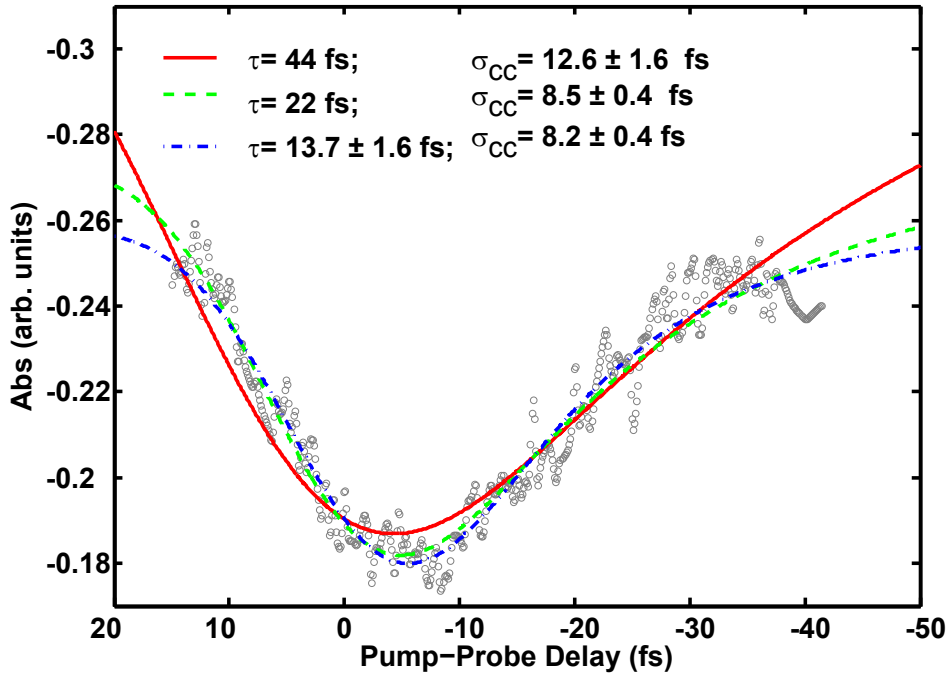

Figure 5.8: Absorption at 20.95 eV as a function of pump-probe delay fit with $\sigma(t)_{rec}$ for several τ.

$\sigma(t)_{rec}$. The best fit value of the recovery is found to be 30.2 $\pm$ 1.8 fs. This is shorter than the expected recovery of 44 fs, but the value is significantly closer than τ recovered from fitting the data directly with Equation $\sigma(t)_{rec}$.

Fitting the measured spectra to a Fano profile before recovering time-dependent data has a few advantages: Equation 5.8 contains a term for the non-resonant background, so fitting the measured spectra to a Fano profile removes background fluctuations and long term drift from the data. Fitting the data to Equation 5.8 also ensures that the signal at the exact line center of the Fano peak is being fit with $\sigma(t)_{rec}$. Equation 5.8 also contains parameters for q and Γ. Monitoring those parameters over pump-probe delay, for example, can be used to estimate increased lifetime broadening from linewidth changes, and possibly changes to transition probabilities that define q [136]. The current experimental resolution, which is greater than the literature linewidths, precludes any definite conclusions about variations in q or Γ as a function of pump-probe delay.

Qualitative model

The time-dependent spectra plotted in Section 5.2 demonstrate optical control of the attosecond XUV absorption spectra of $5s5p^6 6p$ and $5s5p^6 7p$ states of Xe. The following qualitative model illustrates the effect a time delayed NIR field has on the autoionizing states.

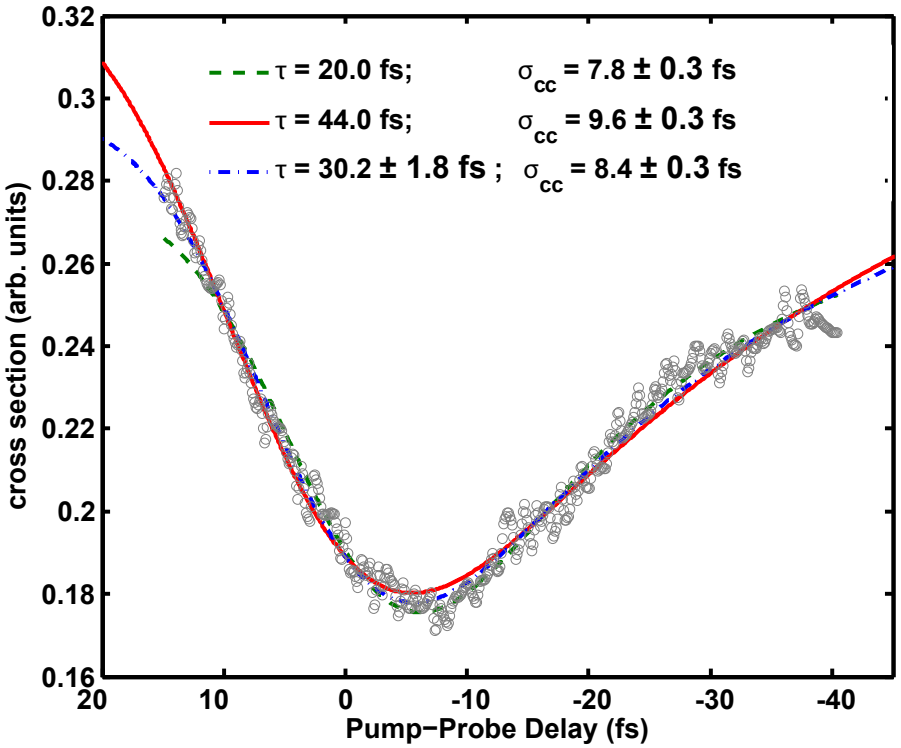

Figure 5.9: The fit values of σ_a, as a function of pump-probe delay fit with $\sigma(t)_{rec}$ for several τ. The best fit curve of $\sigma(t)_{rec}$ produces a recovery constant of approximately 30 fs.

The atomic induced polarization field for $5s5p^6 6p$ state is assumed to have the form:

$$P_a(t) = \frac{i}{\hbar}\Theta Exp[i\omega_{6p}t - (\Gamma/2)t] \tag{5.13}$$

where Θ is the Heaviside function, ω_{6p} is the excitation frequency of the $5s5p^6 6p$ state, and $\frac{\Gamma}{2} = 1/\tau_p$ is the decay rate [71]. To mimic the effect of the NIR field coupling the autoionizing state to other states (either continuum or bound states), the polarization is curtailed at a time delay (t_d). Figure 5.10 plots the unmodified polarization ($\tau_p = 44$ fs) and polarization truncated at –15 fs (i.e. the attosecond XUV pulse has arrived at the gas target 15 fs before the NIR pulse). To simulate the effect of a pump-probe delay scan the modified polarization is calculated for a series of t_d ranging from 0 to –150.

The modified polarization is then Fourier transformed and the imaginary part of the resulting $\widetilde{P}_a(\omega)$ can be used to find the absorption coefficient ($\alpha(\omega)$) [71].

$$\alpha(\omega) \propto Im\left[\frac{\widetilde{P}_a(\omega)}{\widetilde{E}_{in}(\omega)}\right] \tag{5.14}$$

where $\widetilde{E}_{in}(\omega)$ is given by the incident spectral intensity. Representative spectra are plotted in Figure 5.11 (top) for unmodified polarization (solid line) and polarization truncated at –15 fs

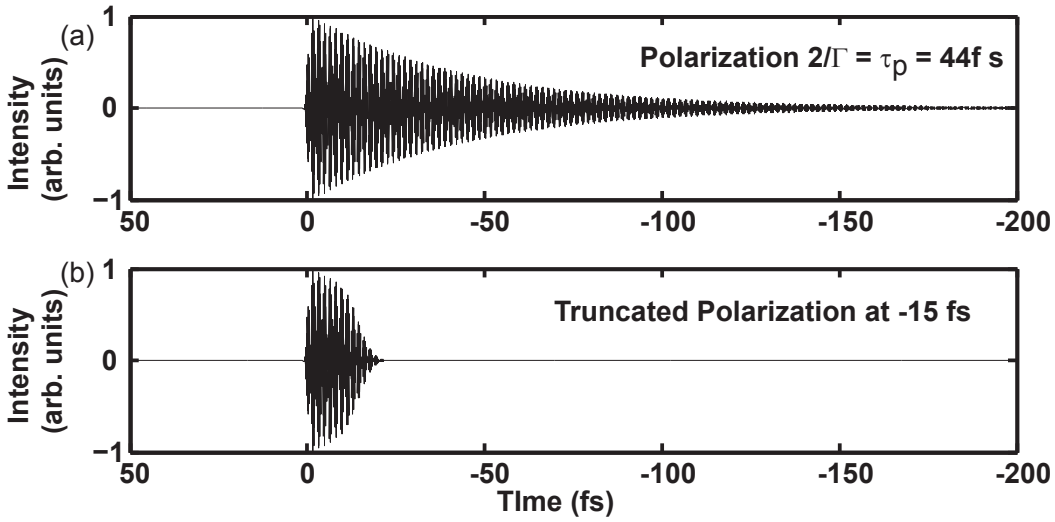

Figure 5.10: Induced polarization (top) corresponding to the $5s5p^6 6p$ autoionizing state with a decay of $\sim$ 44 fs and (bottom) the polarization truncated at –15 fs.

(dashed line). Figure 5.11 (bottom) plots the resulting spectra for polarizations truncated for t_d ranging from 0 to -150 fs. For time delays close to 0, corresponding to exact overlap of the XUV attosecond pulse and the NIR pulse, the peak is diminished, and as the time delay becomes more negative the peak recovers. The cross section on line center (20.95 eV), and the average cross section between 20.90 and 21.00 eV is plotted as a function of pump-probe delay in Figure 5.12. The absorption signal exactly on line center is nicely fit by an exponential with a time constant of 44 fs. However, the averaged signal does not have a recovery constant corresponding to the polarization decay.

Density matrix methods

The current results highlight the conditions necessary to measure field-free ultrashort lifetimes. As shown by the qualitative model, it is necessary to measure the time-dependent absorption spectra with resolution at least as narrow as the linewidth. This effect has also been demonstrated in calculations of the polarization using the Von Neumann equation (performed by Dr. Adrian Pfeiffer a post-doctoral scholar working in the Leone group). For completeness the methods and results will be summarized here. The technique is outlined in Ref. [122] and is generalized to include a phenomenological decay constant as in Lin et al. [125]. The transient absorption spectra are found from the atomic polarization response induced in the atom by the XUV attosecond pulse and the NIR pulse. The spectrum of the transmitted XUV pulse ($\widetilde{E}_{out}(\omega)$) is found by:

$$\widetilde{E}_{out}(\omega) = \widetilde{E}_{in}(\omega) Exp[i \frac{2\pi\omega N \widetilde{P}_a(\omega)}{c\widetilde{E}_{in}(\omega)} L] \tag{5.15}$$

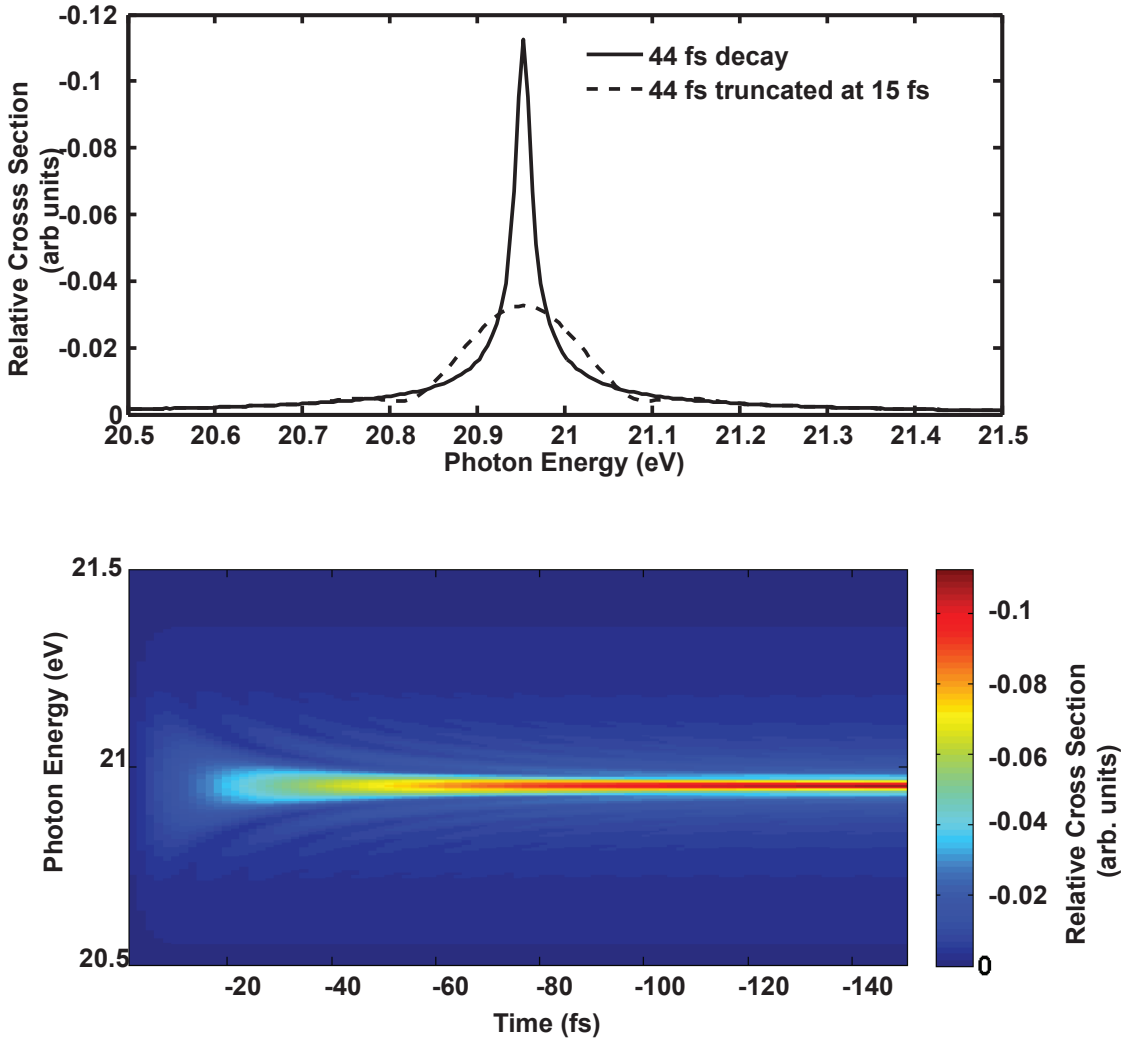

Figure 5.11: The relative cross section determined from the Fourier transformed polarization with no truncation and for t_d = –15 fs (top). The relative cross section as a function of pump-probe delay (bottom).

where $\widetilde{E}_{in}(\omega)$ is the spectrum of the incident XUV pulse, $\widetilde{P}_a(\omega)$ is the atomic polarization response in the frequency domain, N is the density of target gas, c is the speed of light in vacuum, and L is the path length of absorption. This is a formulation of the Beer-Lambert law using $\alpha(\omega)$ calculated in a manner similar to Equation 5.14.

The time-dependent polarization response is calculated as:

$$P = Tr(\rho \cdot \mathbf{d}) \tag{5.16}$$

the trace of the product of the density matrix (ρ) and transition dipole matrix ($\mathbf{d}$). The time

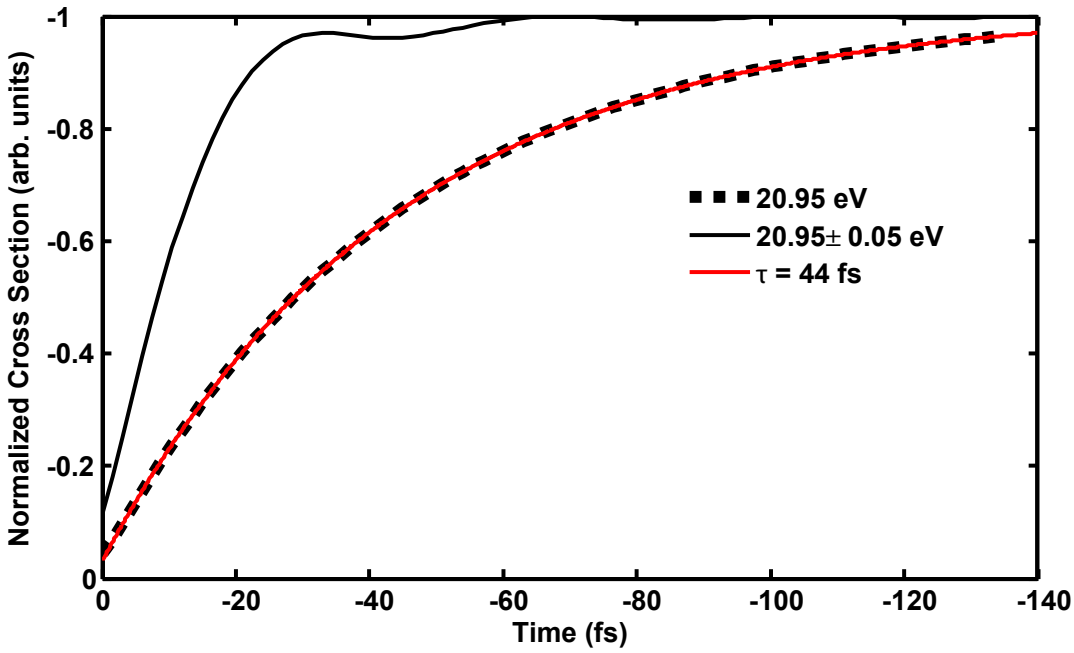

Figure 5.12: The relative cross section as a function of pump probe delay for (dashed line) line center of the absorption resonance and the cross section averaged over a range of 100 meV about the resonance (solid line). The recovery time is significantly shortened for the averaged measurement.

evolution of the density matrix is found from a modified form of the von Neumann equation:

$$i\dot{\rho} = [\mathbf{H}, \rho] + i\mathbf{\Gamma} \tag{5.17}$$

Where $\mathbf{H}$ is the Hamiltonian and $\mathbf{\Gamma}$ is a matrix that contains the decay rates of the states. The von Neumann equation is solved using a fourth-order Runge-Kutta method. The results of the simulations indicate that convolving the absorption spectra with a 50 meV full-width at half-maximum Gaussian function to simulate experimental spectral resolution greatly reduced the decay constant in Equation 5.12 (to ~ 8 fs from the expected 44 fs), while the spectra with infinite resolution are fit with the expected decay constant. This result requires that measurements of ultrashort lifetimes have resolutions better than resonance linewidths.

The density matrix calculations also incorporate coupling to other nearby states, so effects like Autler-Townes splitting and Rabi cycling may be modeled. High resolution measurements can help elucidate the role of coupling to to other excited states. For example, line shifting and broadening is observed in transient absorption spectra of autoionizing states in argon and xenon. The level shifts are explained by NIR induced couplings of the autoionizing states to other nearby states, as in Autler-Townes splitting [3, 122, 125, 135, 136].

Full quantum mechanical methods

An ongoing collaboration with the research group of Professor C. William McCurdy (University of California, Davis and Lawrence Berkeley National Lab) is focused on full quantum mechanical calculations of transient absorption spectra, with an emphasis on states with ultrashort lifetimes. Preliminary efforts are determining the experimental conditions (for example NIR laser intensity and spectral resolution) under which ultrashort lifetimes can be accurately measured.

5.4 Conclusions and outlook

The measurements in this chapter have highlighted critical parameters for lifetime retrieval. The experimental resolution must be greater than the expected linewidth in order for accurate lifetime information to be extracted. Fitting of the recovery will also be improved by recording data out to larger pump-probe delays. Experimental measurements with several NIR field intensities may elucidate what field parameters are required to determine accurate lifetimes. For example, NIR fields with sufficient magnitude to induce Rabi cycling may produce complex time-dependent spectra and spectral changes that cannot be straightforwardly fit with simple analytic functions like Equation 5.12 [135, 136]. To facilitate these measurements a new attosecond experimental apparatus has been designed and built, with greatly improved spectral resolution and increased photon flux of the attosecond pulse.

Understanding the simple atomic case is advantageous for analogous measurements on more complicated molecular targets in the future. Absorption measurements of more complex targets with overlapping Fano resonances may be described by adding additional terms to the parameterization given by Equation 5.8. Measurements on molecular targets provide the opportunity to study the coupling of electronic and nuclear dynamics because for many molecular excited states that lie above the ionization potential, there are competing decay pathways; for example autoionization and predissociation as in molecular nitrogen [145, 146] and oxygen [147, 148].

Bibliography

[1] A. H. Zewail. *J. Phys. Chem.*, **104**, 5660 (2000).

[2] M. Drescher, M. Hentschel, R. Kienberger, G. Tempea, C. Spielmann, G. A. Reider, P. B. Corkum, and F. Krausz. *Science*, **291**, 1923 (2001).

[3] H. Wang, M. Chini, S. Chen, C.-H. Zhang, F. He, Y. Cheng, Y. Wu, U. Thumm, and Z. Chang. *Phys. Rev. Lett.*, **105**, 143002 (2010).

[4] E. Goulielmakis, Z.-H. Loh, A. Wirth, R. Santra, N. Rohringer, V. S. Yakovlev, S. Zherebtsov, T. Pfeifer, A. M. Azzeer, M. F. Kling, S. R. Leone, and F. Krausz. *Nature (London, U.K.)*, **466**, 739 (2010).

[5] M. Schultze, M. Fiess, N. Karpowicz, J. Gagnon, M. Korbman, M. Hofstetter, S. Neppl, A. L. Cavalieri, Y. Komninos, T. Mercouris, C. A. Nicolaides, R. Pazourek, S. Nagele, J. Feist, J. Burgdörfer, A. M. Azzeer, R. Ernstorfer, R. Kienberger, U. Kleineberg, E. Goulielmakis, F. Krausz, and V. S. Yakovlev. *Science*, **328**, 1658 (2010).

[6] M. F. Kling and M. J. J. Vrakking. *Annu. Rev. Phys. Chem.*, **59**, 463 (2008).

[7] T. Pfeifer, M. J. Abel, P. M. Nagel, A. Jullien, Z.-H. Loh, M. J. Bell, D. M. Neumark, and S. R. Leone. *Chem. Phys. Lett.*, **463**, 11 (2008).

[8] F. Krausz and M. Ivanov. *Rev. Mod. Phys.*, **81**, 163 (2009).

[9] L. Gallmann, C. Cirelli, and U. Keller. *Annu. Rev. Phys. Chem.*, **63**, 447 (2012).

[10] Z.-H. Loh and S. R. Leone. *J. Phys. Chem. Lett.*, **4**, 292 (2013).

[11] M. Drescher, M. Hentschel, R. Kienberger, M. Uiberacker, V. Yakovlev, A. Scrinzi, T. Westerwalbesloh, U. Kleineberg, U. Heinzmann, and F. Krausz. *Nature (London, U.K.)*, **419**, 803 (2002).

[12] P. Eckle, A. N. Pfeiffer, C. Cirelli, A. Staudte, R. Dörner, H. G. Muller, M. Büttiker, and U. Keller. *Science*, **322**, 1525 (2008).

[13] S. Gilbertson, M. Chini, X. Feng, S. Khan, Y. Wu, and Z. Chang. *Phys. Rev. Lett.*, **105**, 263003 (2010).

[14] U. Becker and D. A. Shirley (editors). *VUV and Soft X-Ray Photoionization.* Plenum Press, New York (1996).

[15] L. S. Cederbaum, J. Zobrlry, and F. Tarantelli. *Phys. Rev. Lett.*, **79**, 4778 (1997).

[16] C. Buth, R. Santra, and L. S. Cederbaum. *J. Chem. Phys.*, **119**, 7763 (2003).

[17] S. Scheit, H.-D. Meyer, and L. S. Cederbaum. *J. Phys. Conf. Ser. 4*, **4**, 277 (2005).

[18] A. D. Dutoi, M. Wormit, and L. S. Cederbaum. *J. Chem. Phys.*, **134**, 024303 (2011).

[19] S. Nagele, R. Pazourek, J. Feist, K. Doblhoff-Dier, C. Lemell, K. Tokési, and J. Burgdör-

fer. *J. Phys. B: At. Mol. Opt. Phys.*, **44**, 081001 (2011).
[20] I. A. Ivanov. *Phys. Rev. A: At. Mol. Opt. Phys.*, **83**, 023421 (2011).
[21] C.-H. Zhang and U. Thumm. *Phys. Rev. A*, **82**, 043405 (2010).
[22] E. P. Wigner. *Phys. Rev.*, **98**, 145 (1995).
[23] F. T. Smith. *Phys. Rev.*, **118**, 349 (1960).
[24] K. Klünder, J. M. Dahlström, M. Gisselbrecht, T. Fordell, M. Swoboda, D. Guénot, P. Johnsson, J. Caillat, J. Mauritsson, A. Maquet, R. Taïeb, and A. L'Huillier. *Phys. Rev. Lett.*, **106**, 143002 (2011).
[25] A. Lagendijk and B. A. van Tiggelen. *Phys. Rep.*, **270**, 143 (1996).
[26] A. L. Cavalieri, N. Müller, T. Uphues, V. S. Yakovlev, A. Baltuska, B. Horvath, B. Schmidt, L. Blümel, R. Holzwarth, S. Hendel, M. Drescher, U. Kleineberg, P. M. Echenique, R. Kienberger, F. Krausz, and U. Heinzmann. *Nature (London, U.K.)*, **449**, 1029 (2007).
[27] J. C. Baggesen and L. B. Madsen. *Phys. Rev. A*, **78**, 032903 (2008).
[28] C.-H. Zhang and U. Thumm. *Phys. Rev. Lett.*, **103**, 239902 (2009).
[29] M. Uiberacker, T. Uphues, M. Schultze, A. J. Verhoef, V. Yakovlev, M. F. Kling, J. Rauschenberger, N. M. Kabachnik, H. Schröder, M. Lezius, K. L. Kompa, H.-G. Muller, M. J. J. Vrakking, S. Hendel, U. Kleineberg, U. Heinzmann, M. Drescher, and F. Krausz. *Nature (London, U.K.)*, **446**, 627 (2007).
[30] A. N. Pfeiffer, C. Cirelli, M. Smolarski, D. Dimitrovski, M. Abu-samha, L. B. Madsen, and U. Keller. *Nat. Phys.*, **8**, 76 (2011).
[31] Z.-H. Loh, M. Khalil, R. E. Correa, R. Santra, C. Buth, and S. R. Leone. *Phys. Rev. Lett.*, **98**, 143601 (2007).
[32] L. Young, D. A. Arms, E. M. Dufresne, R. W. Dunford, D. L. Ederer, C. Höhr, E. P. Kanter, B. Krässig, E. C. Landahl, E. R. Peterson, J. Rudati, R. Santra, and S. H. Southworth. *Phys. Rev. Lett.*, **97**, 083601 (2006).
[33] R. Santra, R. W. Dunford, and L. Young. *Phys. Rev. A: At. Mol. Opt. Phys.*, **74**, 043403 (2006).
[34] C. Buth and R. Santra. *Phys. Rev. A: At. Mol. Opt. Phys.*, **75**, 033412 (2007).
[35] J. Baggesen, E. Lindroth, and L. Madsen. *Phys. Rev. A: At. Mol. Opt. Phys.*, **85**, 013415 (2012).
[36] M. S. Schöffler, J. Titze, N. Petridis, T. Jahnke, K. Cole, L. P. H. Schmidt, A. Czasch, D. Akoury, O. Jagutzki, J. B. Williams, N. A. Cherepkov, S. K. Semenov, C. W. McCurdy, T. N. Rescigno, C. L. Cocke, T. Osipov, S. Lee, M. H. Prior, A. Belkacem, A. L. Landers, H. Schmidt-Böcking, T. Weber, and R. Dörner. *Science*, **320**, 920 (2008).
[37] A. Wirth. *Attosecond Transient Absorption Spectroscopy*. Ph.D. thesis, Ludwig Maximilian University of Munich (2011).
[38] A. Wirth, M. T. Hassan, I. Grguras, J. Gagnon, A. Moulet, T. T. Luu, S. Pabst, R. Santra, Z. A. Alahmed, A. M. Azzeer, V. S. Yakovlev, V. Pervak, F. Krausz, and E. Goulielmakis. *Science*, **334**, 195 (2011).
[39] Z. Chang. *Fundamentals of Attosecond Optics*. CRC PRess, Boca Raton, Fl (2011).

[40] A. E. Siegman. *Lasers*. University Science Books, Sausalito, CA (1986).
[41] P. B. Corkum. *Phys. Rev. Lett.*, **71**, 1994 (1993).
[42] M. Lewenstein, P. Balcou, M. Y. Ivanov, A. L'Huillier, and P. Corkum. *Phys. Rev. A*, **49**, 2217 (1994).
[43] L. Nugent-Glandorf, M. Scheer, D. A. Samuels, A. M. Mulhisen, E. R. Grant, X. Yang, V. M. Bierbaum, and S. R. Leone. *Phys. Rev. Lett.*, **87**, 193002 (2001).
[44] A. S. Sandhu, E. Gagnon, R. Santra, V. Sharma, W. Li, P. Ho, P. Ranitovic, C. L. Cocke, M. M. Murnane, and H. C. Kapteyn. *Science*, **322**, 1081 (2008).
[45] B. K. McFarland, J. P. Farrell, P. H. Bucksbaum, and M. Gühr. *Science*, **322**, 1232 (2008).
[46] K. R. Siefermann, Y. Liu, E. Lugovoy, O. Link, M. Faubel, U. Buck, B. Winter, and B. Abel. *Nat. Chem.*, **2**, 274 (2010).
[47] P. B. Corkum, N. H. Burnett, and M. Y. Ivanov. *Opt. Lett.*, **19**, 1870 (1994).
[48] M. Ivanov, P. B. Corkum, T. Zuo, and A. Bandrauk. *Phys. Rev. Lett.*, **74**, 2933 (1995).
[49] C. Altucci, C. Delfin, L. Roos, M. B. Gaarde, A. L'Huillier, I. Mercer, T. Starczewski, and C.-G. Wahlström. *Phys. Rev. A: At. Mol. Opt. Phys.*, **58**, 3934 (1998).
[50] O. Tcherbakoff, E. Mével, D. Descamps, J. Plumridge, and E. Constant. *Phys. Rev. A: At. Mol. Opt. Phys.*, **68**, 043804 (2003).
[51] H. Mashiko, S. Gilbertson, C. Li, S. Khan, M. Shakya, E. Moon, and Z. Chang. *Phys. Rev. Lett.*, **100**, 103906 (2008).
[52] H. Mashiko, S. Gilbertson, M. Chini, X. Feng, C. Yun, H. Wang, S. D. Khan, S. Chen, and Z. Chang. *Opt. Lett.*, **34**, 3337 (2009).
[53] Z. Chang. *Phys. Rev. A: At. Mol. Opt. Phys.*, **76**, 051403 (2007).
[54] H. Mashiko, M. J. Bell, A. R. Beck, M. J. Abel, P. M. Nagel, C. P. Steiner, J. Robinson, D. M. Neumark, and S. R. Leone. *Opt. Express*, **18**, 25887 (2010).
[55] P. Emma, K. Bane, M. Cornacchia, Z. Huang, H. Schlarb, G. Stupakov, and D. Walz. *Phys. Rev. Lett.*, **92**, 074801 (2004).
[56] A. Zholents and G. Penn. *Phys. Rev. Spec. Top. Accel Beams*, **8**, 050704 (2005).
[57] E. Saldin, E. Schneidmiller, and M. Yurkov. *Phys. Rev. Spec. Top. Accel Beams*, **9**, 050702 (2006).
[58] A. Zholents and W. Fawley. *Phys. Rev. Lett.*, **92**, 224801 (2004).
[59] J. Itatani, F. Quéré, G. L. Yudin, M. Y. Ivanov, F. Krausz, and P. B. Corkum. *Phys. Rev. Lett.*, **88**, 173903 (2002).
[60] Y. Mairesse, F. Quéré, and F. Qu. *Phys. Rev. A: At. Mol. Opt. Phys.*, **71**, 011401 (2005).
[61] E. Gagnon, A. S. Sandhu, A. Paul, K. Hagen, A. Czasch, T. Jahnke, C. L. Cocke, B. Walker, M. M. Murnane, and H. C. Kapteyn. *Rev. Sci. Instrum.*, **79**, 063102 (2008).
[62] R. Trebino and D. J. Kane. *J. Opt. Soc. Am. A*, **10**, 1101 (1994).
[63] D. J. Kane. *IEEE J. Quantum Electron.*, **35**, 421 (1999).
[64] M. Chini, S. Gilbertson, S. D. Khan, and Z. Chang. *Opt. Express*, **18**, 13006 (2010).
[65] M. Jurvansuu, A. Kivimäki, and S. Aksela. *Phys. Rev. A: At. Mol. Opt. Phys.*, **64**, 012502 (2001).

[66] R. G. W. Norrish and G. Porter. *Nature (London, U.K.)*, **164**, 658 (1949).
[67] C. Bressler and M. Chergui. *Annu. Rev. Phys. Chem.*, **61**, 263 (2010).
[68] T. Brabec and F. Krausz. *Rev. Mod. Phys.*, **72**, 545 (2000).
[69] T. Kobayashi, T. Saito, and H. Ohtani. *Nature (London, U.K.)*, **414**, 531 (2001).
[70] T. K. Ahn, T. J. Avenson, M. Ballottari, Y.-C. Cheng, K. K. Niyogi, R. Bassi, and G. R. Fleming. *Science*, **320**, 794 (2008).
[71] C. Rulliere. *Femtosecond Laser Pulses: Principles and Experiments*. Springer-Verlag, Berlin (2004).
[72] Z.-H. Loh, M. Khalil, R. E. Correa, and S. R. Leone. *Rev. Sci. Instrum.*, **79**, 073101 (2008).
[73] M. Schultze, E. M. Bothschafter, A. Sommer, S. Holzner, W. Schweinberger, M. Fiess, M. Hofstetter, R. Kienberger, V. Apalkov, V. S. Yakovlev, M. I. Stockman, and F. Krausz. *Nature (London, U.K.)*, **493**, 75 (2012).
[74] M. Chini, X. Wang, Y. Cheng, Y. Wu, D. Zhao, D. A. Telnov, S.-I. Chu, and Z. Chang. *Sci. Rep.*, **3**, 1105 (2013).
[75] W. T. Pollard and R. A. Mathies. *Annu. Rev. Phys. Chem.*, **43**, 497 (1992).
[76] R. Santra, V. S. Yakovlev, T. Pfeifer, and Z.-H. Loh. *Phys. Rev. A: At. Mol. Opt. Phys.*, **83**, 033405 (2011).
[77] S. Mukamel. *Principles of Nonlinear Optical Spectroscopy*. Oxford University Press, New York (1995).
[78] D. J. Jones, S. T. Cundiff, T. M. Fortier, J. L. Hall, and J. Ye. In F. Kartner (editor), *Few Cycle Pulse Generation and Its Applications, Topics in Applied Physics 95*, volume 343, 317–343. Springer, Bellingham, WA (2004).
[79] M. J. Abel. *Attosecond X-Ray Pulses for Molecular Electronic Dynamics*. Ph.D. thesis, University of California, Berkeley (2010).
[80] P. M. Nagel. *Plasmon enhanced photoelectron spectroscopy and the generation of isolated attosecond XUV pulses for use with condensed matter targets*. Ph.D. thesis, University of California, Berkeley (2011).
[81] P. Tournois. *Opt. Commun.*, **140**, 245 (1997).
[82] G. M. Nisoli, S. DeSilvestri, and O. Svelto. *Appl. Phys. Lett*, **68**, 2793 (1996).
[83] M. Nisoli, S. Stagira, S. DeSilvestri, O. Svelto, S. Sartania, Z. Cheng, G. Tempea, C. Spielmann, and F. Krausz. *IEEE J. Sel. Top. Quant.*, **4**, 414 (1998).
[84] M. Wegener. *Extreme Nonlinear Optics*. Springer-Verlag, Berlin (2005).
[85] R. Szipocs, K. Ferencz, C. Spielmann, and F. Krausz. *Opt. Lett.*, **16**, 201 (1994).
[86] L. Gallmann, T. Pfeifer, P. M. Nagel, M. J. Abel, D. M. Neumark, and S. R. Leone. *Appl. Phys. B*, **86**, 561 (2006).
[87] C. Iaconis and I. A. Walmsley. *IEEE J. Quantum Electron.*, **35**, 501 (1999).
[88] H. Mashiko, S. Gilbertson, C. Li, E. Moon, and Z. Chang. *Phys. Rev. A: At. Mol. Opt. Phys.*, **77**, 063423 (2008).
[89] S. Gilbertson, S. D. Khan, Y. Wu, M. Chini, and Z. Chang. *Phys. Rev. Lett.*, **105**, 093902 (2010).
[90] B. L. Henke, E. M. Gullikson, and J. C. Davis. *At. Data Nucl. Data Tables*, **54**, 181

(1993).
[91] J. Gagnon, E. Goulielmakis, and V. S. Yakovlev. *Appl. Phys. B*, **92**, 25 (2008).
[92] S. Hufner. *Photoelectron spectroscopy: Principles and applications.* Springer-Verlag, Berlin (1995).
[93] H. Wang, M. Chini, S. D. Khan, S. Chen, S. Gilbertson, X. Feng, H. Mashiko, and Z. Chang. *J. Phys. B: At. Mol. Opt. Phys.*, **42**, 134007 (2009).
[94] D. Attwood. *Soft X-rays and Extreme Ultraviolet Radiation.* Cambridge University Press, Cambridge (1999).
[95] T. Barbec, S. Mrowka, and M. Hettrick. *Appl. Opt.*, **24**, 883 (1985).
[96] E. Spiller. *Soft X-Ray Optics.* SPIE Optical Engineering Press (1994).
[97] M. Hofstetter, A. Aquila, M. Schultze, A. Guggenmos, S. Yang, E. Gullikson, M. Huth, B. Nickel, J. Gagnon, V. S. Yakovlev, E. Goulielmakis, F. Krausz, and U. Kleineberg. *New J. Phys.*, **13**, 063038 (2011).
[98] A. Aquila, F. Salmassi, and E. Gullikson. *Opt. Lett.*, **33**, 455 (2008).
[99] M. Hofstetter, M. Schultze, M. Fiess, B. Dennhardt, A. Guggenmos, J. Gagnon, V. S. Yakovlev, E. Goulielmakis, R. Kienberger, E. M. Gullikson, F. Krausz, and U. Kleineberg. *Opt. Express*, **19**, 1767 (2011).
[100] D. J. Kane. *J. Opt. Soc. Am. B*, **25**, A120 (2008).
[101] C. Palmer. *Diffraction Grating Handbook.* Richardson Grating Laboratory, Rochester, NY (2002).
[102] X. Wang, M. Chini, Y. Cheng, Y. Wu, and Z. Chang. *Appl. Opt.*, **52**, 323 (2013).
[103] W. F. Chan, G. Cooper, and C. Brion. *Phys. Rev. A: At. Mol. Opt. Phys.*, **44**, 186 (1991).
[104] W.-C. Chu and C. Lin. *Phys. Rev. A: At. Mol. Opt. Phys.*, **85**, 013409 (2012).
[105] J. Qi, G. Lazarov, X. Wang, L. Li, L. Narducci, A. Lyyra, and F. Spano. *Phys. Rev. Lett.*, **83**, 288 (1999).
[106] T. E. Glover, M. P. Hertlein, S. H. Southworth, T. K. Allison, J. van Tilborg, E. P. Kanter, B. Krässig, H. R. Varma, B. Rude, R. Santra, A. Belkacem, and L. Young. *Nat. Phys.*, **6**, 69 (2009).
[107] M. Fleischhauer, A. Imamoglu, and J. P. Marangos. *Rev. Mod. Phys.*, **77**, 633 (2005).
[108] M. B. Gaarde, C. Buth, J. L. Tate, and K. J. Schafer. *Phys. Rev. A: At. Mol. Opt. Phys.*, **83**, 013419 (2011).
[109] P. Johnsson, J. Mauritsson, T. Remetter, A. L'Huillier, and K. J. Schafer. *Phys. Rev. Lett.*, **99**, 233001 (2007).
[110] N. Shivaram, H. Timmers, X.-M. Tong, and A. Sandhu. *Phys. Rev. A: At. Mol. Opt. Phys.*, **85**, 05180R (2012).
[111] M. Holler, F. Schapper, L. Gallmann, and U. Keller. *Phys. Rev. Lett.*, **106**, 123601 (2011).
[112] S. Chen, K. J. Schafer, and M. B. Gaarde. *Opt. Lett.*, **37**, 2211 (2012).
[113] P. Ranitovic, X. M. Tong, B. Gramkow, S. De, B. DePaola, K. P. Singh, W. Cao, M. Magrakvelidze, D. Ray, I. Bocharova, H. Mashiko, A. Sandhu, E. Gagnon, M. M. Murnane, H. C. Kapteyn, I. Litvinyuk, and C. L. Cocke. *New J. Phys.*, **12**, 013008

(2010).
[114] X. M. Tong, P. Ranitovic, C. L. Cocke, and N. Toshima. *Phys. Rev. A: At. Mol. Opt. Phys.*, **81**, 021404 (2010).
[115] M. Chini, B. Zhao, H. Wang, Y. Cheng, S. Hu, and Z. Chang. *Phys. Rev. Lett.*, **109**, 073601 (2012).
[116] F. Quéré, Y. Mairesse, and J. Itatani. *J. Mod. Opt.*, **52**, 339 (2005).
[117] D. J. Tannor. *Introduction to Quantum Mechanics: A Time- Dependent Perspective*. University Science Books, Sausalito, CA (2007).
[118] C. H. Brito Cruz, J. P. Gordon, P. C. Becker, R. L. Fork, and C. V. Shank. *IEEE J. Quantum Electron.*, **24**, 261 (1988).
[119] G. W. F. Drake. In G. W. F. Drake (editor), *Springer Handbook of Atomic, Molecular, and Optical Physics*, volume 1, chapter 11, 199–219. Springer, Berlin (2006).
[120] P. P. Sorokin and E. C. Hammond. *Appl. Phys. Lett.*, **10**, 44 (1967).
[121] P. Kukura, D. W. McCamant, and R. A. Mathies. *Annu. Rev. Phys. Chem.*, **58**, 461 (2007).
[122] A. N. Pfeiffer and S. R. Leone. *Phys. Rev. A: At. Mol. Opt. Phys.*, **85**, 053422 (2012).
[123] L. Allen and J. H. Eberly. *Optical Resonance and Two-Level Atoms*. Courier Dover, New York (1987).
[124] Z.-H. Loh, C. H. Greene, and S. R. Leone. *Chem. Phys.*, **350**, 7 (2008).
[125] M.-F. Lin, A. N. Pfeiffer, D. M. Neumark, S. R. Leone, and O. Gessner. *J. Chem. Phys.*, **137**, 244305 (2012).
[126] S. Chen, M. J. Bell, A. R. Beck, H. Mashiko, M. Wu, A. N. Pfeiffer, M. B. Gaarde, D. M. Neumark, S. R. Leone, and K. J. Schafer. *Phys. Rev. A: At. Mol. Opt. Phys.*, **86**, 063408 (2012).
[127] P. Ranitovic, X. M. Tong, C. W. Hogle, X. Zhou, Y. Liu, N. Toshima, M. M. Murnane, and H. C. Kapteyn. *Phys. Rev. Lett.*, **106**, 193008 (2011).
[128] W. F. Chan, G. Cooper, X. Guo, G. R. Burton, and C. E. Brion. *Phys. Rev. A: At. Mol. Opt. Phys.*, **46**, 149 (1992).
[129] C. Cohen-Tannoudji, J. Dupont-Roc, and G. Grynberg. *Atom-Photon Interactions*. WILEY-VCH Verlag GmbH & Co. KGaA, Weinheim (2004).
[130] P. F. Liao and J. E. Bjorkholm. *Opt. Commun.*, **16**, 392 (1976).
[131] U. Fano. *Phys. Rev.*, **124**, 1866 (1961).
[132] U. Fano and J. W. Cooper. *Phys. Rev.*, **137**, A1364 (1965).
[133] K. Codling and R. P. Maden. *Phys. Rev. A: At. Mol. Opt. Phys.*, **4**, 2261 (1971).
[134] D. L. Ederer. *Phys. Rev. A*, **4**, 2263 (1971).
[135] W.-C. Chu and C. D. Lin. *Phys. Rev. A: At. Mol. Opt. Phys.*, **87**, 013415 (2013).
[136] W.-C. Chu and C. D. Lin. *J. Phys. B: At. Mol. Opt. Phys.*, **45**, 201002 (2012).
[137] D. Cubric, D. B. Thompson, D. R. Cooper, G. King, and F. H. Read. *J. Phys. B: At. Mol. Phys.*, **30**, L857 (1997).
[138] V. L. Sukhorukov, I. D. Petrov, B. M. Lagutin, H. Schmoranzer, W. Kielich, P. V. Demekhin, and A. Ehresmann. *Eur. Phys. J. D*, **59**, 151 (2010).
[139] D. L. Ederer, A. C. Parr, J. B. West, D. Holland, and D. Dehmer. *Phys. Rev. A: At.*

Mol. Opt. Phys., **25**, 2006 (1982).
[140] M. G. Flemming, J.-Z. Wu, C. D. Caldwell, and M. O. Krause. *Phys. Rev. A: At. Mol. Opt. Phys.*, **44**, 1733 (1991).
[141] G. Herzberg. *Atomic Spectra and Atomic Structure*. Dover, New York (1945).
[142] J. West and J. Morton. *At. Data Nucl. Data Tables*, **22**, 103 (1978).
[143] A. Delage, D. Roy, and J. D. Carette. *J. Phys. B: At. Mol. Opt. Phys.*, **10**, 1487 (1977).
[144] S. Pedersen and A. H. Zewail. *Mol. Phys*, **89**, 1455 (1996).
[145] D. Strasser, L. H. Haber, B. L. Doughty, and S. R. Leone. *Mol. Phys.*, **106**, 275 (2008).
[146] P. Erman, A. Karawajczyk, U. Koble, E. Rachlew, and K. Yoshiki Franzén. *Phys. Rev. Lett.*, **76**, 4136 (1996).
[147] M. Ukai, S. Machida, K. Kameta, M. Kitajima, N. Kouchi, Y. Hatano, and K. Ito. *Phys. Rev. Lett.*, **74**, 239 (1995).
[148] H. Liebel, S. Lauer, F. Vollweiler, A. Muller-Albrecht, R. Ehresmann, H. Schmoranzer, G. Mentzel, K. H. Schartner, and O. P. Wilhelmi. *Phys. Lett. A*, **276**, 357 (2000).